

# Analysis Note

## Measurement of charged particle production in diffractive proton-proton collisions at $\sqrt{s} = 200$ GeV with tagging of the forward scattered proton

Leszek Adamczyk<sup>1</sup>, Łukasz Fulek<sup>1</sup>, Mariusz Przybycień<sup>1</sup>, and Rafał Sikora<sup>1</sup>

<sup>1</sup>*AGH University of Science and Technology, FPACS, Kraków, Poland*

2nd April 2020

In this note we present the analysis of the Single Diffractive Dissociation process with the STAR Roman Pot (RP) detectors at RHIC. The measurement is focused on the charged particle multiplicity, its dependence on the transverse momentum and pseudorapidity in three regions of  $\xi$ :  $0.02 < \xi < 0.05$ ,  $0.05 < \xi < 0.1$  and  $0.1 < \xi < 0.2$ . The identified particle to antiparticle (pion, kaon, proton and their antiparticle) multiplicity ratios as a function of transverse momentum in above three  $\xi$  regions are also measured. The data come from proton-proton collisions collected in 2015. The forward proton was tagged in the STAR Roman Pot system while the charged particle tracks were reconstructed in the STAR Time Projection Chamber (TPC). We describe all stages of the analysis involving comparison of the data with MC simulations and systematic uncertainty studies. More technical parts of the analysis are described in a supplementary analysis note [1].

## 3 List of contributions

4	<hr/>	
	Leszek Adamczyk	Analysis coordination/supervision, production of picoDST, production of embedded MC samples
5	Lukasz Fulek*	Main analyzer, write-up author
	Mariusz Przybycień	Analysis supervision
6	Rafał Sikora	Analysis support
	<hr/>	

7 \* - contact editor

8

## 9 Change log

10	<hr/>		
11	2nd April	ver. 1.0	Initial revision
12	2020		
13	<hr/>		

# Contents

15	<b>List of contributions</b>	<b>2</b>
16	<b>Change log</b>	<b>2</b>
17	<b>1 Introduction</b>	<b>1</b>
18	<b>2 Monte Carlo Samples</b>	<b>2</b>
19	<b>3 Data Sample and Event Selection</b>	<b>4</b>
20	3.1 Event Selection . . . . .	4
21	3.2 Track Selection . . . . .	5
22	3.3 Fiducial Region of the Measurement . . . . .	8
23	<b>4 Background Contribution</b>	<b>10</b>
24	4.1 Accidental Background . . . . .	10
25	4.2 Background from Non-Primary Tracks . . . . .	12
26	<b>5 Non-SD Contributions</b>	<b>20</b>
27	<b>6 Selection Efficiencies</b>	<b>24</b>
28	6.1 Vertex Reconstruction . . . . .	24
29	6.2 Correction to BBC-Small . . . . .	28
30	<b>7 Migrations into and out of the Fiducial Region</b>	<b>33</b>
31	7.1 Migrations of Tracks into and out of the Fiducial Region . . . . .	33
32	7.2 Migrations in $\xi$ . . . . .	34
33	<b>8 Corrections and Unfolding Procedure</b>	<b>37</b>
34	8.1 Correction to $dN/dn_{\text{sel}}$ . . . . .	37
35	8.2 Correction to Transverse Momentum and Pseudorapidity Distributions . . . . .	39
36	8.3 Closure Tests . . . . .	41
37	8.4 EAST-WEST asymmetry . . . . .	41
38	8.5 Particle Identification . . . . .	41
39	8.6 Antiparticle-to-Particle Ratios . . . . .	46
40	<b>9 Systematic Uncertainties</b>	<b>49</b>
41	<b>10 Results</b>	<b>54</b>
42	<b>11 Summary and Conclusions</b>	<b>61</b>
43	<b>Appendices</b>	<b>64</b>
44	<b>A Proton and Antiproton DCA Distributions</b>	<b>65</b>



# 46 Acronyms

47	<b>CD</b>	Central Diffraction
48	<b>DD</b>	Double Diffraction
49	<b>MBR</b>	Minimum Bias Rockefeller
50	<b>MC</b>	Monte Carlo
51	<b>ND</b>	Non-Diffractive
52	<b>QCD</b>	Quantum Chromodynamics
53	<b>RP</b>	Roman Pot
54	<b>SaS</b>	Schuler and Sjöstrand
55	<b>SD</b>	Single Diffraction
56	<b>TPC</b>	Time Projection Chamber

# 1. Introduction

Inclusive measurements of charged-particle distributions in proton–proton ( $pp$ ) collisions probe the strong interaction in the low-momentum transfer, non-perturbative regime of Quantum Chromodynamics (QCD). In this kinematic region interactions are usually described by phenomenological models implemented in Monte Carlo (MC) event generators. Measurements can be used to constrain the free parameters of these models. An accurate description of low-energy strong interaction processes is essential for understanding and precise simulation of different types of  $pp$  processes and the effects of multiple  $pp$  collisions in the same bunch crossing at high instantaneous luminosity at hadron colliders. Measurements with tagging of the forward-scattered proton are of special interest. They give direct access to specific but still significant part of  $pp$  processes called diffraction. In addition precise modelling of forward particle production is essential for better understanding of the longitudinal development of air showers observed in experiments studying cosmic radiation.

We present a measurement of charged particle production in events with single forward proton tagging (dominated by Single Diffraction (SD):  $p + p \rightarrow p + X$ ). The following observables are studied:

$$\frac{1}{N_{\text{ev}}} \frac{dN_{\text{ev}}}{dn_{\text{ch}}}, \quad \frac{1}{N_{\text{ev}}} \frac{1}{2\pi p_{\text{T}}} \frac{d^2 N}{d\bar{\eta} dp_{\text{T}}}, \quad \frac{1}{N_{\text{ev}}} \frac{dN}{d\bar{\eta}} \quad (1.1)$$

where  $n_{\text{ch}}$  is the number of primary charged particles within kinematic range given by  $p_{\text{T}} > 200$  MeV and  $|\eta| < 0.7$ ,  $N_{\text{ev}}$  is the total number of events with  $2 \leq n_{\text{ch}} \leq 8$ ,  $N$  is the total number of charged particles within the above kinematic acceptance and  $\bar{\eta}$  is the pseudorapidity of the charged particle with longitudinal momentum taken with respect to direction of the forward scattered proton. To suppress non-SD events the trigger system required no signal in BBC-small in the direction of forward scattered proton and signal in BBC-small in opposite direction. The measurements are performed in a fiducial phase space of the forward scattered protons of  $0.04 < -t < 0.16$  GeV<sup>2</sup>/c<sup>2</sup> and  $0.02 < \xi < 0.2$ , where  $\xi$  is the fractional energy loss of the scattered proton and  $t$  is the squared four momentum transfer. In case of SD process  $\xi = M_{\text{X}}^2/s$ , where  $M_{\text{X}}$  is the mass of the state X into which one of the incoming proton dissociates and  $s$  is the center of mass energy squared of the  $pp$  system. The Mandelstam variable  $t$  is defined by  $t = (p_1 - p_3)^2$ , where  $p_1$  is the four-momentum of the incoming proton,  $p_3$  is the four-momentum of the outgoing proton. The above mentioned observables are presented in three  $\xi$  regions:  $0.02 < \xi < 0.05$ ,  $0.05 < \xi < 0.1$  and  $0.1 < \xi < 0.2$ . In addition their average values are presented as a function of  $\xi$ .

We have also studied an identified particle to antiparticle (pion, kaon, proton and their antiparticle) multiplicity ratios as a function of  $p_{\text{T}}$  also in the above mentioned three regions of  $\xi$ . The system X into which proton diffractively dissociates has net charge and baryon number +1. It is believed that initial charge and barion number should appear in the very forward direction leading to the equal amount of particles and antiparticles in the central region created by fragmentation and hadronization processes. However other scenarios are also possible where extra baryon is uniformly distributed over rapidity [2] or even appear close to the gap edge [3]. It is natural to expect that possible charge and baryon number transfer to central region will be better visible at small  $\xi$  where amount of particle-antiparticle creation is smaller due to the generally smaller particle multiplicity or due to the fact that gap edge is inside our fiducial region of  $|\eta| < 0.7$ .

## 2. Monte Carlo Samples

MC samples used to correct data for detector effects were obtained by the embedding MC technique [4], in which simulated particles are mixed with the real Zerobias events at the raw data level. Zerobias data events used in the embedding were sampled over the entire data-taking period in order to properly describe the data set used in the analysis. Two samples of embedding MC were produced:

1. Single particle MC, in which particles are generated from flat distributions in  $\eta$  and  $p_T$ , in order to have similar statistics in all bins.
2. The Schuler and Sjöstrand (SaS) model implemented in PYTHIA 8 with 4C tune.

The particles were propagated through the full simulation of the STAR TPC and RP system detectors using GEANT3 [5] and GEANT4 [6], respectively. Obtained information for the simulated particles was embedded into the existing information of the real data. These events were next processed through the full reconstruction chain.

An iterative unfolding procedure was used to express the track multiplicity in terms of the number of charged particles. The unfolding matrices were obtained from PYTHIA 8 4C (SaS). In order to keep statistical precision coming from the matrices high, samples filtered on true-level values of  $\xi$  and  $t$  (not necessarily with reconstructed proton track in RP) are used.

It is preferred to get the detector corrections from a MC, which is dedicated to simulate the studied physics process. However, for this purpose, the statistics in the MC should be several times greater than we have in the data for analysis. Since this is not possible with low efficiency of TPC and TOF, the basic method of corrections used in the analysis for  $p_T$  and  $\bar{\eta}$  distributions is a method of factorization of global efficiency into the product of single-particle efficiencies. In this way, statistically precise multidimensional corrections on TPC and TOF were obtained from the single particle MC. The charged-particle multiplicity distributions were unfolded from the measured multiplicities of TPC tracks based on the response matrix, which takes into account all detector effects and was obtained from PYTHIA 8 4C (SaS) simulation of SD process. In this procedure single particle MC samples were not used.

Several additional MC samples were generated, in which simulated particles were propagated through full simulation and reconstruction chain but were not embedded into Zerobias events. Systematic effect related to hadronization of the diffractive system was determined by using an alternative hadronization model implemented in HERWIG. Results are compared to model predictions from PYTHIA 8 4C (SaS), HERWIG, EPOS and alternative PYTHIA 8 model Minimum Bias Rockefeller (MBR) with A2 tune. EPOS predicts very large contribution of forward protons, which originate from non-diffractive events and are well separated in rapidity from other final state particles. This is the result of low mass excitation of the proton remnant ( $< 1$  GeV) leading to hadronization of the beam remnant back to the proton. Therefore EPOS predictions were separated in two classes: diffractive (EPOS SD) modelled by Pomeron exchange and non-diffractive modelled by low mass excitation of the proton remnant (EPOS SD'). Such remnant treatment is very unique in EPOS compared to other string models, especially, to that used in PYTHIA 8, where Non-Diffractive (ND) forward protons are rare and arise from string fragmentation and hadronization. In all PYTHIA 8 models, diffractive cross-sections are scaled by the fudge factors, which were introduced in order to describe the full phase space [7, 8]. In the SaS model, the fudge factors for SD and DD,  $F_{SD}$  and  $F_{DD}$ , are defined as a function of diffractive masses:

$$F_{SD} = \left(1 - \frac{M^2}{s}\right) \left(1 + \frac{c_{res} M_{res}^2}{M_{res}^2 + M^2}\right) \quad (2.1)$$

$$F_{DD} = \left(1 - \frac{M_a^2 + M_b^2}{s}\right) \left(\frac{sm_p^2}{sm_p^2 + M_a^2 M_b^2}\right) \times \left(1 + \frac{c_{res} M_{res}^2}{M_{res}^2 + M_a^2}\right) \left(1 + \frac{c_{res} M_{res}^2}{M_{res}^2 + M_b^2}\right) \quad (2.2)$$

where  $M$  and  $M_a$ ,  $M_b$  are the invariant masses of the systems  $X$  and  $X_a$ ,  $X_b$  for SD and DD, respectively,  $c_{\text{res}} = 2$  and  $M_{\text{res}} = 2 \text{ GeV}/c^2$  were obtained from a fit to  $pp/\bar{p}p$  data [7]. On the other hand, in the MBR model the fudge factor is given as a function of the rapidity gap [8]:

$$S = \frac{1}{2} \left[ 1 + \text{erf} \left( \frac{\Delta y - \Delta y_S}{\sigma_S} \right) \right] \quad (2.3)$$

where  $\Delta y$  is the rapidity gap,  $\Delta y_S = 2$  and  $\sigma_S = 0.5$ . As a result, diffractive cross sections are artificially suppressed at relatively large values of  $\xi$  ( $>0.05$ ). This artificial suppression significantly changes predicted distribution of  $\xi$  and fractions of different processes in our fiducial phase space. Therefore data is also compared with expectations obtained without suppression of the diffractive cross sections (MBR-tuned).

Figure 2.1 shows  $\xi$  and  $|t|$  distributions generated with EPOS (SD and SD+SD') and PYTHIA 8 SD (MBR and MBR-tuned). There are differences among models in both the low and high  $\xi$  regions. The minimum value of  $|t|$  depends on the mass of the diffractive system, hence, all models predict suppression of the cross-section at small  $|t|$ . EPOS SD is only relevant for very small  $|t|$  and is suppressed in the STAR acceptance region,  $0.04 < |t| < 0.16$ , where EPOS SD' contribution dominates. In addition, the  $t$ -slope is very different for EPOS SD and SD', while it is similar for EPOS SD' and PYTHIA 8 predictions. The PYTHIA 8 (MBR-tuned) expectations, as opposed to the MBR model, lead to the larger cross-sections in the high-mass regions.

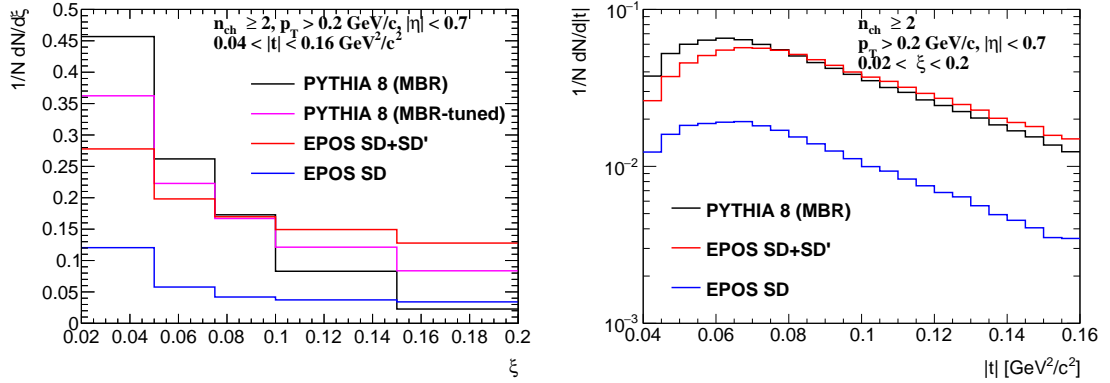


Figure 2.1: (left)  $\xi$  and (right)  $|t|$  distributions for various MC generators at  $\sqrt{s} = 200 \text{ GeV}$ .



# 3. Data Sample and Event Selection

The data sample used in this analysis was collected in proton-proton collisions at centre-of-mass energy of  $\sqrt{s} = 200$  GeV during RHIC Run 15, i.e. in year 2015.

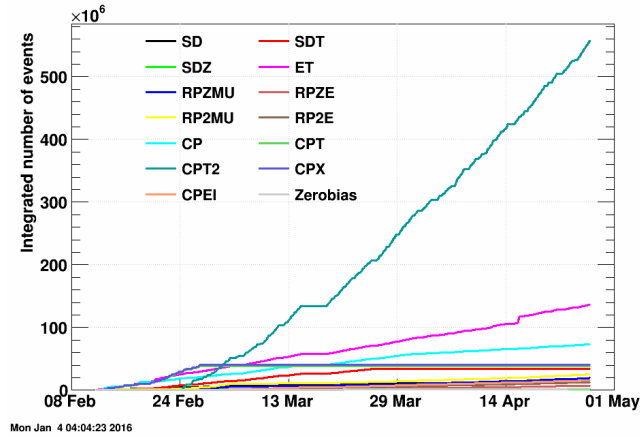


Figure 3.1: Cumulative number of events collected for each trigger in the RP data stream during Run 15 [9, 10].

All of the studies in this work use data from only the SDT trigger condition, which was the main trigger designed for SD studies in Run 15 and used in this analysis. It was formed by the following conditions combined with the logical AND:

1. RP\_EOR || RP\_WOR - signal in at least one RP on one side of the STAR central detector.
2. Veto on any signal in small BBC tiles or ZDC on the triggered RP side of the STAR central detector.
3. At least two TOF hits.

Above requirements were imposed in accordance with the diffractive events topology. Veto on any signal in small BBC tiles and ZDC allows to accept only events with rapidity gap and reject diffractive events with parallel pile-up event. The requirement of at least two TOF hits was to ensure activity in the mid-rapidity.

Integrated luminosity delivered by the RHIC to the STAR detector in  $pp$  collisions during Run 15 amounts to  $185.1 \text{ pb}^{-1}$  [11], whereas about 34.4M SDT events were gathered by the STAR detector, shown in Fig. 3.1, which corresponds to  $16 \text{ nb}^{-1}$  of integrated luminosity.

## 3.1 Event Selection

Events were selected from those passing the SDT trigger condition. In order to remove events having poor quality and to suppress background the following conditions were required:

1. Trigger signals in exactly two stations of one arm of RP system (this requirement divides the sample into four sub-samples, which were later analyzed independently, e.g. for background studies),

- 181 2. Any trigger signal in small BBC tiles on the opposite side of the STAR central detector to  
182 the triggered RP station,
- 183 3. Exactly one proton track in the above RP stations with  $0.02 < \xi < 0.2$  and  $0.04 < -t <$   
184  $0.16 \text{ GeV}^2/c^2$ .
- 185 4. Exactly one vertex with TPC tracks matched with hits in TOF (later in the text such vertex  
186 is referred as a TOF vertex),
- 187 5. Vertex within  $|V_z| < 80 \text{ cm}$  - events with vertices away from the nominal IP have low  
188 acceptance for the central and forward tracks [1],
- 189 6. At least two but no more than eight primary TPC tracks,  $2 \leq n_{\text{sel}} \leq 8$ , matched with hits  
190 in TOF and satisfying the selection criteria described in Sec. 3.2,
- 191 7. If there are exactly two primary tracks satisfying above criteria and exactly two global tracks  
192 used in vertex reconstruction (Sec. 6.1), the longitudinal distance between these global tracks  
193 should be smaller than 2 cm,  $|\Delta z_0| < 2 \text{ cm}$ , due to small ( $< 20\%$ ) vertex reconstruction  
194 efficiency for tracks with  $|\Delta z_0| > 2 \text{ cm}$  (as described in Sec. 6.1).

195 Figure 3.2 shows the multiplicity of TOF vertices  $n_{\text{vrt}}$  (left) and the  $z$ -position of reconstructed  
196 vertices in single TOF vertex events (right). Data are compared to embedded PYTHIA 8 SD  
197 sample. These distributions are not significantly process-dependent, therefore, contributions from  
198 other processes are not included in these plots. Most events with  $n_{\text{vrt}} > 1$  originate from in-time  
199 pile-up.

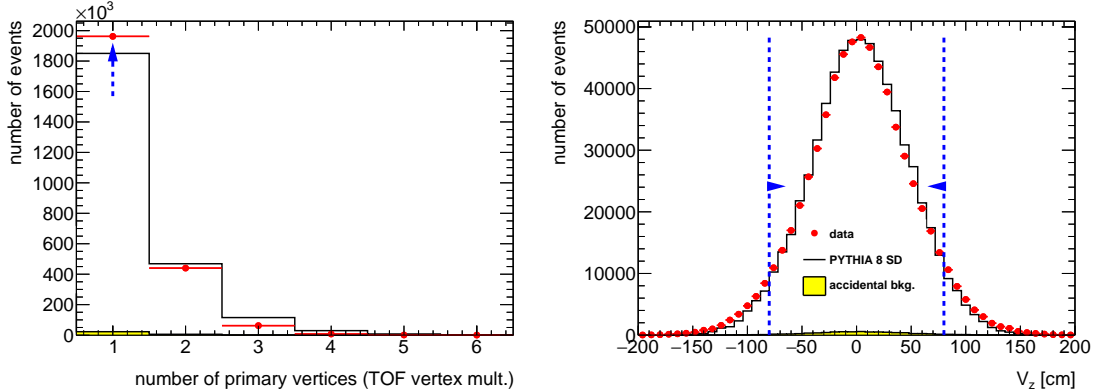


Figure 3.2: (left) TOF vertex multiplicity and (right) the  $z$ -position of reconstructed vertices in single TOF vertex events before applying the cut on the quantity shown. Blue lines indicate regions accepted in the analysis.

## 200 3.2 Track Selection

201 The following quality cuts had to be passed by the selected primary tracks in this analysis (TPC  
202 and TOF efficiencies are described in [1]):

- 203 1. The tracks must be matched with hits reconstructed in TOF,
- 204 2. The number of the TPC hits used in the helix fit  $N_{\text{hits}}^{\text{fit}}$  must be greater than 24,
- 205 3. The ratio of  $N_{\text{hits}}^{\text{fit}}$  to the number of all possible TPC hits,  $N_{\text{hits}}^{\text{fit}}/N_{\text{hits}}^{\text{possible}}$ , must be greater  
206 than 0.52,

- 207 4. The number of the TPC hits used to determine the  $dE/dx$  information  $N_{\text{hits}}^{dE/dx}$  must be  
 208 greater than 14,  
 209 5. The transverse impact parameter with respect to the beamline  $d_0$  must be less than 1.5 cm,  
 210 6. The radial component of the distance of the closest approach between the global helix and  
 211 the vertex  $\text{DCA}_{xy}$  must be less than 1.5 cm (consistent with the  $d_0$  limit),  
 212 7. The absolute magnitude of longitudinal component of the distance of the closest approach  
 213 between the global helix and the vertex  $|\text{DCA}_z|$  must be less than 1 cm,  
 214 8. The track's transverse momentum  $p_T$  must be greater than 0.2 GeV/c,  
 215 9. The track's absolute value of pseudorapidity  $|\eta|$  must be smaller than 0.7.

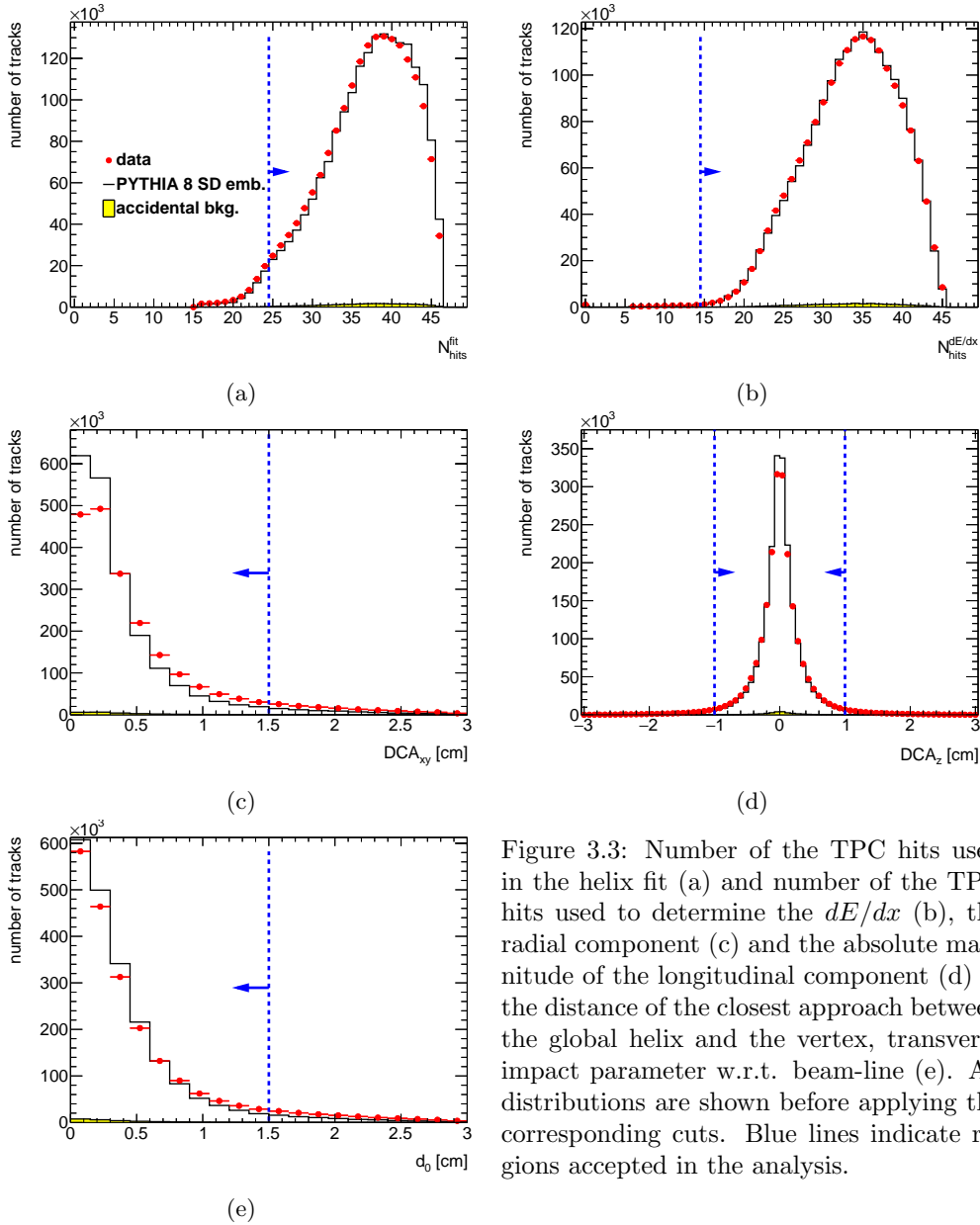


Figure 3.3: Number of the TPC hits used in the helix fit (a) and number of the TPC hits used to determine the  $dE/dx$  (b), the radial component (c) and the absolute magnitude of the longitudinal component (d) of the distance of the closest approach between the global helix and the vertex, transverse impact parameter w.r.t. beam-line (e). All distributions are shown before applying the corresponding cuts. Blue lines indicate regions accepted in the analysis.

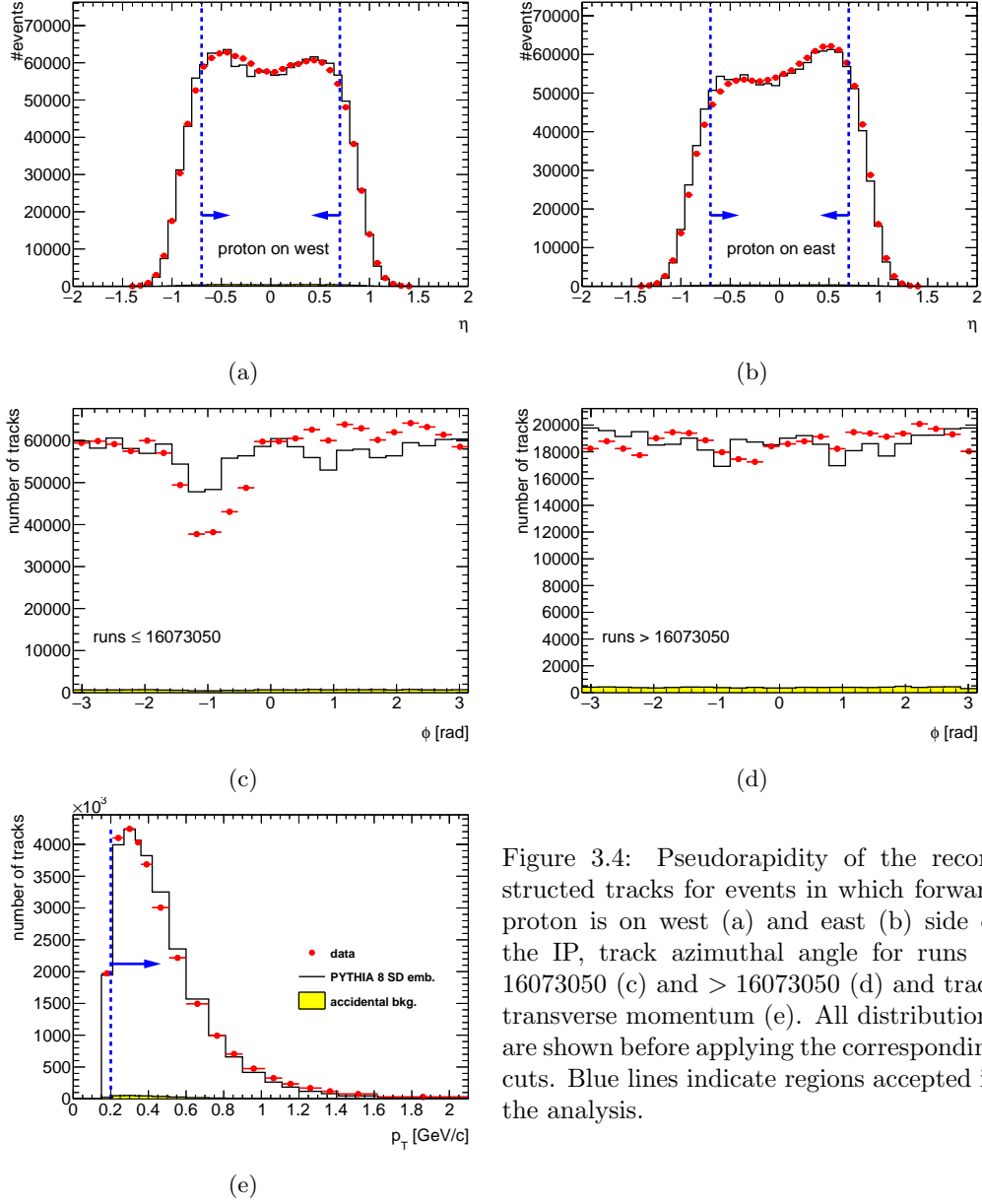


Figure 3.4: Pseudorapidity of the reconstructed tracks for events in which forward proton is on west (a) and east (b) side of the IP, track azimuthal angle for runs  $\leq 16073050$  (c) and  $> 16073050$  (d) and track transverse momentum (e). All distributions are shown before applying the corresponding cuts. Blue lines indicate regions accepted in the analysis.

216 The  $N_{\text{hits}}^{\text{fit}}$  and  $N_{\text{hits}}^{\text{fit}}/N_{\text{hits}}^{\text{possible}}$  cuts are used to reject low quality TPC tracks and avoid track  
 217 splitting effects. The  $d_0$  and global  $\text{DCA}_{xy}$ ,  $|\text{DCA}_z|$  cuts are used to select tracks that originate  
 218 from the primary interaction vertex. The cut on  $N_{\text{hits}}^{\text{dE/dx}}$  is used to ensure that selected tracks  
 219 have sufficient energy loss information for particle identification purposes. In this analysis tracks  
 220 without identification are required to have  $p_T > 0.2$  GeV/c and  $|\eta| < 0.7$  due to high track  
 221 reconstruction and TOF matching efficiencies in this region. For the identified particle-antiparticle  
 222 ratio analysis, where charged pions, charged kaons and (anti)protons are measured, the  $p_T$  cut  
 223 was increased for kaons and (anti)protons to 0.3 and 0.4 GeV/c, respectively. The distributions  
 224 of the  $\text{DCA}_{xy}$ ,  $|\text{DCA}_z|$ ,  $d_0$ ,  $N_{\text{hits}}^{\text{fit}}$  and  $N_{\text{hits}}^{\text{dE/dx}}$  quantities together with applied cuts are shown in  
 225 Fig. 3.3, while the  $p_T$ ,  $\eta$  and the azimuthal angle,  $\phi$ , of the reconstructed tracks are shown in  
 226 Fig. 3.4. Data are compared to embedded PYTHIA 8 SD sample.

227 The azimuthal angle of the reconstructed tracks for runs  $\leq 16073050$  is not described by  
 228 PYTHIA 8. The inner sector #19 in the TPC was dead for this running period and some effects

related to it were presumably not taken into account in the TPC detector simulation. Therefore, additional data-driven corrections to track efficiencies are used [1].

### 3.3 Fiducial Region of the Measurement

A fiducial phase space of measurement is defined by the following criteria. Primary charged particles are defined as charged particles with a mean lifetime  $\tau > 300$  ps, either directly produced in  $pp$  interaction or from subsequent decays of directly produced particles with  $\tau < 30$  ps. In this analysis, primary charged particles had to be contained within the kinematic range of  $p_T > 0.2$  GeV/c and  $|\eta| < 0.7$ . The results are corrected to the region of the total number of primary charged particles (without identification),  $2 \leq n_{\text{ch}} \leq 8$ . In identified charged antiparticle to particle ratio measurement, the lower transverse momentum limit was set for the analyzed particles as follows: 0.2 GeV/c (pions), 0.3 GeV/c (kaons), 0.4 GeV/c (protons and antiprotons).

The measurements were performed in a fiducial phase space of the forward scattered protons of  $0.04 < -t < 0.16$  GeV<sup>2</sup>/c<sup>2</sup> and  $0.02 < \xi < 0.2$ . Figure 3.5 shows that the fraction of events containing at least two primary charged particles,  $\epsilon_{n_{\text{ch}} \geq 2}(\log_{10} \xi)$ , is reduced by half for  $\xi < 0.02$  compared to the region of larger  $\xi$ . In addition, the accidental background contribution in this region of  $\xi$  is significant and approximately equal to 20% (Sec. 4.1). For these reasons the lower  $\xi$  cut was introduced. On the other hand, the upper  $\xi$  cut was required since the region of larger  $\xi$  is dominated by Double Diffraction (DD) and ND (Sec. 5). The joint RP acceptance and track reconstruction efficiency was defined as the probability that true-level proton was reconstructed as a track passing the selection criteria. This efficiency was calculated as a function of  $-t$  for three ranges of  $\xi$  separately and is shown in Fig. 3.6. Events were accepted in the analysis only if the reconstructed values of  $-t$  for protons fall within non-zero acceptance regions, which were required to be the same for each  $\xi$  region and similar to those defined in the elastic analysis [12]. Therefore, additional cuts on  $0.04 < -t < 0.16$  GeV<sup>2</sup>/c<sup>2</sup> were introduced.

All measured observables are presented in three  $\xi$  regions:  $0.02 < \xi < 0.05$ ,  $0.05 < \xi < 0.1$  and  $0.1 < \xi < 0.2$ .

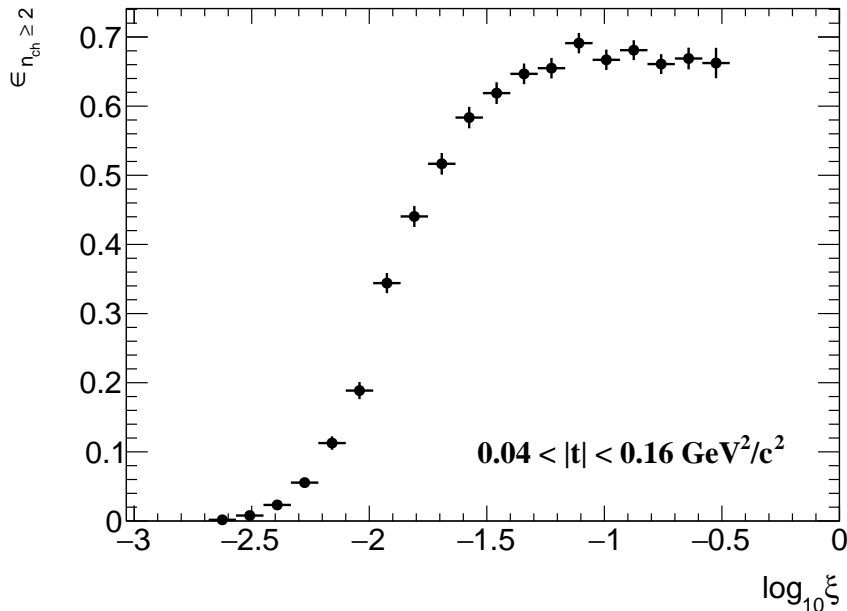


Figure 3.5:  $\epsilon_{n_{\text{ch}} \geq 2}$  as a function of  $\log_{10} \xi$  calculated from PYTHIA 8 (MBR).

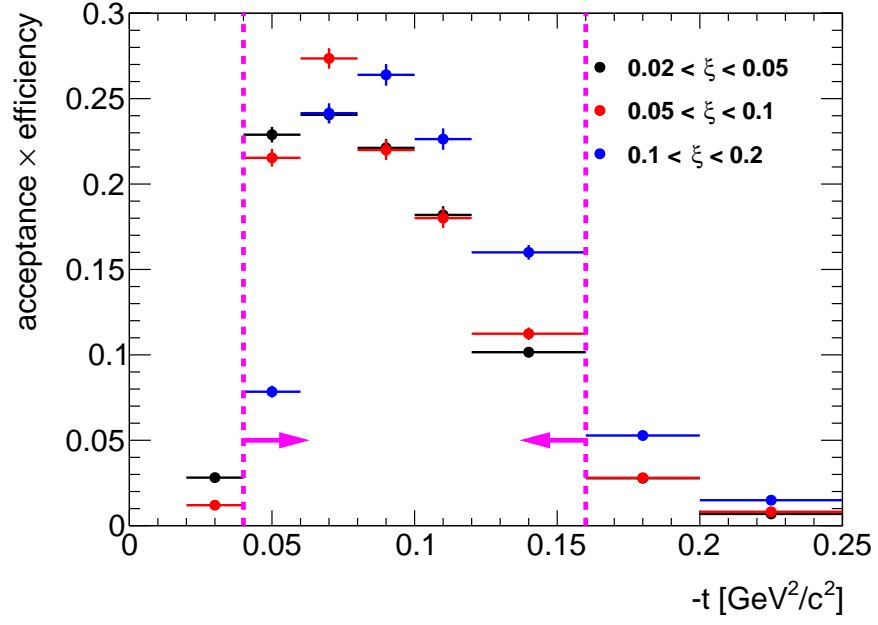


Figure 3.6: RP acceptance and track reconstruction efficiency as a function  $-t$  in three ranges of  $\xi$ , calculated using PYTHIA 8 4C (SaS). Magenta lines indicate region accepted in the analysis.

## 4. Background Contribution

The background contribution to the charged-particle distributions can be broken down into event-level and track-level backgrounds, which are described in detail in the following sections:

- Accidental background refers to events which do not originate from a single collision of two protons.
- Track backgrounds from non-primary tracks consist of secondary tracks and fake tracks; the first come mostly from decays, the short-lived particles with mean life  $30 < \tau < 300$  ps, or secondary interactions with the detector dead material, while the second comes from the track reconstruction algorithms and out-of-time pile-up with no corresponding true particles.

### 4.1 Accidental Background

The accidental backgrounds (same bunch pile-up background) are quantified using data-driven method and defined as a process where in single bunch crossing there is coincidence of two interactions, where any single-side proton signal is collected in coincidence with a signal in the TPC-TOF detector. This type of background may come from the overlap of a signal in RP (proton from beamhalo, low mass SD process without activity in TOF, elastic or low mass Central Diffraction (CD) processes with undetected proton on the other side) with a signal in TPC+TOF (mainly ND events without forward proton).

The accidental background contribution was calculated from Zerobias data, where two signatures of such background were investigated: the reconstructed proton in RP and the reconstruction of vertex from TPC tracks matched with TOF. The analysis was done for each RP arm separately and thus the Zerobias data was firstly required to pass the following criteria:

1. no trigger in any RP or trigger in exactly one arm (two RPs) with exactly one reconstructed proton track in that arm,
2. veto on any signal in small BBC tiles or ZDC on the same side of the IP as RP under consideration,
3. no or exactly one reconstructed vertex with at least two TOF-matched tracks passing the quality criteria. The latter includes also signal in BBC small tiles on the opposite side of the IP to the RP under study.

The sample of selected Zerobias data with total number of events  $N$  was divided into four classes:

$$N = N(P, S) + N(R, S) + N(P, T) + N(R, T) \quad (4.1)$$

where:  $N(P, S)$  is the number of events with reconstructed proton in exactly one RP and reconstructed TOF vertex,  $N(R, S)$  is the number of events with no trigger in any RP and reconstructed TOF vertex,  $N(P, T)$  is the number of events with reconstructed proton in exactly one RP and no reconstructed TOF vertex,  $N(R, T)$  is the number of events with no trigger in any RP and no reconstructed TOF vertex.

Since the signature of the signal is a reconstructed proton in exactly one RP and a reconstructed TOF vertex, the number of such events can be expressed as:

$$N(P, S) = N(p_3 + p_1 p_2) \quad (4.2)$$

where:  $p_1$  is the probability that there is a reconstructed proton in RP and there is no reconstructed TOF vertex,  $p_2$  is the probability that there is no reconstructed proton in RP and there is

a reconstructed TOF vertex,  $p_3$  is the probability that there is a reconstructed proton in RP and there is a reconstructed TOF vertex (not accidental).

The other classes of events given in Eq. (4.1) can be expressed in terms of the above probabilities as:

$$\begin{aligned} N(R, S) &= N(1 - p_1)p_2(1 - p_3) \\ N(P, T) &= N(1 - p_2)p_1(1 - p_3) \\ N(R, T) &= N(1 - p_1)(1 - p_2)(1 - p_3) \end{aligned} \quad (4.3)$$

Finally, the accidental background contribution  $A_{\text{bkg}}^{\text{accidental}}$  is given by:

$$A_{\text{bkg}}^{\text{accidental}} = \frac{p_1 p_2}{p_3 + p_1 p_2} = \frac{N(R, S)N(P, T)N}{N(R)N(T)N(P, S)} \quad (4.4)$$

where:  $N(R) = N(R, S) + N(R, T)$  and  $N(T) = N(P, T) + N(R, T)$ .

The shapes of the accidental background related to TPC distributions come from the above Zerobias data events which pass all the analysis selection except having no trigger in any RP. The templates corresponding to RP distributions are from protons in the above data sets but with no reconstructed TOF vertex. The normalization is given by Eq. (4.4). Figure 4.1 shows distributions of the reconstructed  $\xi$  with the accidental background contribution for events with proton reconstructed in EU, ED, WU and WD arms. Accidental background in the range of  $0.02 < \xi < 0.2$  is below 1%.

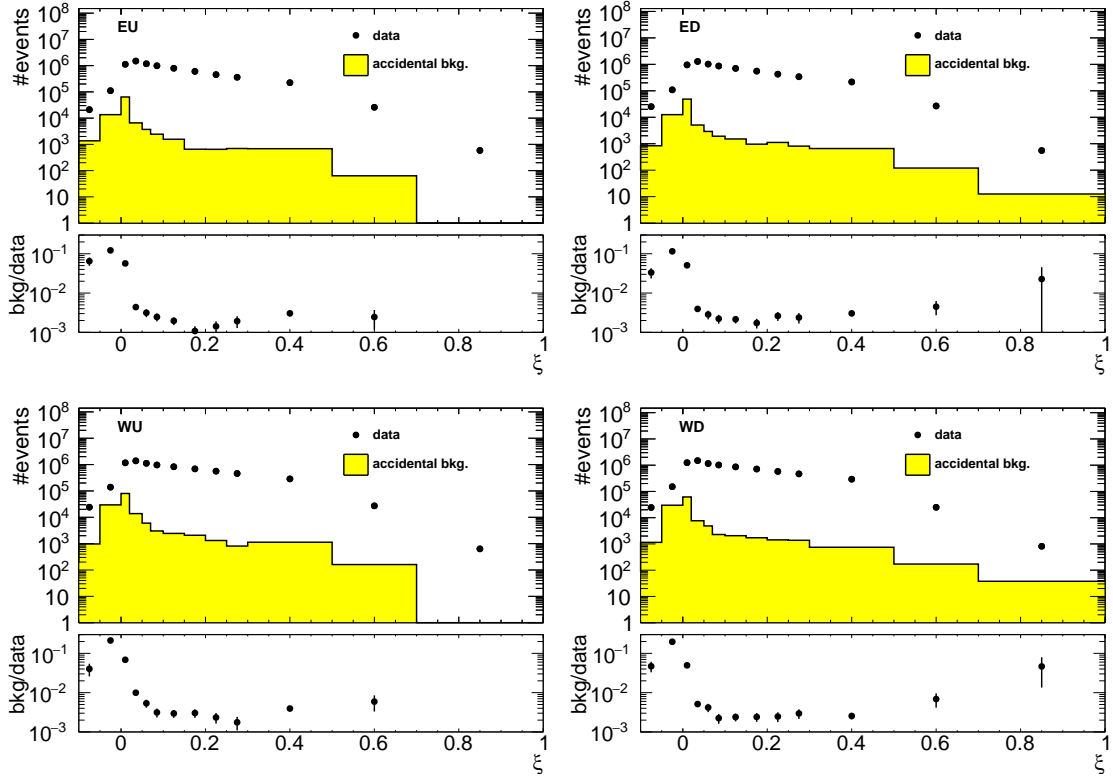


Figure 4.1: Uncorrected distributions of the reconstructed  $\xi$  for events with proton reconstructed in (top left) EU, (top right) ED, (bottom left) WU and (bottom right) WD arms. Data is shown as black markers, whereas the accidental background contribution is shown as yellow histogram. The ratio of accidental background and data is shown in the bottom pad.



The selection of Zerobias events, which is not unique, may provide some bias to the normalization of the accidental background. As a systematic check, two criteria for Zerobias selection were changed to:

1. no trigger in any RP or trigger in exactly one arm (two RPs) with *no more* than one reconstructed proton track in that arm, i.e. events with trigger signals in exactly one arm and without reconstructed proton track in that arm were also used,
2. no or exactly one reconstructed TOF vertex (*without any additional requirements*), i.e. events with a reconstructed TOF vertex that does not have at least two primary tracks satisfying the selection criteria (Sec. 3.2), or with a reconstructed TOF vertex that is out of the range of  $|V_z| < 80$  cm, were also accepted. The requirement of signal in BBC small tiles remains unchanged.

As a result of this change in the procedure, the accidental background normalization increases of about 50% with respect to the nominal value. Therefore, the background changes by  $\pm 50\%$  was taken as a systematic uncertainty related to the accidentals.

## 4.2 Background from Non-Primary Tracks

Reconstructed tracks matched to a non-primary particle, so-called background tracks, originate mainly from the following sources:

- decays of short-lived primary particles with strange quark content (mostly  $K^0$ ,  $\Lambda^0$ ),
- photons from  $\pi^0$  and  $\eta$  decays which are converting to  $e^+e^-$ ,
- hadronic interactions of particles with the beam-pipe or detector dead material.

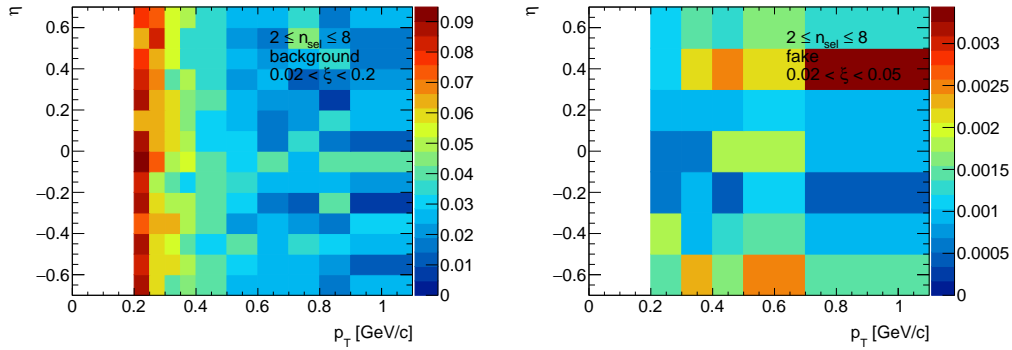


Figure 4.2: (left) Distribution of fraction of selected tracks associated with non-primary particles in the range  $0.02 < \xi < 0.2$  and (right) distribution of fraction of tracks which are not associated with true-level particles in the range  $0.02 < \xi < 0.05$  as predicted by PYTHIA 8 4C (SaS) embedding.

There is also a contribution from fake tracks, i.e. tracks not associated with true-level particles, coming from out-of-time pile-up or formed by a random combination of TPC hits. Figure 4.2 shows the background  $f_{\text{bkg}}(p_T, \eta)$  and fake track  $f_{\text{fake}}(p_T, \eta)$  contribution to reconstructed tracks as a function of  $p_T$  and  $\eta$ . There were no differences observed in the background contribution in different  $\xi$  ranges, hence, all three  $\xi$  ranges were merged for this study. The highest background fraction, which varies between 5 – 10%, was found to be at low  $p_T$ . Due to too low statistics in PYTHIA 8 embedding MC, the shape of the fake track contribution was assumed to be the same in all three  $\xi$  ranges. However, its normalization was calculated for each  $\xi$  range separately with a ratio between the ranges of 1 : 0.74 : 1.11. The change by  $\pm 100\%$  in fake track contribution was taken as a systematic uncertainty.

Figure 4.3 shows the background track contribution to reconstructed tracks as a function of  $p_T$  and  $\eta$  calculated from EPOS SD+SD'. The differences between PYTHIA 8 and EPOS, which are up to 50% for  $p_T > 0.5$  GeV/c (as shown in Fig. 4.4), were symmetrized and taken as a systematic uncertainty.

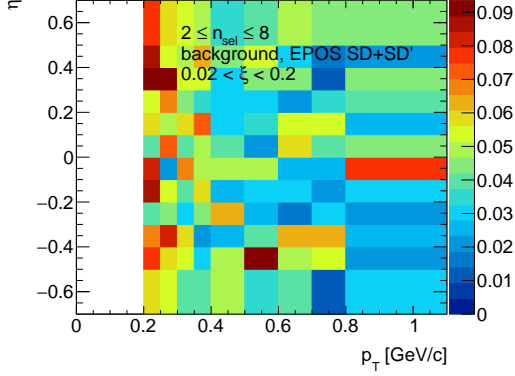


Figure 4.3: Distribution of fraction of selected tracks associated with non-primary particles as predicted by EPOS SD+SD'.

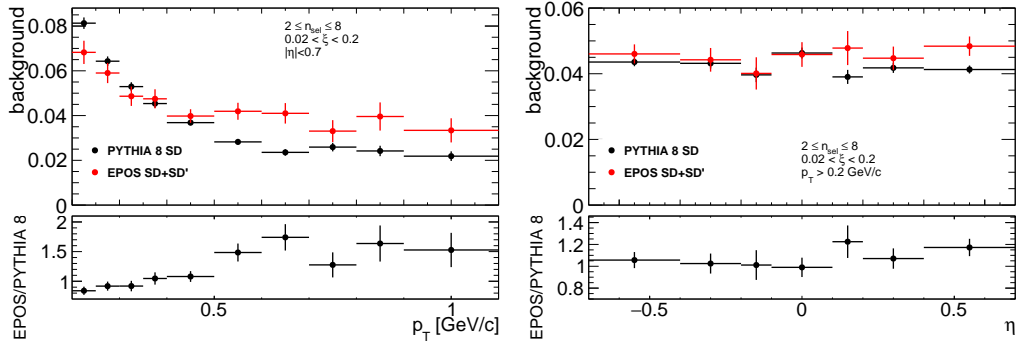


Figure 4.4: PYTHIA 8 SD and EPOS SD+SD' predictions of fraction of selected tracks associated with non-primary particles as a function of (left)  $p_T$  and (right)  $\eta$ .

## Proton Background

Secondary particles can be created due to the interaction of particles with detector dead-material. The proton sample contains background from such protons knocked out from the detector materials [13]. Most of these protons have large DCA to the primary vertex and are not associated with it. However, the protons with small DCA are included in the primary track sample. Antiprotons do not have knockout background, hence the DCA tail is almost absent in their DCA distributions.

The fraction of knock-out background protons depends on a number of factors, including the amount of detector material, analysis cuts and the  $\xi$  of diffractive proton. While it is natural to calculate the fractions of primary and background protons in the MC sample, the MC models do not necessarily predict the fraction of knock-out background protons without any bias. Hence, data-driven methods should be used to calculate this type of background.

In order to correct for the knock-out background protons, sample enriched in proton background was used for background normalization, where  $DCA_{xy}$ ,  $DCA_z$  and  $d_0$  cuts were abandoned. Additionally, at least one, instead of exactly one, reconstructed vertex was allowed in this sample. Figures 4.5 and 4.6 show the DCA distributions of protons and antiprotons, respectively, for nominal (bottom) and background enriched (top) samples. The distributions for other  $p_T$  and  $\xi$  regions are shown in Appendix A. The protons and antiprotons are selected by a  $dE/dx$

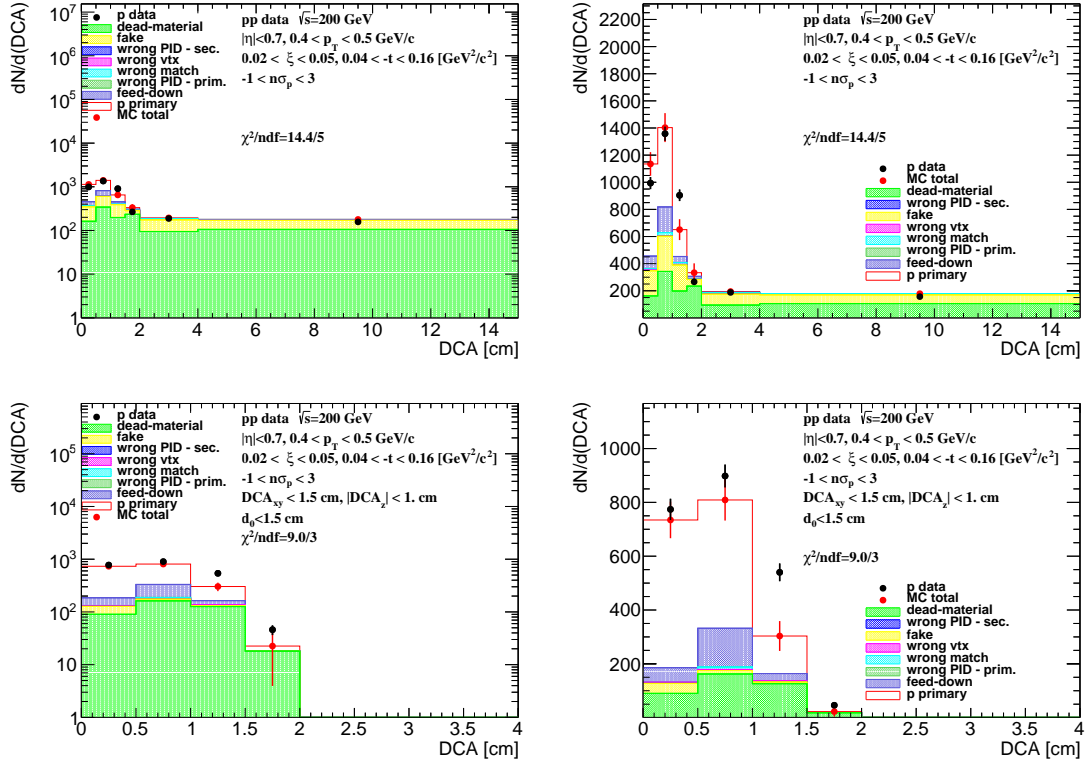


Figure 4.5: The DCA distributions of protons for  $0.4 < p_T < 0.5$  GeV/c shown for single range of  $0.02 < \xi < 0.05$  (shown in log and linear scale in left and right column, respectively). The MC contributions are shown after scaling the dead-material template to the tail of large DCA values,  $2 < \text{DCA} < 15$  cm. (top) Background enriched samples were used in the normalization procedure, whereas (bottom) the proton background was estimated from the nominal sample.

cut of  $-1 < n\sigma_{p,\bar{p}} < 3$  where  $n\sigma_{p,\bar{p}}$  is given by Eq. (8.10). In some  $p_T$  regions, the  $dE/dx$  of (anti)protons and pions starts to overlap, hence, the asymmetric  $n\sigma_{p,\bar{p}}$  cut was introduced in order to select as clean (anti)proton sample as possible. The fraction of knock-out protons within the selected sample is determined via MC template fits. The templates of reconstructed tracks with  $dE/dx$  corresponding to the proton and antiproton are obtained from PYTHIA 8 embedding MC separately for:

- primary (anti)protons,
- knock-out background protons (labeled as dead-material),
- fake tracks,
- secondary particles with  $dE/dx$  of (anti)proton (labeled as wrong PID - sec.),
- tracks associated with primary (anti)protons, but with the reconstructed vertex not matched to true-level primary vertex (labeled as wrong vtx),
- reconstructed track is partially matched to true-level particle (labeled as wrong match, track to true-level particle matching is described in [1]), i.e. track and true-level particle have appropriate number of common hit points but the distance between true-level particle and track is too large,  $\delta^2(\eta, \phi) > (0.15)^2$ , thus, track is not considered as primary particle according to discussion in [1],

- primary particles with  $dE/dx$  of (anti)proton (labeled as wrong PID - prim.),
- (anti)proton as a product of short-lived decays, mainly  $\Lambda^0$  (labeled as feed-down).

First, the background enriched sample was analyzed (Fig. 4.5, top), where the template of knock-out background protons was normalized to the number of events in the fake-subtracted tail of the DCA distribution,  $2 < \text{DCA} < 15$  cm. Next the knock-out proton and fake background was subtracted from the DCA distribution and the sum of other templates was normalized to the number of events in the signal region,  $\text{DCA} < 1.5$  cm.

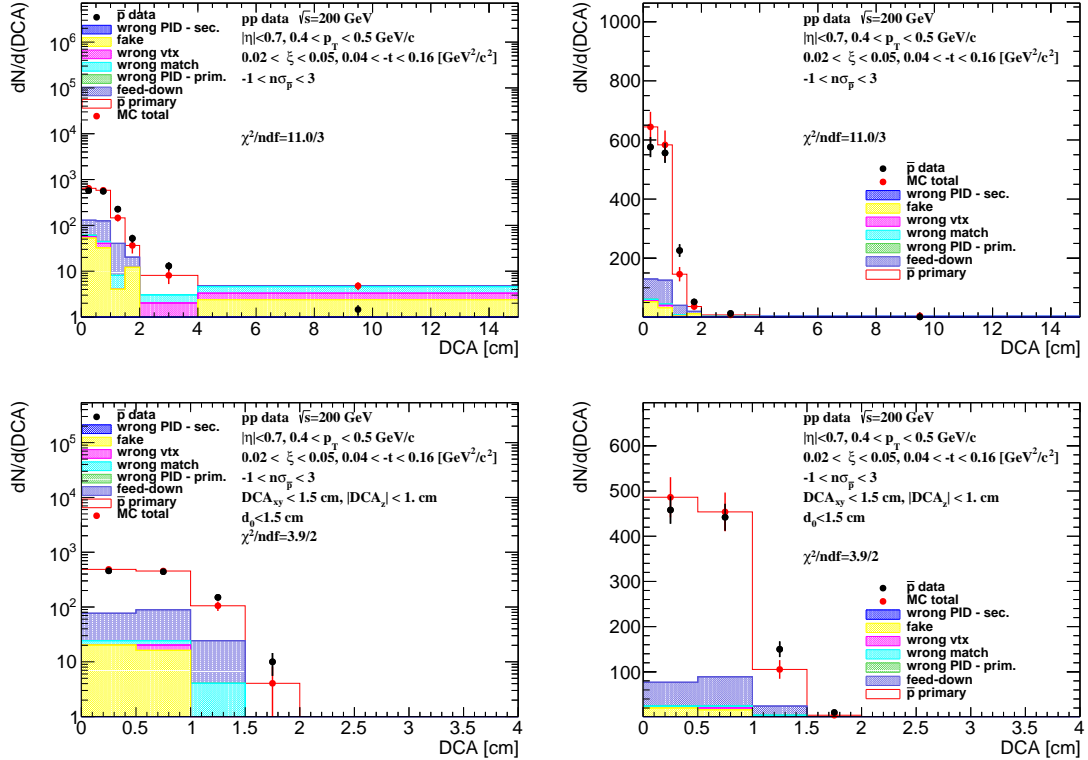


Figure 4.6: The DCA distributions of antiprotons for  $0.4 < p_T < 0.5$  GeV/c shown for one range of  $0.02 < \xi < 0.05$  (log and linear scale in left and right column, respectively). The MC contributions are shown as colour histograms. (top) Background enriched and (bottom) nominal samples were used.

The fraction of the knock-out proton background in the signal region,  $\text{DCA} < 1.5$ , was estimated from the nominal sample (Fig. 4.5, bottom), where  $\text{DCA}_{xy}$ ,  $\text{DCA}_z$  and  $d_0$  track cuts were applied and exactly one reconstructed vertex was required. The normalization of each MC contribution was kept the same as that estimated for the background enriched sample. Figure 4.7 shows the knock-out proton background as a function of  $p_T$  in three ranges of  $\xi$ . The following functional form was found to describe the background protons:

$$f_{\text{bkg}}^p(p_T) = p_0 \exp(p_1 p_T) \quad (4.5)$$

where  $p_0$  and  $p_1$  are free parameters obtained from a fit.

The obtained fraction of knock-out background protons is approximately 20% at  $p_T = 0.45$  GeV/c and less than 10% at  $p_T = 1.0$  GeV/c. In PYTHIA 8 SD predictions (also shown in Fig. 4.5), such fraction is much smaller and equals to approximately 7% at  $p_T = 0.45$  GeV/c and about 5% at  $p_T = 1.0$  GeV/c. This may suggest that there are differences in the amount of dead material in front of TPC between data and simulation, which is consistent with the studies presented in [1].

Figure 4.6 shows the corresponding DCA distributions with MC templates for antiprotons, where the background from knock-out particles is not present. Therefore, there was no need for any fit to be performed in this comparison. The MC templates fairly well describe the DCA distribution for both, protons, after tuning the fraction of knock-out background to data, and antiprotons.

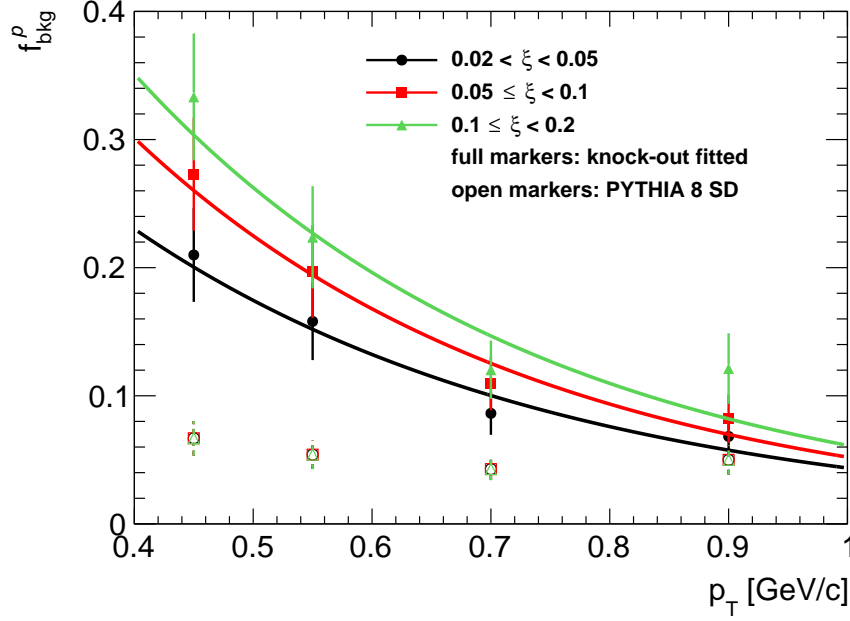


Figure 4.7: The fraction of knock-out proton background as a function of  $p_T$  in three ranges of  $\xi$  with fitted parametrizations. Full markers represent fitted knock-out background and open markers represent PYTHIA 8 SD predictions.

#### Systematic Uncertainty Related to Proton Background

The knock-out proton background estimation introduces systematic uncertainties. First, the normalization interval of the knock-out proton background template in the background enriched sample was changed to  $4 < \text{DCA} < 15$  cm. This introduced a relative systematic uncertainty of up to 30% for  $p_T \approx 0.9$  GeV/c.

The knock-out proton background contribution was parameterized as it is shown in Eq. (4.5). The systematic uncertainty related to the parameterization procedure was estimated by varying the parameters,  $p_0$  and  $p_1$ , by their statistical uncertainties ( $\pm 1\sigma$ ). As a result, a relative systematic uncertainties of about 10% were obtained.

Differences in the shape of the DCA distribution between data and MC can affect the knock-out proton background estimation procedure. Figure 4.8 (top left) shows the data to MC ratio of the number of events in the background dominated region,  $2 < \text{DCA} < 15$  cm. Since this region is used to estimate background normalization, and the shape of the DCA distribution in the data differs from that observed in the simulation, the predicted background in the  $\text{DCA} < 1.5$  cm region can change. Thus, the following functional form was used to estimate the slope between data and MC:

$$\frac{\text{data}}{\text{MC}}(\text{DCA}) = A(\text{DCA} - 8.5) + B \quad (4.6)$$

where  $A$  (slope) and  $B$  are fit free parameters. Differences in slope between data and MC were used to estimate how many more background tracks would fit into the signal region and a systematic uncertainty, which varies up to 5% for  $0.02 < \xi < 0.05$ , was introduced.

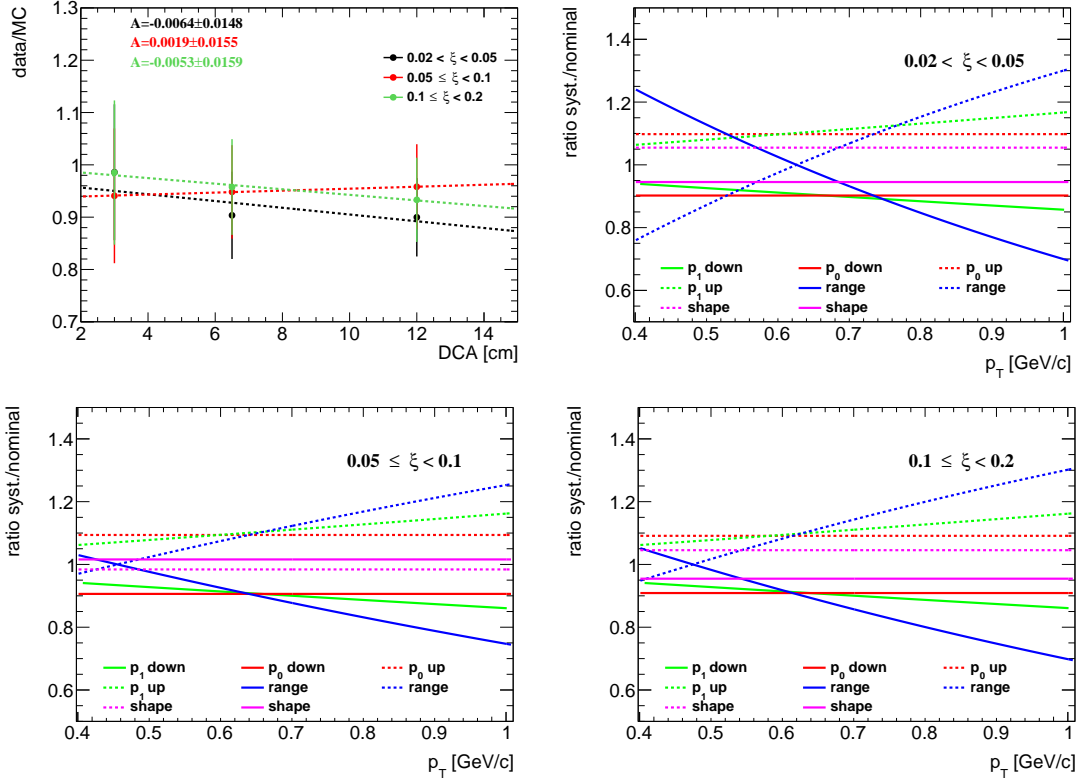


Figure 4.8: (top left) Data to MC ratio of the number of events in the background dominated region in three ranges of  $\xi$  with fitted functional form given by Eq. (4.6). (top right and bottom) Components of the systematic uncertainty related to the knock-out background protons contribution, shown in Fig. 4.8, are added in quadrature. Those related to the fit range and the shape of the proton background are symmetrized. Figure 4.9 shows the fraction of knock-out proton background in three ranges of  $\xi$  and the total systematic uncertainty related to it.

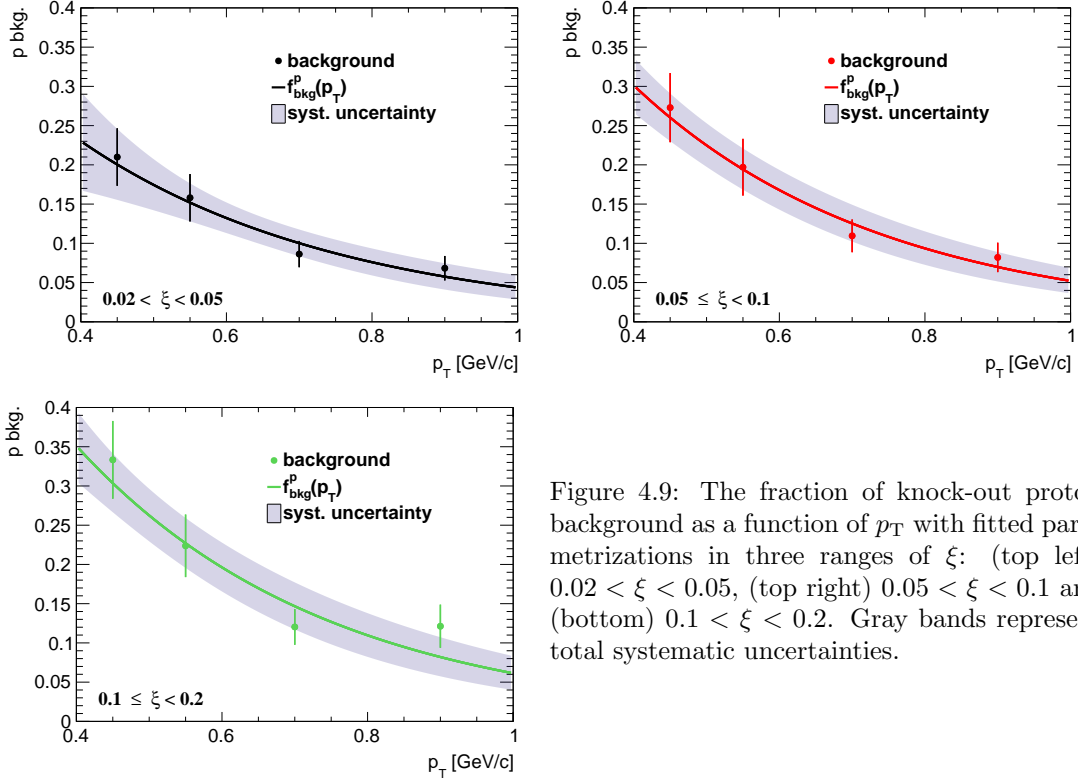


Figure 4.9: The fraction of knock-out proton background as a function of  $p_T$  with fitted parametrizations in three ranges of  $\xi$ : (top left)  $0.02 < \xi < 0.05$ , (top right)  $0.05 \leq \xi < 0.1$  and (bottom)  $0.1 \leq \xi < 0.2$ . Gray bands represent total systematic uncertainties.

## Pion Background

The pion spectra are corrected for weak decays (mainly of  $K_S^0$  and  $\Lambda^0$ ), muon contribution and background from the detector dead-material interactions. The pion decay muons can be identified as pions due to the similar masses. These contributions are obtained from PYTHIA 8 SD. Figure 4.10 shows the background contribution to the pion spectra as a function of  $p_T$  in three ranges of  $\xi$ , separately for  $\pi^-$  and  $\pi^+$ . Since there were negligible differences observed between these three ranges of  $\xi$ , the background contribution was averaged over  $\xi$ . The following parametrization was found to describe it:

$$f_{\text{bkg}}^\pi(p_T) = a_0 \exp(a_1 p_T) + a_2 p_T^2 + a_3 p_T \quad (4.7)$$

where  $a_i$ ,  $i = 0, \dots, 3$  are free parameters of the fitted function.

The pion background contribution varies between 5% at low- $p_T$  ( $p_T = 0.25$  GeV/c) and about 1% at  $p_T = 1.0$  GeV/c for both negatively and positively charged pions. In addition, the background was calculated from EPOS SD+SD' for the full range of  $\xi$ . The differences between PYTHIA 8 and EPOS are up to 1% for  $\pi^-$ .

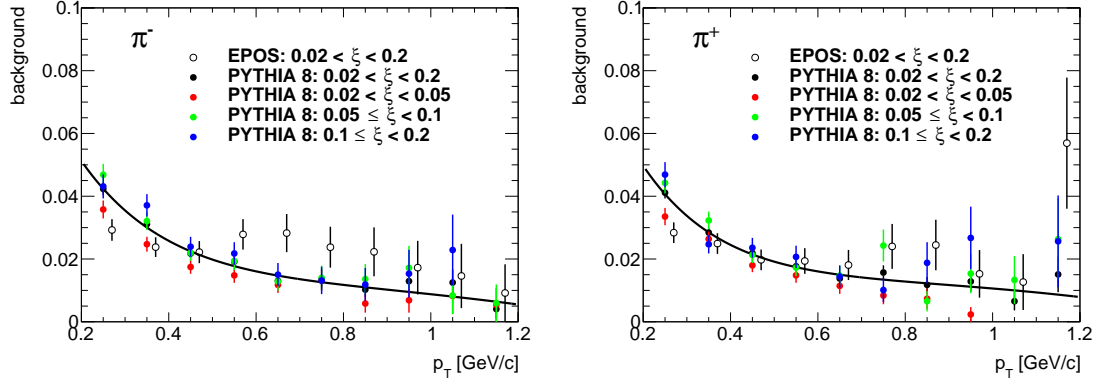


Figure 4.10: Pion background fraction as a function of  $p_T$  calculated from PYTHIA 8 and shown separately for (left) negatively and (right) positively charged pions in three ranges of  $\xi$ : (red)  $0.02 < \xi < 0.05$ , (green)  $0.05 < \xi < 0.1$ , (blue)  $0.1 < \xi < 0.2$ . (full black points) The pion background averaged over three ranges of  $\xi$  with fitted parametrization is also shown. Open black points represent EPOS predictions for the full  $\xi$  range.



## 5. Non-SD Contributions

Events, in which forward proton and reconstructed TOF vertex are the result of the same  $pp$  interaction, may originate from ND, DD, SD, and CD processes. Their relative contributions must be estimated from MC models and are therefore model dependent. Tracks reconstructed in RPs may also be:

- forward protons produced in the SD, CD or DD diffractive systems or from ND events,
- secondary particles from showering initiated by interaction of forward protons with beam-line elements. This contribution is equal to approximately 2%.

Figure 5.1 shows the uncorrected  $\xi$  and  $t$  distributions in data compared to various MC models: PYTHIA 8 A2 (MBR), PYTHIA 8 A2 (MBR-tuned) and EPOS. The MC distributions are split into SD, ND, DD and CD components. For EPOS, SD' is separated from the ND events. Additionally, the accidental background is also shown. PYTHIA 8 A2 (MBR-tuned) predictions agree much better with the data than PYTHIA 8 A2 (MBR) and result also in a suppression of non-SD events. EPOS describes data better than PYTHIA 8 but shows a dominant contribution of SD' events. All MCs predict significant DD and ND background at large  $\xi$ , thereby the analysis was limited to  $\xi < 0.2$ .

Figures 5.2 to 5.4 show the uncorrected distributions of variables used in the later analysis:  $n_{\text{sel}}$ ,  $p_T$  and  $\bar{\eta}$ . The contributions from non-SD (except EPOS-SD') interactions differ a bit between each other, i.e. EPOS predicts significantly larger CD contribution, whereas DD and ND are suppressed in PYTHIA 8 A2 (MBR-tuned). PYTHIA 8 A2 (MBR) is used as the default model of non-SD contribution subtracted from the data with systematic uncertainty  $\pm 50\%$ , which covers all differences between the models except EPOS-SD'. In this analysis EPOS-SD' is considered as an alternative to PYTHIA 8 SD model of events with forward proton in the final state, where one of the proton remnants hadronizes back to a single proton (non-diffractive process), while in PYTHIA 8 the initial proton stays intact (diffractive process). As a consequence, results are compared with the sum of SD and SD' processes for EPOS model.

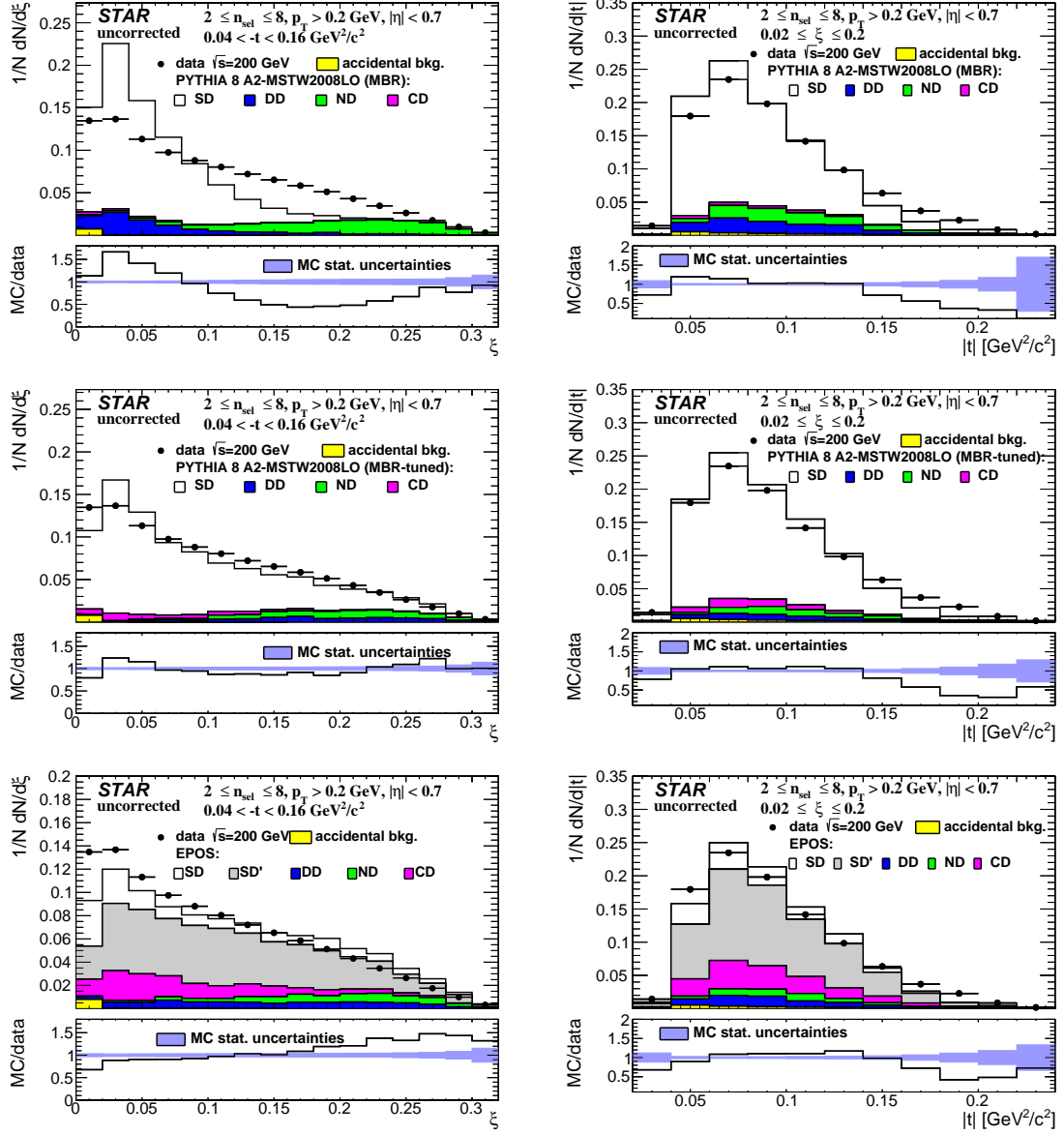


Figure 5.1: Uncorrected distributions of data compared to various MC models: (top) PYTHIA 8 A2 (MBR), (middle) PYTHIA 8 A2 (MBR-tuned) and (bottom) EPOS, as a function of (left column)  $\xi$  and (right column)  $|t|$ .

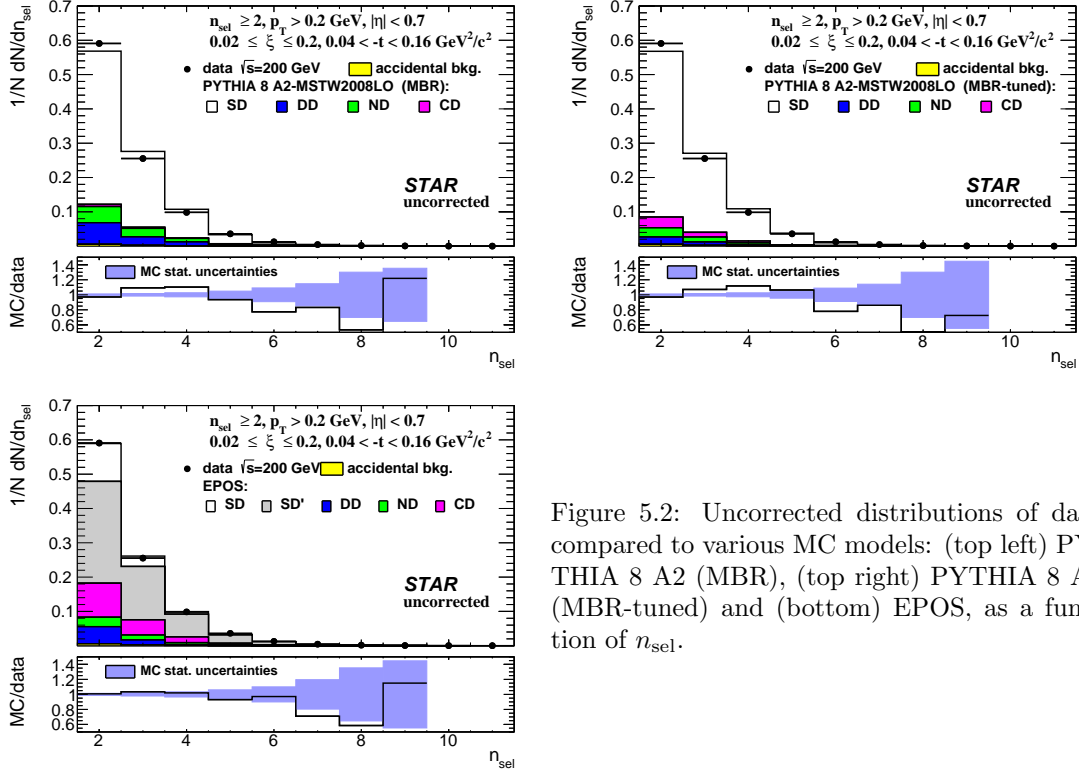


Figure 5.2: Uncorrected distributions of data compared to various MC models: (top left) PYTHIA 8 A2 (MBR), (top right) PYTHIA 8 A2 (MBR-tuned) and (bottom) EPOS, as a function of  $n_{\text{sel}}$ .

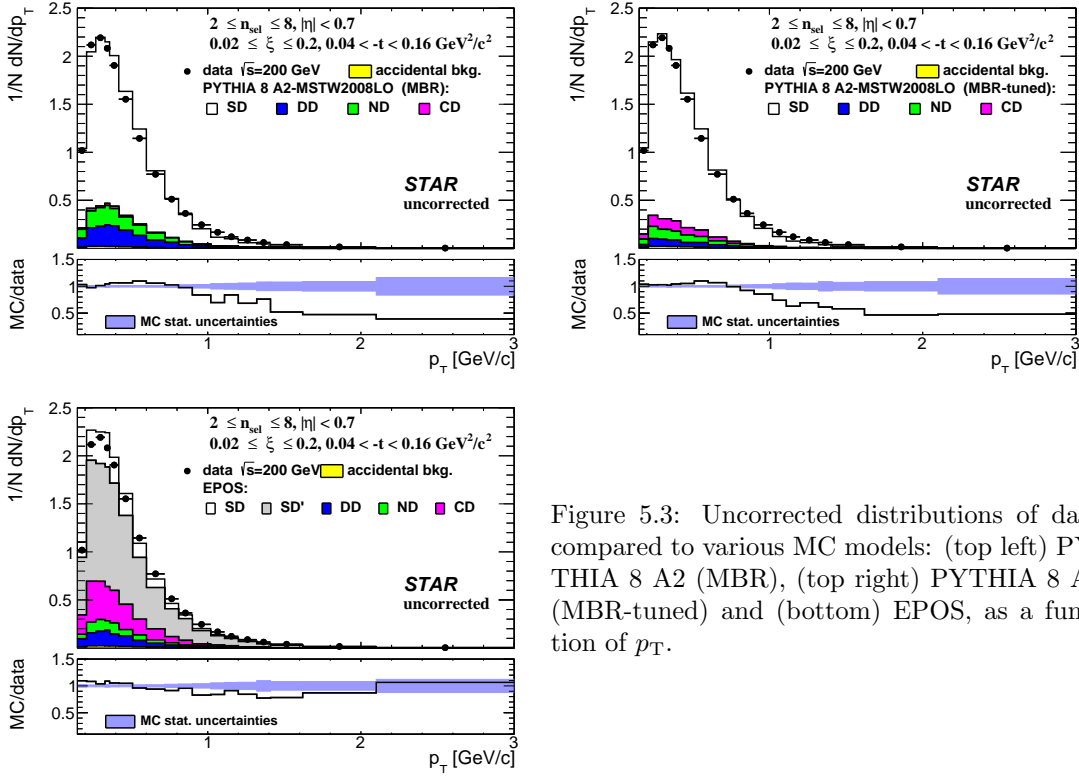


Figure 5.3: Uncorrected distributions of data compared to various MC models: (top left) PYTHIA 8 A2 (MBR), (top right) PYTHIA 8 A2 (MBR-tuned) and (bottom) EPOS, as a function of  $p_T$ .

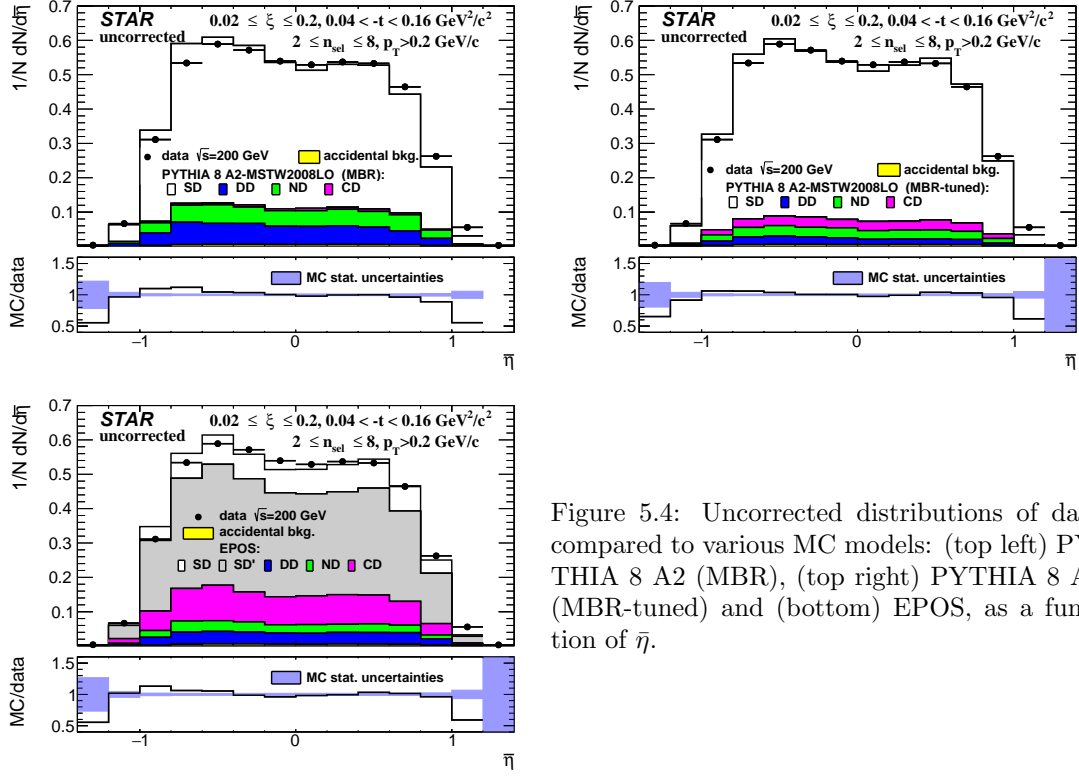


Figure 5.4: Uncorrected distributions of data compared to various MC models: (top left) PYTHIA 8 A2 (MBR), (top right) PYTHIA 8 A2 (MBR-tuned) and (bottom) EPOS, as a function of  $\eta$ .

# 6. Selection Efficiencies

## 6.1 Vertex Reconstruction

When the charged-particle multiplicity is low, the vertex finding algorithm sometimes fails to find the primary vertex. In addition, at high luminosity, vertex finder can fail due to the contribution of pile-up interactions and providing a wrong reconstructed vertex. In the study of vertex reconstruction efficiency we required at least two reconstructed global tracks  $n_{\text{sel}}^{\text{global}} \geq 2$  passing all the quality cuts listed in Sec 3.2, except vertex-related cuts on  $\text{DCA}_{xy}$  and  $\text{DCA}_z$ , and associated to true-level primary particles. Additionally, MC events were accepted if the  $z$ -coordinate of the true-level primary vertex was between  $-80$  and  $80$  cm and  $n_{\text{ch}} \geq 2$ . All corrections, described in this section, were calculated in three ranges of  $\xi$  separately using PYTHIA 8 SD embedding MC.

The global tracks (not necessarily associated to a true-level primary particles), which are used by the vertex-finder algorithm, had to pass the following quality cuts:

1. Tracks must be matched with hits reconstructed in TOF,
2. The number of the TPC hits used in the helix fit  $N_{\text{hits}}^{\text{fit}}$  must be greater than 20,
3. The ratio of the number of TPC hits used in the helix fit to the number of possible TPC hits  $N_{\text{hits}}^{\text{fit}}/N_{\text{hits}}^{\text{poss}}$  must be greater than 0.52,
4. The transverse impact parameter with respect to the beamline  $d_0$  must be less than 2 cm,
5. The track's transverse momentum  $p_T$  must be greater than 0.2 GeV/c.

The above track selection criteria are different than those used in the nominal analysis. Primary vertex reconstruction efficiency and fake vertex rate were calculated as a function of the number of global tracks used in vertexing  $n_{\text{vrt}}^{\text{global}}$  instead of  $n_{\text{sel}}^{\text{global}}$  ( $n_{\text{vrt}}^{\text{global}} \geq n_{\text{sel}}^{\text{global}}$ ).

In the nominal analysis exactly one vertex with  $n_{\text{sel}} \geq 2$  is required. However, in the study of vertex reconstruction, events with additional vertices were studied. Therefore, we define the best vertex as the reconstructed vertex with the highest number of TOF-matched tracks. This vertex does not have to be associated to true-level primary vertex (fake or secondary vertex). The algorithm, which matches reconstructed vertices to true-level vertices, checks for reconstructed tracks originating from them. If at least one reconstructed track is assigned to a true-level particle, then the reconstructed vertex is assigned to the true-level vertex from which the true-level particle originates. Since the fake vertices (not matched to the true-level primary vertex) are allowed in the analysis, the overall vertex-finding efficiency,  $\epsilon_{\text{vrt}}(n_{\text{vrt}}^{\text{global}})$ , is expressed as:

$$\epsilon_{\text{vrt}}(n_{\text{vrt}}^{\text{global}}) = \epsilon_{\text{vrt}}^{\text{best}}(n_{\text{vrt}}^{\text{global}}) + \delta_{\text{vrt}}^{\text{fake}}(n_{\text{vrt}}^{\text{global}}) \quad (6.1)$$

where:

$\epsilon_{\text{vrt}}^{\text{best}}(n_{\text{vrt}}^{\text{global}})$  is the primary vertex reconstruction efficiency, determined as the ratio of the number of good reconstructed events (best primary vertex with  $n_{\text{sel}} \geq 2$  matched to the true-level primary vertex) to the number of input MC events,

$\delta_{\text{vrt}}^{\text{fake}}(n_{\text{vrt}}^{\text{global}})$  is the fake vertex rate, determined as the ratio of the number of good reconstructed events (best primary vertex with  $n_{\text{sel}} \geq 2$  not matched to the true-level primary vertex) to the number of input MC events. Due to the contribution of pile-up, it is possible that the best vertex originates from fake tracks instead of true-level particles.

501 The vertex-finding efficiency as a function of  $n_{\text{vrt}}^{\text{global}}$  is shown in Fig. 6.1 (left) and it is larger  
 502 than 75% for all  $n_{\text{vrt}}^{\text{global}}$ . However, for  $n_{\text{vrt}}^{\text{global}} > 8$ , there are more fake than true-level primary  
 503 vertices. When there are exactly two global tracks used in the vertex reconstruction,  $n_{\text{vrt}}^{\text{global}} = 2$ ,  
 504 the vertex-finding efficiency depends on the longitudinal distance between these tracks  $|\Delta z_0|$ .  
 505 Therefore, the vertex finding efficiency for such events  $\epsilon_{\text{vrt}}(|\Delta z_0|)$  is given by:

$$\epsilon_{\text{vrt}}(|\Delta z_0|) = \epsilon_{\text{vrt}}^{\text{best}}(|\Delta z_0|) + \delta_{\text{vrt}}^{\text{fake}}(|\Delta z_0|) \quad (6.2)$$

506 where:  $\epsilon_{\text{vrt}}^{\text{best}}(|\Delta z_0|)$  is the primary vertex reconstruction efficiency,  $\delta_{\text{vrt}}^{\text{fake}}(|\Delta z_0|)$  is the fake vertex  
 507 rate.

508 Figure 6.1 (right) shows the vertex finding efficiency for events with  $n_{\text{vrt}}^{\text{global}} = 2$ . This efficiency  
 509 is smaller than 20% for tracks with  $|\Delta z_0| > 2$  cm, hence the analysis was limited to events with  
 510  $|\Delta z_0| < 2$  cm, when  $n_{\text{vrt}}^{\text{global}} = 2$ . The rate of fake vertices is negligibly low (open points overlap  
 with full points).

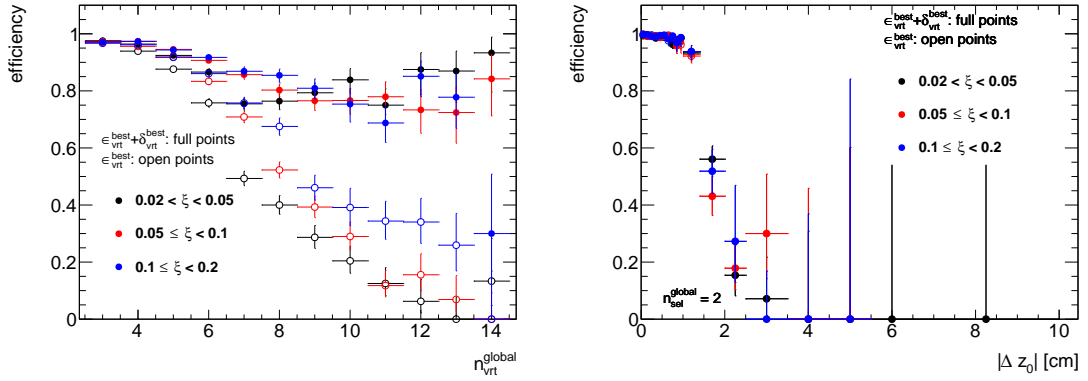


Figure 6.1: Vertex-finding efficiency in three ranges of  $\xi$  as a function of (left)  $n_{\text{vrt}}^{\text{global}}$  and (right) with respect to the  $|\Delta z_0|$  between reconstructed tracks in events with  $n_{\text{vrt}}^{\text{global}} = 2$ .

511 Events are rejected if more vertices are reconstructed in addition to the best one. Rejected  
 512 events can be classified as:  
 513

- 514 a) two or more additional vertices,
- 515 b) additional secondary vertex from interactions with the detector dead-material,
- 516 c) additional fake vertex,
- 517 d) additional primary vertex (vertex splitting or background vertex reconstructed as best ver-
- 518 tex),
- 519 e) additional secondary vertex from the decay.

520 The fraction of such events,  $f_{\text{veto}}^{\text{veto}}(n_{\text{vrt}}^{\text{global}})$ , is given by:

$$f_{\text{vrt}}^{\text{veto}}(n_{\text{vrt}}^{\text{global}}) = \frac{\text{number of events with more than one reconstructed TOF vertex}}{\text{number of events with at least one reconstructed TOF vertex}} \quad (6.3)$$

$$= f_a - f_b - f_c - f_d - f_e$$

521 where  $f_a$  to  $f_e$  are the fractions of events with additional vertices, whose labels are listed above.  
 522 As before, the fraction was calculated as a function of  $|\Delta z_0|$  for events with  $n_{\text{vrt}}^{\text{global}} = 2$ .  
 523 Figure 6.2 shows the fraction of multi-vertex events with respect to the  $n_{\text{vrt}}^{\text{global}}$ . There is a large  
 524 fraction of events ( $> 90\%$ ) with additional background vertices for  $n_{\text{vrt}}^{\text{global}} \geq 9$ , what would result

in large correction factor. Hence, the analysis was limited to events with  $n_{\text{sel}}^{\text{global}} \leq 8$  ( $n_{\text{sel}}^{\text{global}} \leq n_{\text{vrt}}^{\text{global}}$ ). The total fraction of multi-vertex events,  $f_a + f_b + f_c + f_d + f_e$ , as a function of  $n_{\text{vrt}}^{\text{global}}$  and  $|\Delta z_0|$ , shown in Fig. 6.3, demonstrates that  $f_{\text{vrt}}^{\text{veto}}(|\Delta z_0|)$  is very small ( $< 2\%$ ) for events with  $n_{\text{vrt}}^{\text{global}} = 2$ .

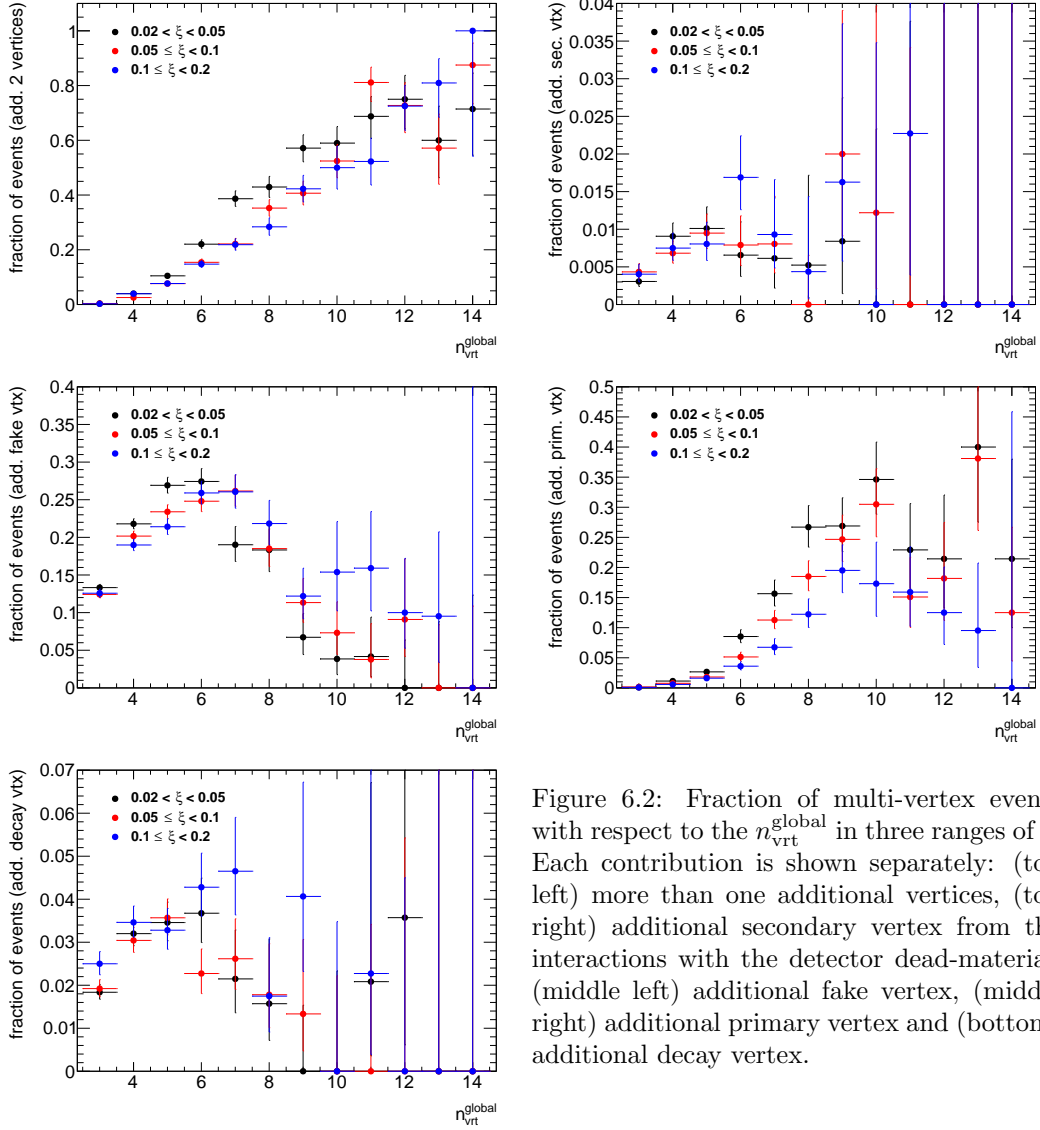


Figure 6.2: Fraction of multi-vertex events with respect to the  $n_{\text{vrt}}^{\text{global}}$  in three ranges of  $\xi$ . Each contribution is shown separately: (top left) more than one additional vertices, (top right) additional secondary vertex from the interactions with the detector dead-material, (middle left) additional fake vertex, (middle right) additional primary vertex and (bottom) additional decay vertex.

Although, the analysis was limited to  $n_{\text{sel}}^{\text{global}} \leq 8$  ( $n_{\text{sel}}^{\text{global}} \leq n_{\text{vrt}}^{\text{global}}$ ), a fraction of events with additional background vertices was still relatively large. Since most of these additional vertices are fake (and as accidental not correlated with true-level primary distributions), it was checked whether the charged-particle multiplicity distributions are different for events with and without reconstructed fake vertices. These distributions, as shown in Fig 6.4, are in good agreement, thus, above studies of vertex reconstruction were repeated using MC events that do not contain reconstructed fake vertices. It means that events with additional fake vertex were rejected (similarly to the analysis of real data) and no correction is needed for such losses since it only affects overall normalization (not the shapes of distributions under study). The vertex finding efficiency, which was calculated from such events, is shown in Fig. 6.5. It is greater than 95% for events with  $2 \leq n_{\text{vrt}}^{\text{global}} \leq 8$ . In addition, the corresponding fraction of multi-vertex events, shown in Figs. 6.6 and 6.7, is smaller than 20%. Since fake vertices were rejected from this study, the  $f_c$  term from

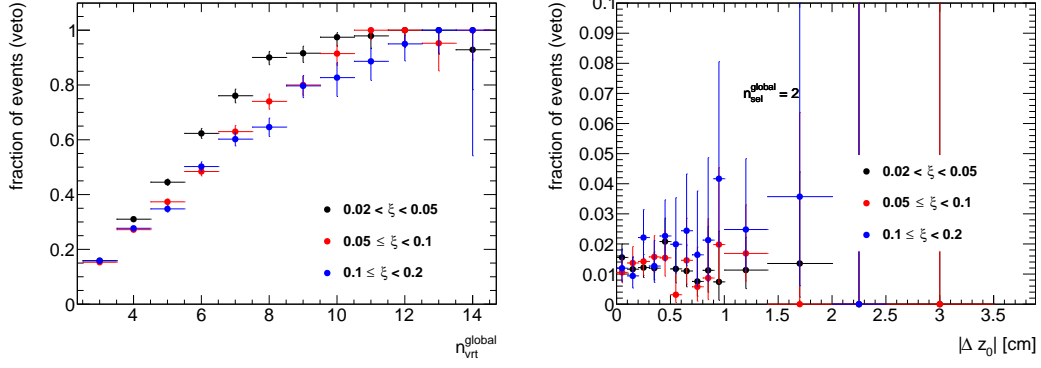


Figure 6.3: Total fraction of multi-vertex events as a function of (left)  $n_{\text{vrt}}^{\text{global}}$  for events with  $n_{\text{vrt}}^{\text{global}} > 2$  and (right)  $|\Delta z_0|$  for events with  $n_{\text{vrt}}^{\text{global}} = 2$  in three ranges of  $\xi$ .

Eq. (6.3) is equal to 0. The correction factors calculated from MC events that do not contain reconstructed fake vertices were used in the analysis instead of the one obtained from the full MC sample.

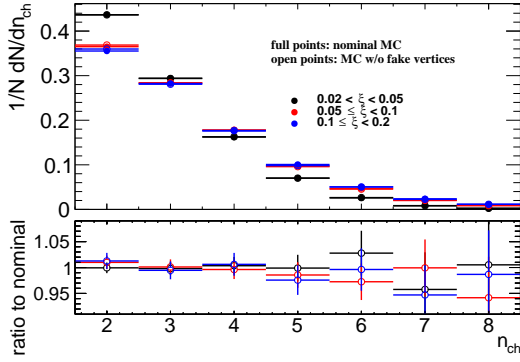


Figure 6.4: Normalized charged-particle multiplicity distributions in three ranges of  $\xi$  calculated from PYTHIA 8 SD embedding MC for (full points) all generated events and (open points) events without reconstructed fake vertices.

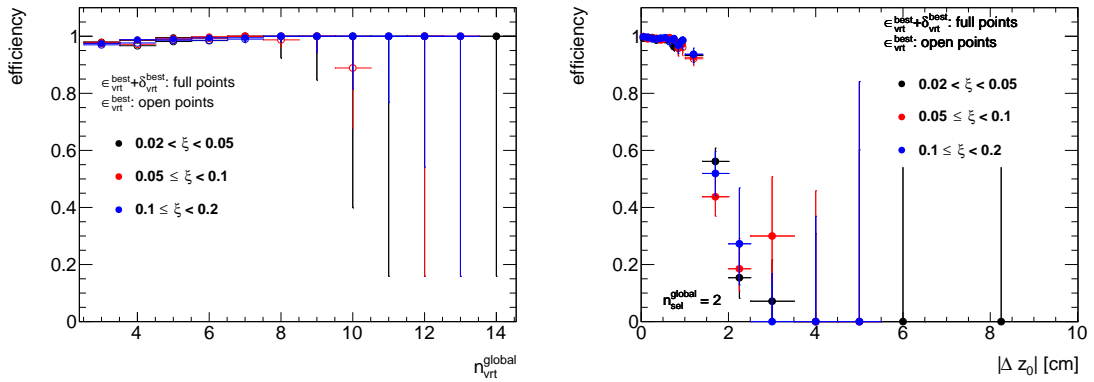


Figure 6.5: Vertex-finding efficiency in three ranges of  $\xi$  as a function of (left)  $n_{\text{vrt}}^{\text{global}}$  and (right) with respect to the  $|\Delta z_0|$  between reconstructed tracks in events with  $n_{\text{vrt}}^{\text{global}} = 2$ . Only events that do not contain additional fake vertices were used.



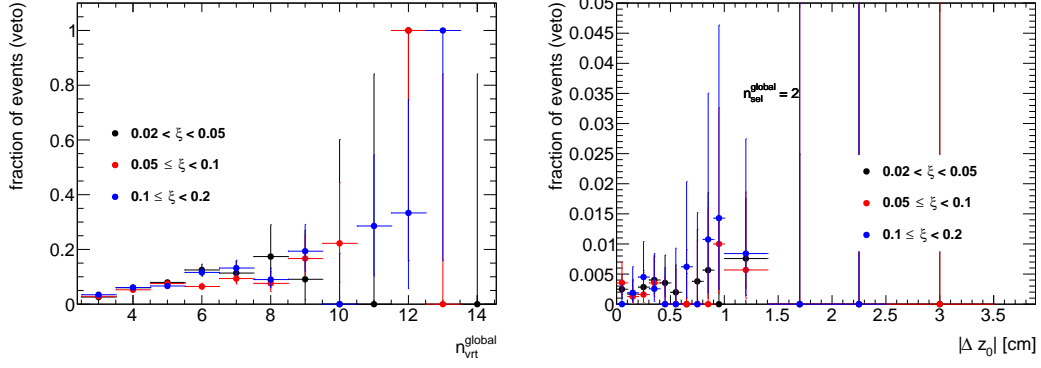


Figure 6.6: Total fraction of multi-vertex events as a function of (left)  $n_{\text{vrt}}^{\text{global}}$  for events with  $n_{\text{vrt}}^{\text{global}} > 2$  and (right)  $|\Delta z_0|$  for events with  $n_{\text{vrt}}^{\text{global}} = 2$  in three ranges of  $\xi$ . Only events that do not contain additional fake vertices were used.

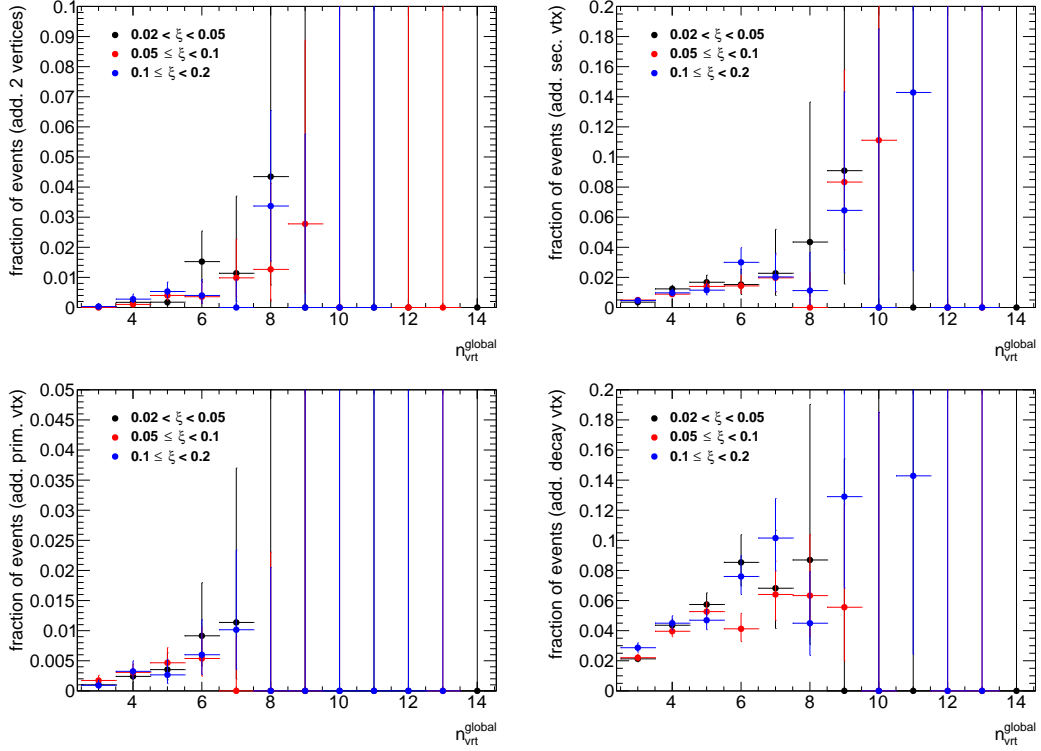


Figure 6.7: Fraction of multi-vertex events with respect to the  $n_{\text{vrt}}^{\text{global}}$  in three ranges of  $\xi$ . Each contribution is shown separately: (top left) more than one additional vertices, (top right) additional secondary vertex from the interactions with the detector dead-material, (bottom left) additional primary vertex and (bottom right) additional decay vertex. Only events that do not contain additional fake vertices were used.

## 6.2 Correction to BBC-Small

The SDT trigger conditions imposed signal in RPs and veto on any signal in the same-side small BBC tiles, whereas signal in the opposite-side BBC-small was required by the offline event selection. These requirements were imposed in order to accept only events with rapidity gap and

548 reduce DD, ND and accidental backgrounds. A joined BBC-small efficiency,  $\epsilon_{\text{BBC}}$ , was obtained  
 549 as a function of each measured quantity using PYTHIA 8 4C (SaS) embedded into Zerobias data,  
 550 EPOS SD+SD' and HERWIG MC. The efficiency was calculated for events within fiducial region  
 551 as follows:

$$\epsilon_{\text{BBC}} = \frac{\text{number of MC events satysfying the BBC-small selection criteria}}{\text{number of MC events}} \quad (6.4)$$

552 Figures 6.8 to 6.10 show the fraction of generated true-level MC events, within the fiducial re-  
 553 gion of the measurement, in which the selection criteria on BBC-small signal and veto are fulfilled.  
 554 The efficiency weakly dependents on the measured variables ( $n_{\text{ch}}$ ,  $p_{\text{T}}$  and  $\bar{\eta}$ ). In addition, veto,  
 555 signal and joined BBC-small efficiencies are presented separately as a function of  $\xi$  in Fig. 6.11.  
 556 The  $\epsilon_{\text{BBC}}$  strongly depends on  $\xi$  and varies from about 90% for events with  $\xi$  within 0.02 – 0.05  
 557 to about 60% for events with  $0.1 < \xi < 0.2$ . However, measurements of corrected  $\xi$  distributions  
 558 are out of the scope of this analysis.

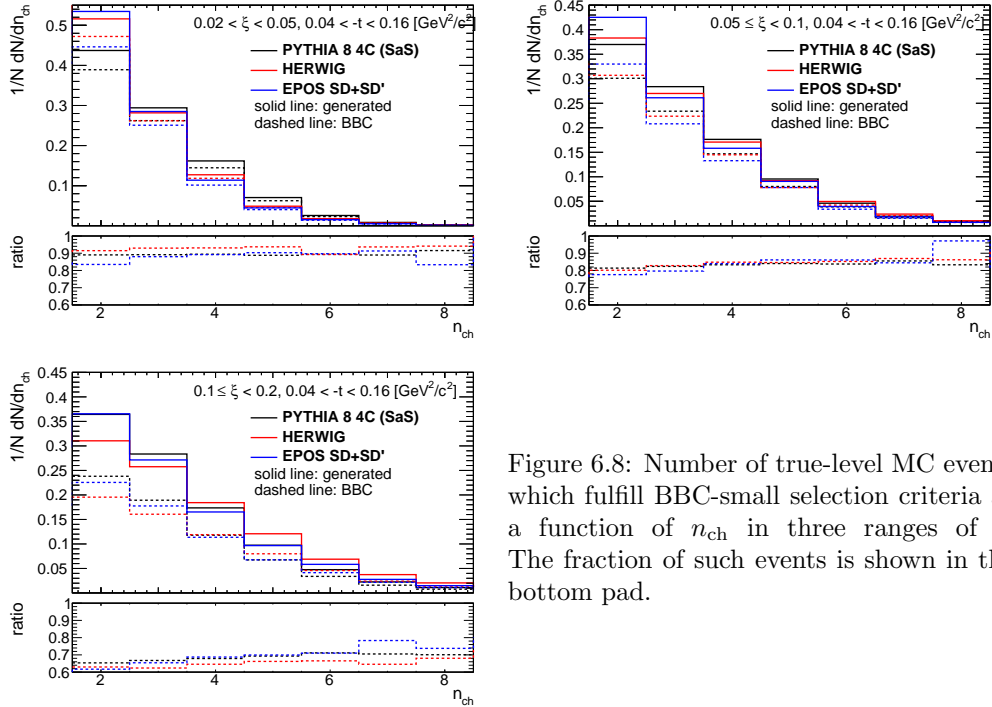


Figure 6.8: Number of true-level MC events which fulfill BBC-small selection criteria as a function of  $n_{\text{ch}}$  in three ranges of  $\xi$ . The fraction of such events is shown in the bottom pad.

559 Data is corrected for BBC-small efficiency using PYTHIA 8 4C (SaS). The uncertainty related  
 560 to this correction is estimated by using HERWIG MC sample, where the hadronisation model is  
 561 different from that used in PYTHIA 8. Figure 6.12 shows the PYTHIA 8 prediction on BBC  
 562 efficiency divided by the HERWIG prediction in three ranges of  $\xi$ . The deviations between these  
 563 two models are of the order of 4% at  $0.02 < \xi < 0.05$ , 2% at  $0.05 < \xi < 0.1$  and about 10%  
 564 at  $0.1 < \xi < 0.2$ . The difference between these two hadronisation models is used as systematic  
 565 uncertainty. For completeness, the differences between PYTHIA 8 and EPOS SD+SD' predictions  
 566 are shown in Fig. 6.13. Most of them are of the order of 3%, except  $n_{\text{ch}} \leq 3$  for which the difference  
 567 varies up to 6%.

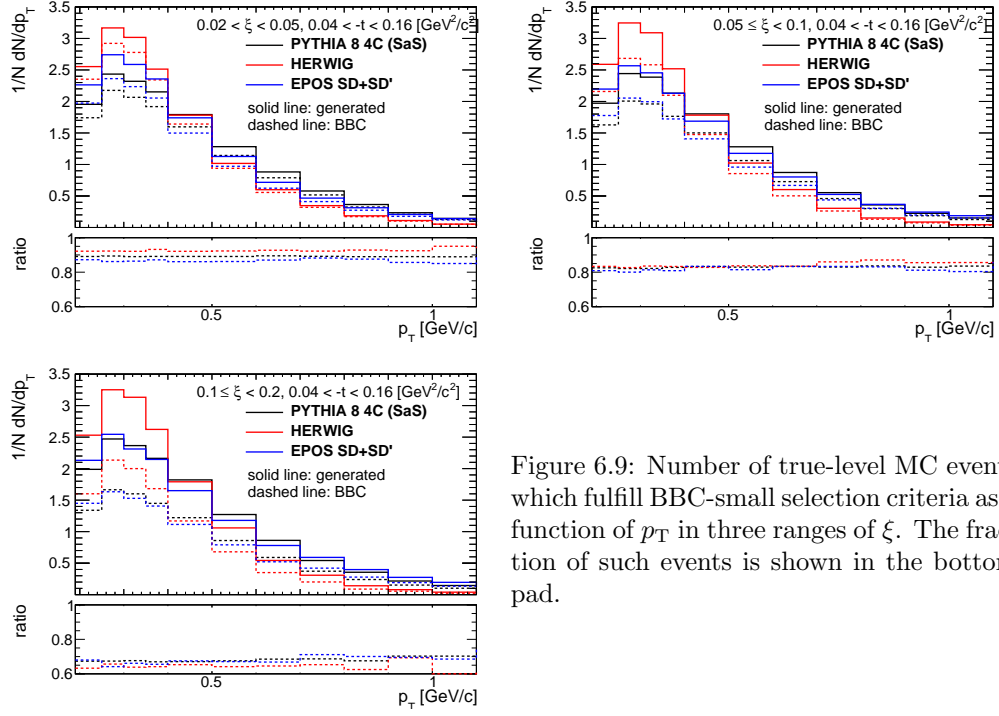


Figure 6.9: Number of true-level MC events which fulfill BBC-small selection criteria as a function of  $p_T$  in three ranges of  $\xi$ . The fraction of such events is shown in the bottom pad.

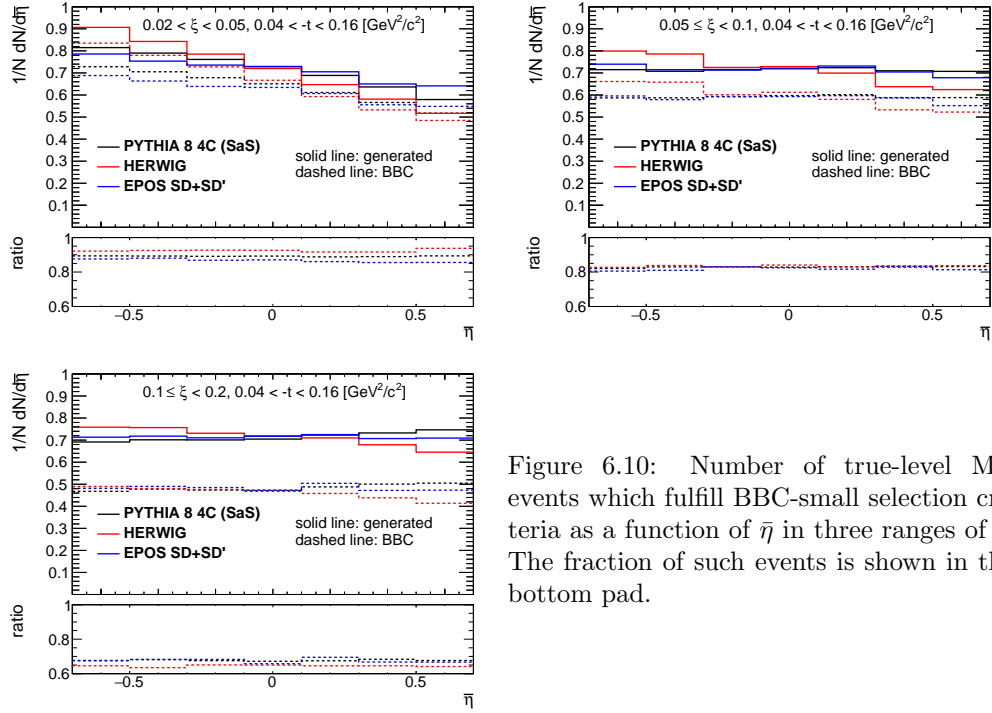


Figure 6.10: Number of true-level MC events which fulfill BBC-small selection criteria as a function of  $\bar{\eta}$  in three ranges of  $\xi$ . The fraction of such events is shown in the bottom pad.

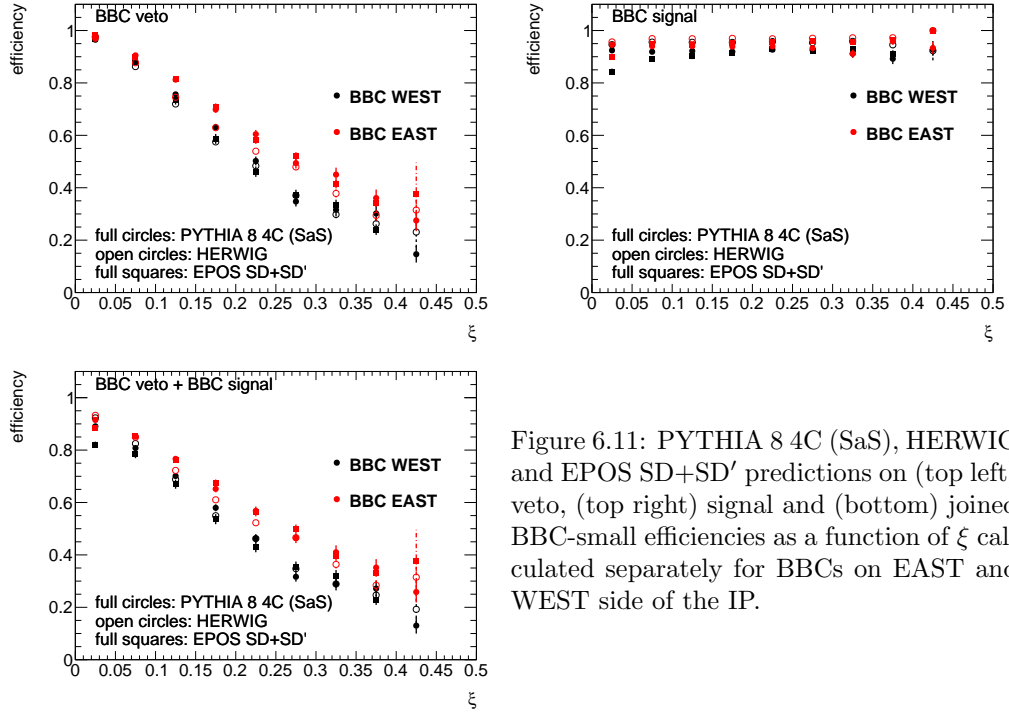


Figure 6.11: PYTHIA 8 4C (SaS), HERWIG and EPOS SD+SD' predictions on (top left) veto, (top right) signal and (bottom) joined BBC-small efficiencies as a function of  $\xi$  calculated separately for BBCs on EAST and WEST side of the IP.

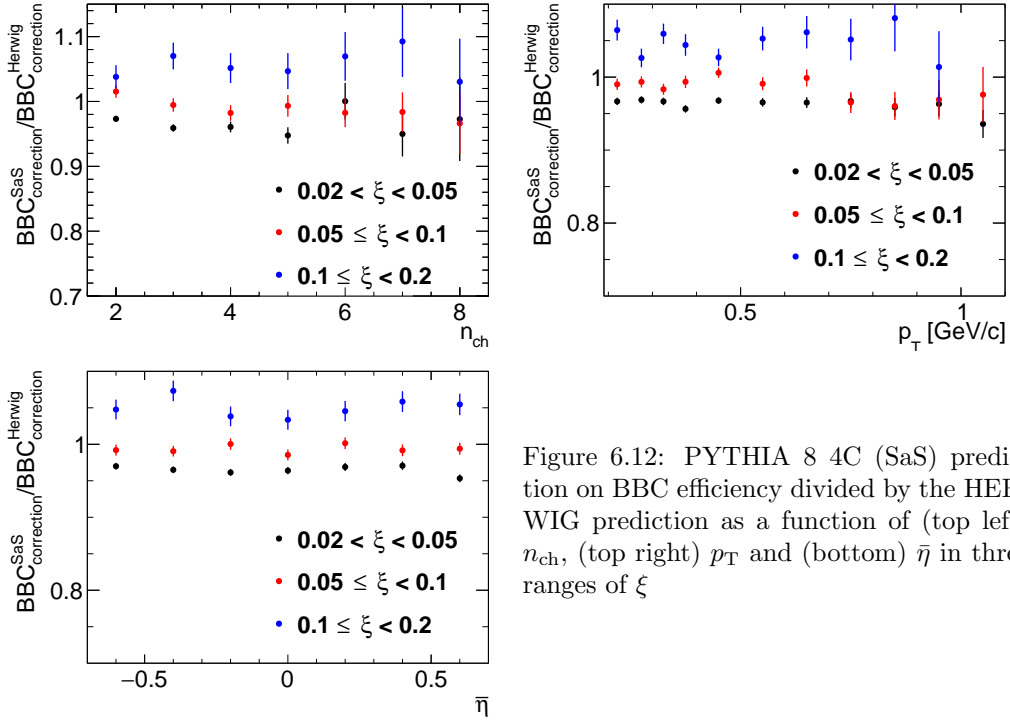


Figure 6.12: PYTHIA 8 4C (SaS) prediction on BBC efficiency divided by the HERWIG prediction as a function of (top left)  $n_{ch}$ , (top right)  $p_T$  and (bottom)  $\bar{\eta}$  in three ranges of  $\xi$

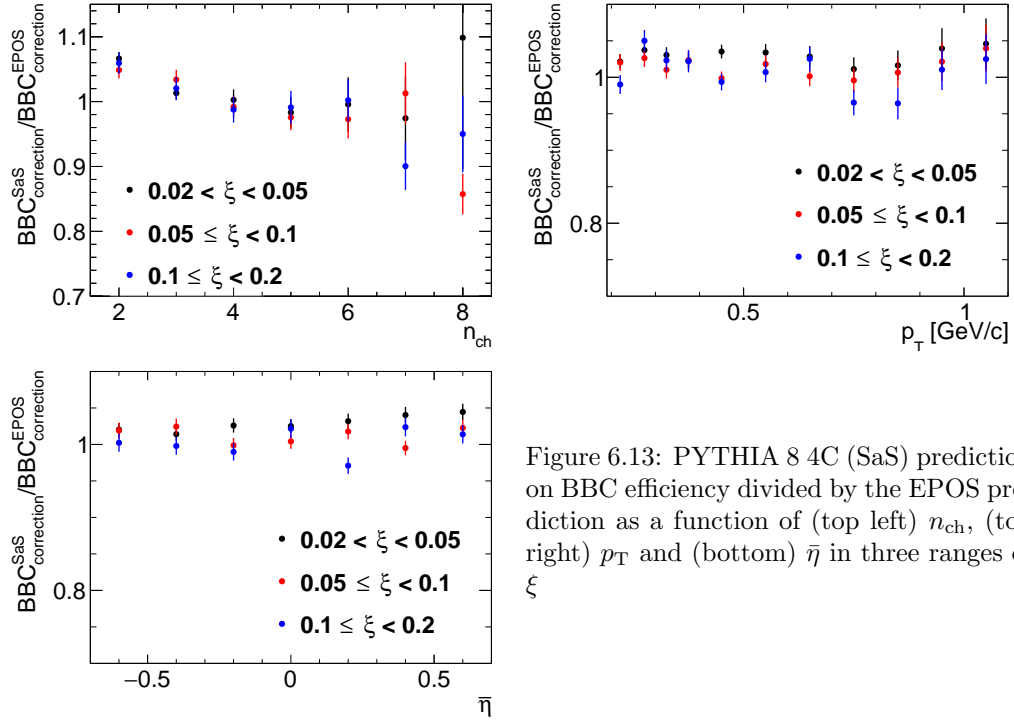


Figure 6.13: PYTHIA 8 4C (SaS) prediction on BBC efficiency divided by the EPOS prediction as a function of (top left)  $n_{\text{ch}}$ , (top right)  $p_{\text{T}}$  and (bottom)  $\eta$  in three ranges of  $\xi$

# 7. Migrations into and out of the Fiducial Region

In this section the corrections due to the migrations of tracks and forward proton into and out of the fiducial region are described.

## 7.1 Migrations of Tracks into and out of the Fiducial Region

The procedure, described in this section, accounts for migrations of tracks into and out of the fiducial region, which originate from TPC resolution effects. The correction factor for such tracks,  $f_{\text{okr}}(p_T, \eta)$  is defined as follows:

$$f_{\text{okr}}(p_T, \eta) = \frac{1 - f_{\text{okr}}^-(p_T, \eta)}{1 - f_{\text{okr}}^+(p_T, \eta)} \quad (7.1)$$

where:

$f_{\text{okr}}^-(p_T, \eta)$  is the fraction of reconstructed tracks for which the corresponding primary particle is outside of the kinematic range of the measurement,

$f_{\text{okr}}^+(p_T, \eta)$  is the fraction of primary particles for which the corresponding reconstructed track is outside of the kinematic range of the measurement.

The resulting residual migrations, shown in Fig. 7.1, were estimated using PYTHIA 8 SD embedding MC. The main effect was observed at  $|\eta| \sim 0.7$ , where about 2–6% reconstructed tracks were associated to primary particle outside the fiducial region. However, above contributions to the correction factor,  $f_{\text{okr}}(p_T, \eta)$ , cancel each other and a resultant factor is about 2% at  $|\eta| \sim 0.7$ .

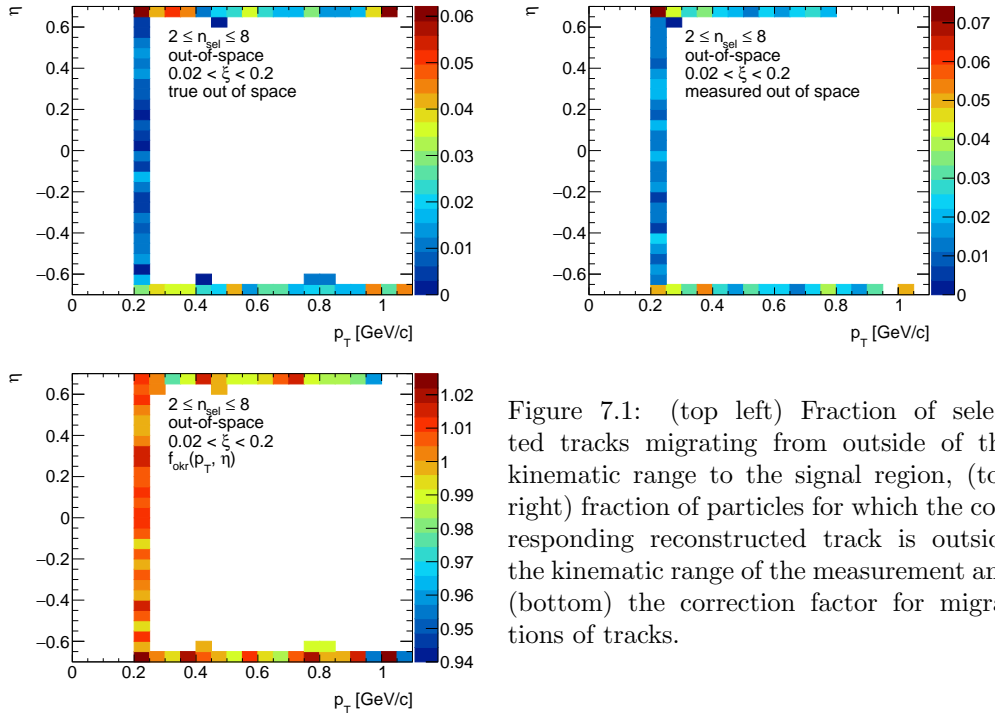


Figure 7.1: (top left) Fraction of selected tracks migrating from outside of the kinematic range to the signal region, (top right) fraction of particles for which the corresponding reconstructed track is outside the kinematic range of the measurement and (bottom) the correction factor for migrations of tracks.

## 7.2 Migrations in $\xi$

The analysis was performed in three ranges of  $\xi$ . Thus, there are migrations into and out of these  $\xi$  regions. They mainly originate from the resolution of  $\xi$  reconstructed from RP tracks. Figure 7.2 shows the resolution of  $\xi$  as a function of the true-level  $\xi$  (denoted as  $\xi_{\text{true}}$ ) with fitted zeroth order polynomial. The resolution of  $\xi$  is fairly constant and equals to about 0.3%.

The corrections due to migrations into and out of  $\xi$  regions was defined as:

$$f_{\xi} = \frac{1 - f_{\xi}^{-}}{1 - f_{\xi}^{+}} \quad (7.2)$$

where:

$f_{\xi}^{-}$  is the fraction of events for which the corresponding true-level  $\xi_{\text{true}}$ , is outside of the  $\xi$  region,

$f_{\xi}^{+}$  is the fraction of events for which the corresponding reconstructed  $\xi_{\text{reco}}$  is outside of the  $\xi$  region.

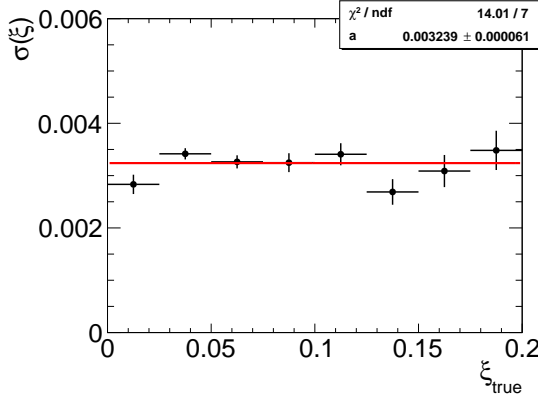


Figure 7.2: The resolution of  $\xi$  as a function of  $\xi_{\text{true}}$ . The zeroth order polynomial, shown as red line, was fitted.

The  $f_{\xi}$  was calculated for each measured variable separately. Figures 7.3 to 7.5 show the fraction of events  $f_{\xi}^{-}$  and  $f_{\xi}^{+}$  as a function of  $n_{\text{ch}}$ ,  $p_{\text{T}}$  and  $\bar{\eta}$ . The lower panel in each figure shows the corresponding correction factor  $f_{\xi}$ . The largest differences between migrations into and out of the  $\xi$  regions were observed at  $0.02 < \xi < 0.05$ , where they are of the order of 2 – 4%. In the other  $\xi$  regions, the difference between  $f_{\xi}^{-}$  and  $f_{\xi}^{+}$  is smaller than 1%.

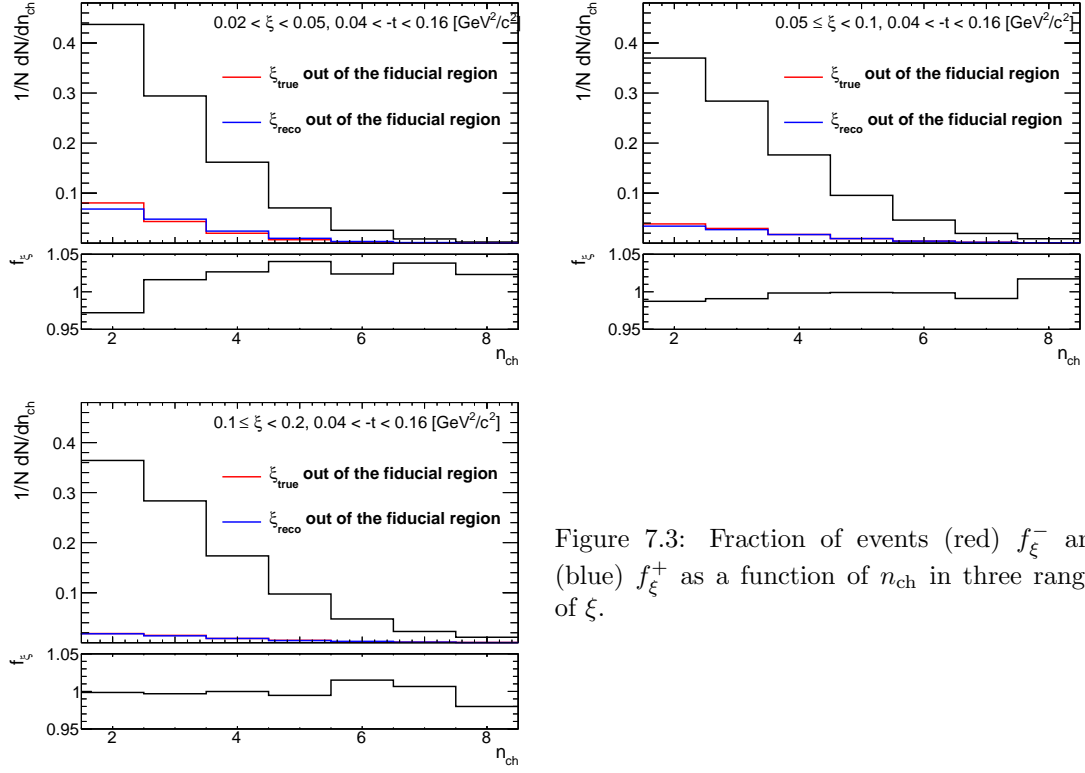


Figure 7.3: Fraction of events (red)  $f_{\xi}^-$  and (blue)  $f_{\xi}^+$  as a function of  $n_{ch}$  in three ranges of  $\xi$ .

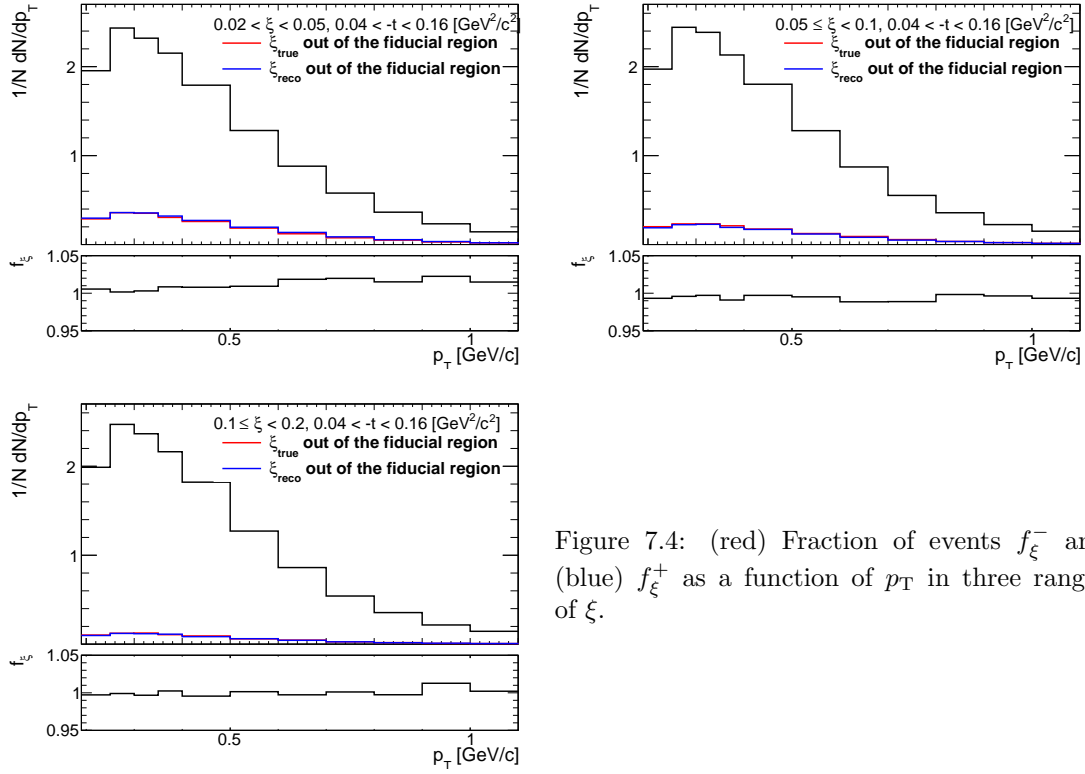


Figure 7.4: (red) Fraction of events  $f_{\xi}^-$  and (blue)  $f_{\xi}^+$  as a function of  $p_T$  in three ranges of  $\xi$ .



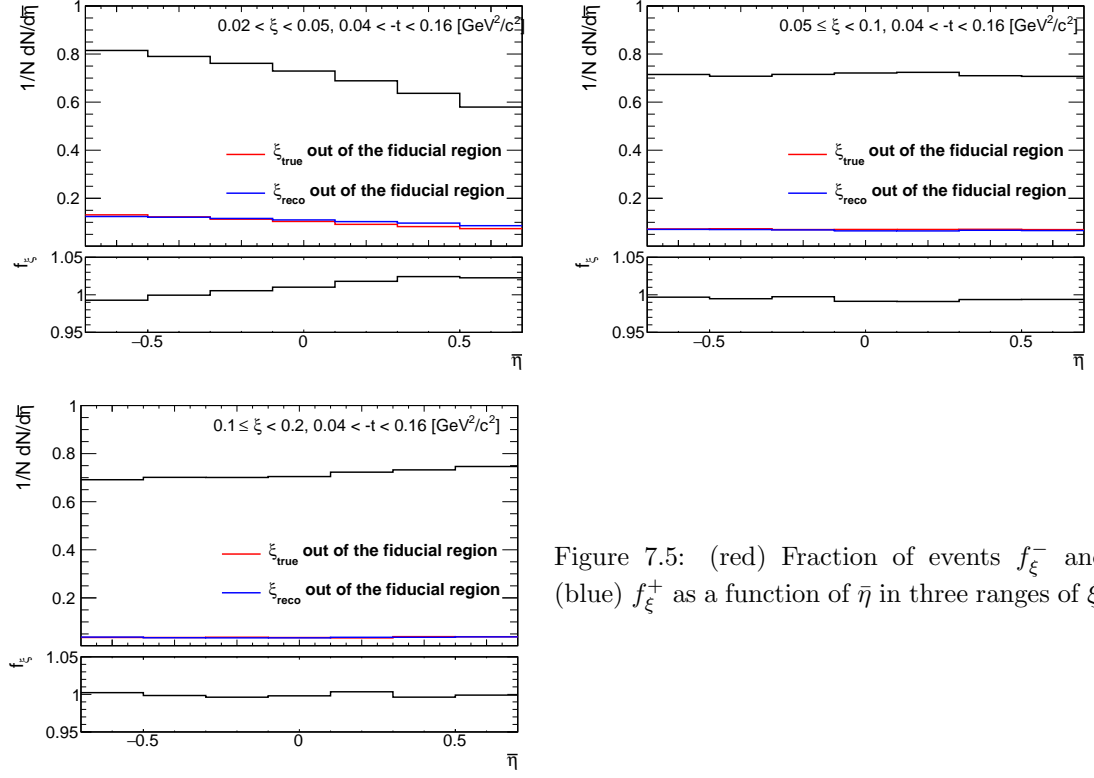


Figure 7.5: (red) Fraction of events  $f_{\xi^-}$  and (blue)  $f_{\xi^+}$  as a function of  $\bar{\eta}$  in three ranges of  $\xi$ .

## 8. Corrections and Unfolding Procedure

After subtraction of accidental, DD, CD and ND backgrounds (as described in Sec. 4.1 and 5), the data was corrected for detector inefficiencies to obtain the distributions of charged particles and particle to antiparticle (pion, kaon, proton and their antiparticle) multiplicity ratios. These corrections include:

- event-by-event weights due to vertex reconstruction efficiency:

$$w_{\text{ev}}^{\text{vrt}}(n_{\text{vrt}}^{\text{global}}, |\Delta z_0|) = \frac{1}{\epsilon_{\text{vrt}}(n_{\text{vrt}}^{\text{global}}, |\Delta z_0|)} \cdot \frac{1}{1 - f_{\text{vrt}}^{\text{veto}}(n_{\text{vrt}}^{\text{global}}, |\Delta z_0|)} \quad (8.1)$$

where the  $|\Delta z_0|$  dependence is only applicable for events with  $n_{\text{vrt}}^{\text{global}} = 2$  as described in Sec. 6.1.

- track-by-track weights due to track reconstruction efficiency, track backgrounds, migrations of tracks into and out of the fiducial region:

$$w_{\text{trk}}(p_T, \eta, V_z) = \frac{1 - f_{\text{bkg}}(p_T, \eta) - f_{\text{fake}}(p_T, \eta)}{\epsilon_{\text{TPC}}(p_T, \eta, V_z) \epsilon_{\text{TOF}}(p_T, \eta, V_z)} f_{\text{okr}}(p_T, \eta) \quad (8.2)$$

where:  $\epsilon_{\text{TPC}}(p_T, \eta, V_z)$  is TPC track reconstruction efficiency [1],  $\epsilon_{\text{TOF}}(p_T, \eta, V_z)$  is TOF matching efficiency [1],  $f_{\text{okr}}(p_T, \eta)$  is a factor accounting for migrations of tracks into and out of the fiducial region,  $f_{\text{bkg}}(p_T, \eta)$  is a fraction of background tracks, and  $f_{\text{fake}}(p_T, \eta)$  is a fraction of fake tracks. These corrections were not applied for  $n_{\text{ch}}$  measurements since they were taken into account in the unfolding procedure.

- event-by-event (for  $n_{\text{ch}}$  distribution) or track-by-track (for  $p_T, \bar{\eta}$  distributions) weights,  $f_{\xi}$ , due to migrations of events between three  $\xi$  regions.

Additionally, the obtained distributions were corrected for BBC-small efficiency,  $\epsilon_{\text{BBC}}$ , using the following weight, which was calculated for each true-level quantity ( $n_{\text{ch}}, p_T, \bar{\eta}$ ) in three ranges of  $\xi$  separately:

$$w_{\text{BBC}} = \frac{1}{\epsilon_{\text{BBC}}} \quad (8.3)$$

In the following sections, the correction procedure for each of the measured distributions is presented separately.

### 8.1 Correction to $dN/dn_{\text{sel}}$

In order to express the multiplicity distribution in terms of the number of charged particles,  $n_{\text{ch}}$ , instead of the number of selected tracks,  $n_{\text{sel}}$ . The following procedure based on the Bayesian unfolding [14, 15] was used. First, the  $n_{\text{sel}}$  distribution was corrected for vertex reconstruction effects by applying event-by-event weights,  $w_{\text{ev}}^{\text{vrt}}(n_{\text{vrt}}^{\text{global}}, |\Delta z_0|)$ . The number of events in which  $n_{\text{ch}}$  are produced,  $N_{\text{ev}}(n_{\text{ch}})$ , can be associated with the number of events in which  $n_{\text{sel}}$  are reconstructed,  $N_{\text{ev}}(n_{\text{sel}})$ . Since there are several possible  $n_{\text{sel}}$  observed in  $n_{\text{ch}}$  event,  $N_{\text{ev}}(n_{\text{ch}})$  is given by:

$$\begin{aligned} N_{\text{ev}}(n_{\text{ch}}) &= \sum_{n_{\text{sel}}=0}^8 P(n_{\text{ch}}|n_{\text{sel}}) \cdot N_{\text{ev}}(n_{\text{sel}}) \\ &= \frac{1}{\epsilon_m(n_{\text{ch}})\epsilon_r(n_{\text{ch}})} \sum_{n_{\text{sel}}=2}^8 P(n_{\text{ch}}|n_{\text{sel}}) \cdot N_{\text{ev}}(n_{\text{sel}}) \end{aligned} \quad (8.4)$$

where:

631  $P(n_{\text{ch}}|n_{\text{sel}})$  is the conditional probability of having  $n_{\text{ch}}$  charged particles in an event in which  
 632  $n_{\text{sel}}$  tracks were found,

633  $\epsilon_m(n_{\text{ch}})$  is a factor, which recovers events that are lost due to TPC track reconstruction and TOF  
 634 matching inefficiencies, i.e. those with  $n_{\text{ch}} \geq 2$  but  $n_{\text{sel}} < 2$ ,

635  $\epsilon_r(n_{\text{ch}})$  is a factor, which recovers events which are lost due to fake tracks, i.e. those with  $n_{\text{ch}} \leq 8$   
 636 but  $n_{\text{sel}} > 8$ . It was checked that this effect is negligible (smaller than 1%) and can be  
 637 omitted.

638 Figure 8.1 shows  $\epsilon_m(n_{\text{ch}})$  in three ranges of  $\xi$ . It was derived from MC and varies from about 25%  
 639 for  $n_{\text{ch}} = 2$  to 95% for  $n_{\text{ch}} = 8$ . Since there are additional data-driven corrections to TPC and TOF  
 640 efficiencies, MC simulations were modified by randomly removing or adding tracks. This was done  
 641 in accordance with differences in the efficiencies between data and MC. Figure 8.2 shows  $\epsilon_m(n_{\text{ch}})$   
 642 calculated in three ranges of  $\xi$  using no-pile-up PYTHIA 8 and EPOS SD+SD'. The differences  
 643 between these two models, which are up to 8% for  $n_{\text{ch}} = 2$  and  $0.1 < \xi < 0.2$ , were symmetrized  
 644 and taken as a systematic uncertainty.

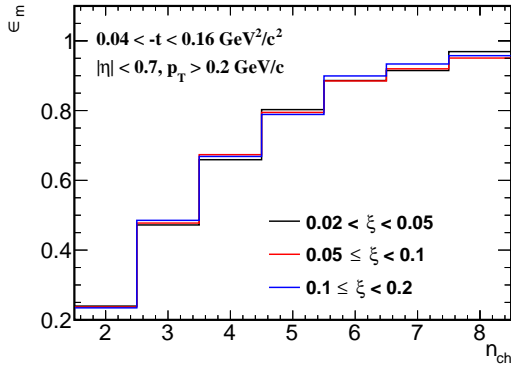


Figure 8.1:  $\epsilon_m(n_{\text{ch}})$  calculated separately in three ranges of  $\xi$  using PYTHIA 8 embedding MC.

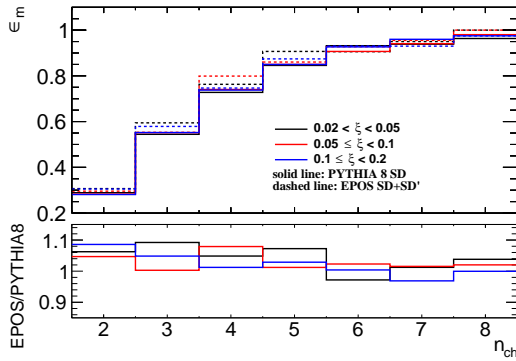


Figure 8.2: Comparison of  $\epsilon_m(n_{\text{ch}})$  calculated separately in three ranges of  $\xi$  using PYTHIA 8 SD and EPOS SD+SD' no-pile-up MCs.

645 The probability  $P(n_{\text{ch}}|n_{\text{sel}})$  can be derived using Bayes' theorem, which can be stated mathematically in terms of charged particle and charged track multiplicities as:  
 646

$$P(n_{\text{ch}}) \cdot P(n_{\text{sel}}|n_{\text{ch}}) = P(n_{\text{ch}}|n_{\text{sel}}) \cdot P(n_{\text{sel}}) \quad (8.5)$$

647 where:  $P(n_{\text{sel}})$  and  $P(n_{\text{ch}})$  are probabilities of observing  $n_{\text{sel}}$  and  $n_{\text{ch}}$  respectively,  $P(n_{\text{ch}}|n_{\text{sel}})$   
 648 and  $P(n_{\text{sel}}|n_{\text{ch}})$  are conditional probabilities.

649 In order to improve the estimate of  $P(n_{\text{ch}}|n_{\text{sel}})$ , the unfolding is done iteratively:

- In the first iteration, it is assumed that:

$$P(n_{\text{ch}}|n_{\text{sel}}) = P = P^{\text{MC}}(n_{\text{sel}}|n_{\text{ch}}) \frac{P^{\text{MC}}(n_{\text{ch}})}{P^{\text{MC}}(n_{\text{sel}})} \quad (8.6)$$

$$N_{\text{ev}}(n_{\text{ch}}) = \frac{1}{\epsilon_m(n_{\text{ch}})} \sum_{n_{\text{sel}}=2}^8 N_{\text{ev}}(n_{\text{sel}}) \cdot P \quad (8.7)$$

where  $P^{\text{MC}}(n_{\text{sel}}|n_{\text{ch}})$ ,  $P^{\text{MC}}(n_{\text{ch}})$  and  $P^{\text{MC}}(n_{\text{sel}})$  are obtained from MC.  $P^{\text{MC}}(n_{\text{sel}}|n_{\text{ch}})$  is the same for each iteration.

- In the  $(i + 1)$ th iteration we have:

$$P^{i+1} = P^{\text{MC}}(n_{\text{sel}}|n_{\text{ch}}) \frac{N_{\text{ev}}^i(n_{\text{ch}})}{N_{\text{ev}}(n_{\text{sel}})} \quad (8.8)$$

$$N_{\text{ev}}^{i+1}(n_{\text{ch}}) = \frac{1}{\epsilon_m(n_{\text{ch}})} \sum_{n_{\text{sel}}=2}^8 N_{\text{ev}}(n_{\text{sel}}) \cdot P^{i+1} \quad (8.9)$$

where  $N_{\text{ev}}^i(n_{\text{ch}})$  is calculated in the previous iteration, and  $N_{\text{ev}}(n_{\text{sel}})$  is taken from data.

The unfolding matrices  $P(n_{\text{ch}}|n_{\text{sel}})$  for each  $\xi$  region, shown in Fig. 8.3, were obtained from PYTHIA 8 embedding MC and used in all iterations of the above procedure. Similarly to  $\epsilon_m(n_{\text{ch}})$ , the matrices were modified in order to take into account differences between data and PYTHIA 8. In order to increase statistical precision of the unfolding matrices, all simulated events were used, i.e. also those with additional fake vertices (with  $n_{\text{sel}}$  defined as a number of primary tracks associated with the best vertex). The systematic uncertainty related to limited statistics in PYTHIA 8 was estimated by performing 50 pseudo-experiments, in which the unfolding matrices were smeared according to their statistical uncertainties. It affects mainly large charged-particle multiplicities, where it is about 8 – 10% (as shown in Fig. 8.4), and is smaller or at the same level as other components contributing to the total systematic uncertainty.

The distribution  $dN/dn_{\text{ch}}$  obtained after the unfolding procedure was corrected for BBC-small efficiency, through  $w_{\text{BBC}}(n_{\text{ch}})$  weights, and migrations of events between  $\xi$  ranges, through  $f_{\xi}(n_{\text{ch}})$  weights. Since the unfolding matrices contain track reconstruction efficiencies, non-primary track backgrounds, migrations of tracks into and out of the fiducial region, the weight  $w_{\text{trk}}(p_{\text{T}}, \eta, V_z)$  was not used.

Finally, the  $dN/dn_{\text{ch}}$  distribution was normalized to the total number of events,  $N_{\text{ev}} = N$ , which was calculated as the integral of the unfolded distribution.

## 8.2 Correction to Transverse Momentum and Pseudorapidity Distributions

First the accidental and non-SD backgrounds were subtracted from the  $p_{\text{T}}$  and  $\bar{\eta}$  distributions. Next, each event was corrected for vertex reconstruction efficiency by applying  $w_{\text{ev}}^{\text{vrt}}(n_{\text{vrt}}^{\text{global}}, |\Delta z_0|)$  weights. Then, the tracks were corrected for the track reconstruction efficiency, non-primary track background contribution, track and  $\xi$  migrations, BBC-small efficiency (the product of  $w_{\text{trk}}(p_{\text{T}}, \eta, V_z)$ ,  $f_{\xi}$  and  $w_{\text{BBC}}$  weights was applied,  $f_{\xi}$  and  $w_{\text{BBC}}$  were calculated as a function of true-level  $p_{\text{T}}$  and  $\bar{\eta}$  separately).

In order to obtain charged-particle densities, the  $p_{\text{T}}$  and  $\bar{\eta}$  distributions were normalized to unity and scaled by the average charged particle multiplicity in an event  $\langle n_{\text{ch}} \rangle$ . The latter was calculated from the corrected charged particle multiplicity distribution  $dN/dn_{\text{ch}}$  (Sec. 8.1).

The mean particle densities in an event,  $\langle p_{\text{T}} \rangle$  and  $\langle \bar{\eta} \rangle$ , were obtained from the measured distributions.

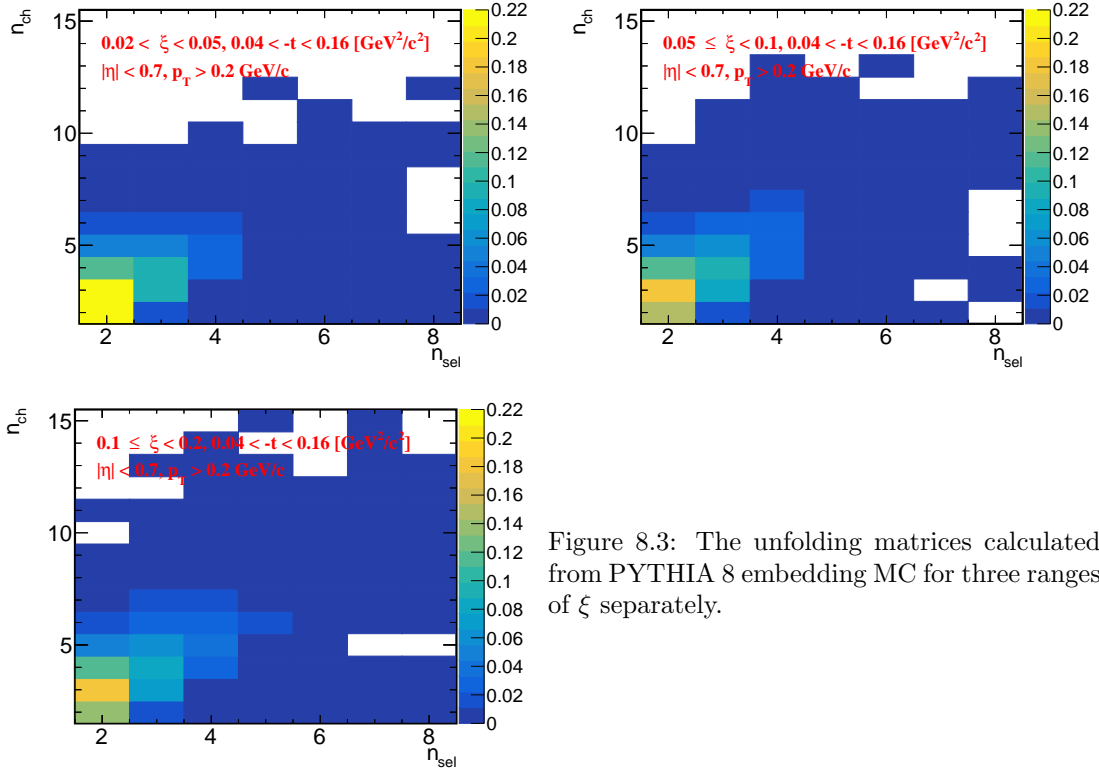


Figure 8.3: The unfolding matrices calculated from PYTHIA 8 embedding MC for three ranges of  $\xi$  separately.

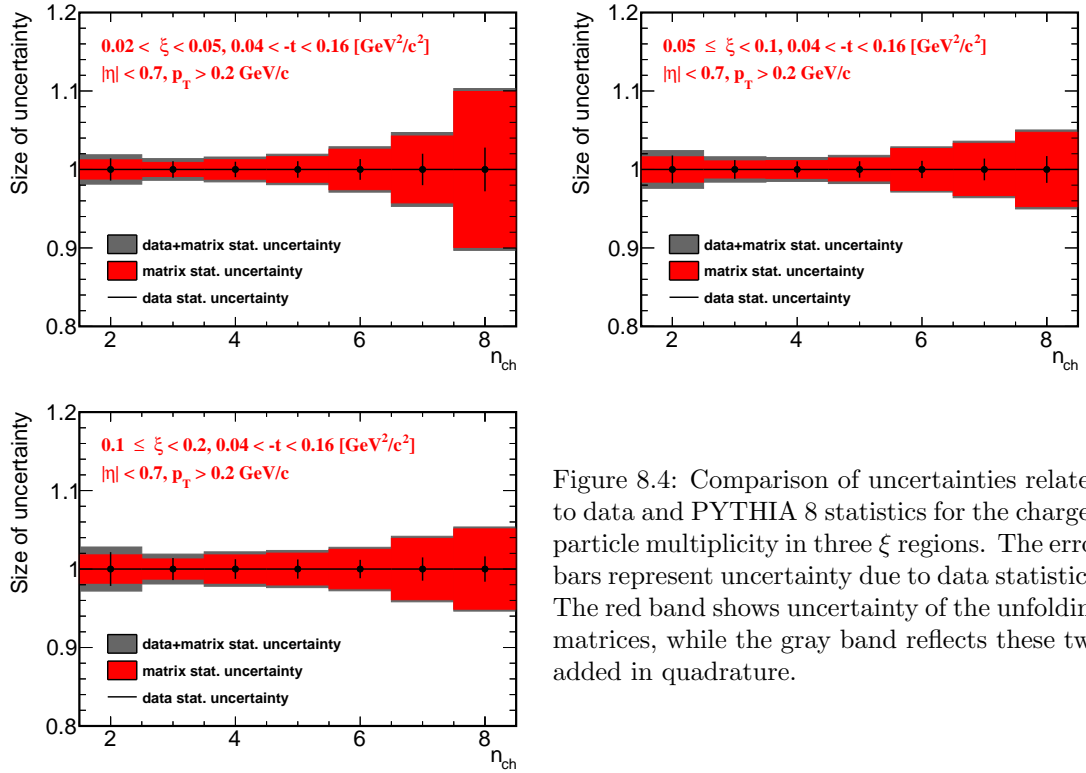


Figure 8.4: Comparison of uncertainties related to data and PYTHIA 8 statistics for the charged particle multiplicity in three  $\xi$  regions. The error bars represent uncertainty due to data statistics. The red band shows uncertainty of the unfolding matrices, while the gray band reflects these two added in quadrature.

### 8.3 Closure Tests

In order to validate the correction procedures, closure tests were performed, i.e. full correction procedure was applied to the MC detector-level distributions and the results were directly compared to the true-level distributions. Figure 8.5 shows closure tests of multiplicity, transverse momentum and pseudorapidity distributions for three ranges of  $\xi$ , separately. PYTHIA 8 SD embedding MC was used as an input. In order to compare corrected and true-level distributions, the statistical uncertainties of the true-level distributions were assumed to be 0. The difference between true-level and corrected distributions was taken as a systematic uncertainties.

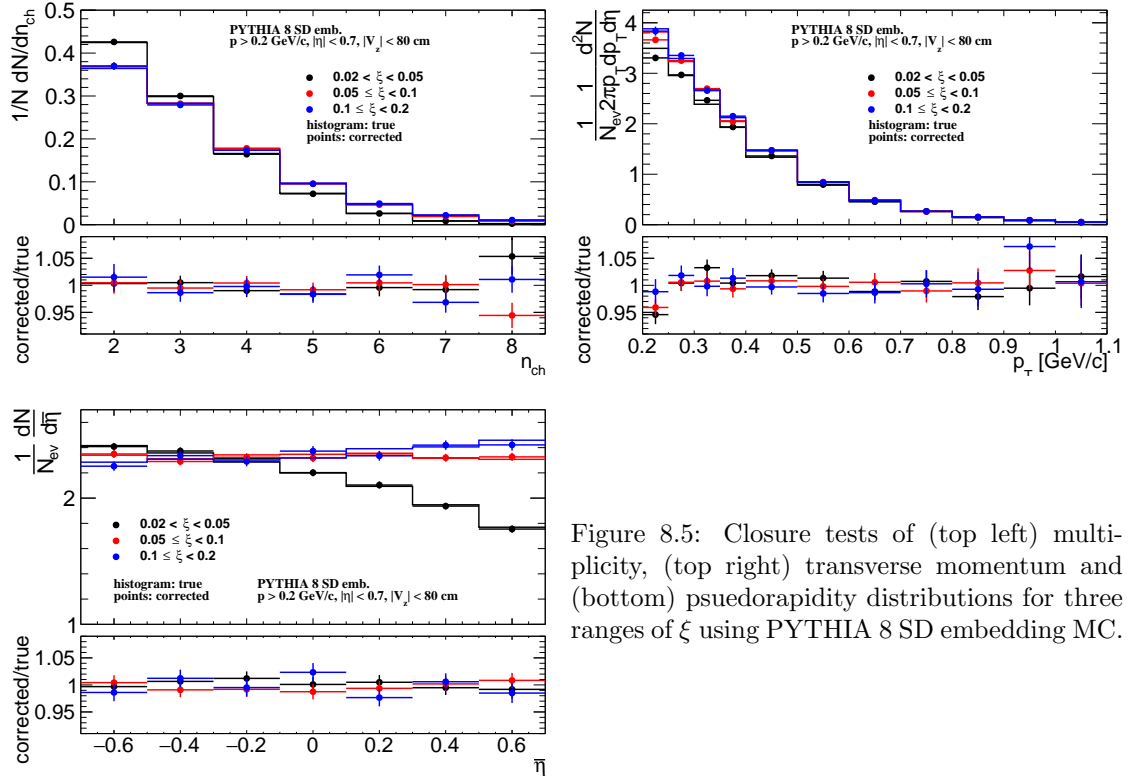


Figure 8.5: Closure tests of (top left) multiplicity, (top right) transverse momentum and (bottom) pseudorapidity distributions for three ranges of  $\xi$  using PYTHIA 8 SD embedding MC.

### 8.4 EAST-WEST asymmetry

Another kind of consistency checks can be performed by comparing the results obtained by tagging forward protons in different detectors. Therefore, each distribution was measured separately for events in which forward proton is on one and the other side of the IP (east-west). Figure 8.6 shows the tests of multiplicity, transverse momentum and pseudorapidity distributions for three ranges of  $\xi$ , separately. The largest difference is observed for charged-particle multiplicity distributions, where it varies up to 20% for  $n_{ch} = 8$  and  $0.02 < \xi < 0.1$ . For the rest multiplicities and  $\xi$  ranges, the differences are smaller ( $< 10\%$ ). In case of  $p_T$  and  $\bar{\eta}$  distributions, a level of these disagreements is below 5%. As a result, half of the differences between east and west distributions were used to be systematic uncertainty.

### 8.5 Particle Identification

The specific ionization energy loss, the  $dE/dx$ , is a function of magnitude of the particle momentum. In this section the particle identification by the  $dE/dx$  is described. Due to the low

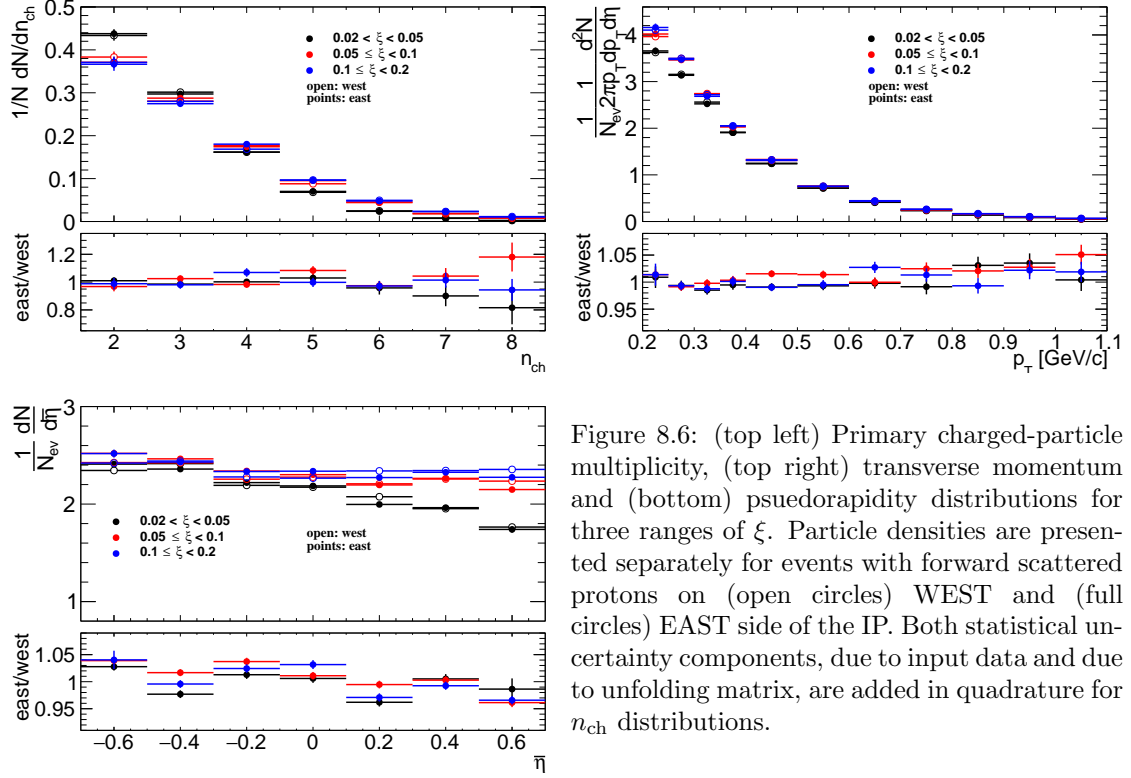


Figure 8.6: (top left) Primary charged-particle multiplicity, (top right) transverse momentum and (bottom) pseudorapidity distributions for three ranges of  $\xi$ . Particle densities are presented separately for events with forward scattered protons on (open circles) WEST and (full circles) EAST side of the IP. Both statistical uncertainty components, due to input data and due to unfolding matrix, are added in quadrature for  $n_{ch}$  distributions.

particle multiplicity and lack of signal in VPDs on the outgoing proton side (presence of the rapidity gap) in SD events, the time of collision is not defined precisely enough, therefore, the particle identification by the TOF is not possible and the analysis was limited to identification only by  $dE/dx$ .

The ionization energy loss of charged particles in material is given by the Bethe-Bloch formula and for the STAR TPC by the more precise Bichsel formula [16]. The particle type can be determined by comparison of particle's  $dE/dx$  with the Bethe-Bloch (Bichsel) expectations. Figure 8.7 shows the  $dE/dx$  versus rigidity  $q \times p$  for particles in  $|\eta| < 0.7$ . Particles are well separated at low  $|q \times p|$ , whereas at higher  $|q \times p|$  the  $dE/dx$  of different particle species starts to overlap:  $e^\pm$  and  $K^\pm$  merge at  $\sim 0.4$  GeV/c,  $K^\pm$  and  $\pi^\pm$  merge at  $\sim 0.65$  GeV/c, and  $p(\bar{p})$  and  $\pi^\pm$  merge at  $\sim 1$  GeV/c. Since the  $dE/dx$  distribution for a given particle type is not Gaussian, the following variable for each particle type was defined:

$$n\sigma_{dE/dx}^i = \ln \left( \frac{dE/dx}{(dE/dx)_i^{BB}} \right) / \sigma \quad (8.10)$$

where  $(dE/dx)_i^{BB}$  is the Bethe-Bloch (Bichsel) expectation of  $dE/dx$  for the given particle type  $i$  ( $i = \pi, K, p$ ),  $\sigma$  - the  $dE/dx$  resolution. The expected value of  $n\sigma_{dE/dx}^i$  for the particle under consideration is 0 and the width equals to 1. The sample  $n\sigma_{dE/dx}^i$  distribution for  $\pi^\pm$ ,  $K^\pm$  and  $p(\bar{p})$  in one  $\xi$  range,  $0.02 < \xi < 0.05$ , is shown in Fig. 8.8.

Figure 8.9 shows the  $n\sigma_{dE/dx}^{\pi^\pm}$ ,  $n\sigma_{dE/dx}^{K^\pm}$  and  $n\sigma_{dE/dx}^{p(\bar{p})}$  distributions for  $0.6 < p_T < 0.65$  GeV/c in the  $\xi$  range,  $0.02 < \xi < 0.05$ , each corrected for the energy loss (mass of  $i$ -particle was assumed) [1] and vertexing (other  $p_T$  bins are shown in Appendix B). To extract the particle yield for a given particle type, a multi-Gaussian fit is applied to the  $n\sigma_{dE/dx}^i$  distribution in each  $p_T$  bin and  $\xi$  range. The parameters of the multi-Gaussian fit are the centroids  $\mu_{i^-/i^+}$ , widths  $\sigma_{i^-/i^+}$ , sum and ratios of yields  $C_{i^-/i^+}$ ,  $r_{i^-/i^+}$  for negative  $i^-$  and positive  $i^+$  particles ( $\pi^\pm$ ,  $e^\pm$ ,  $K^\pm$ ,  $p$  and  $\bar{p}$ ). The positive and negative particle  $n\sigma_{dE/dx}^i$ -distributions are fitted simultaneously, where the centroids and

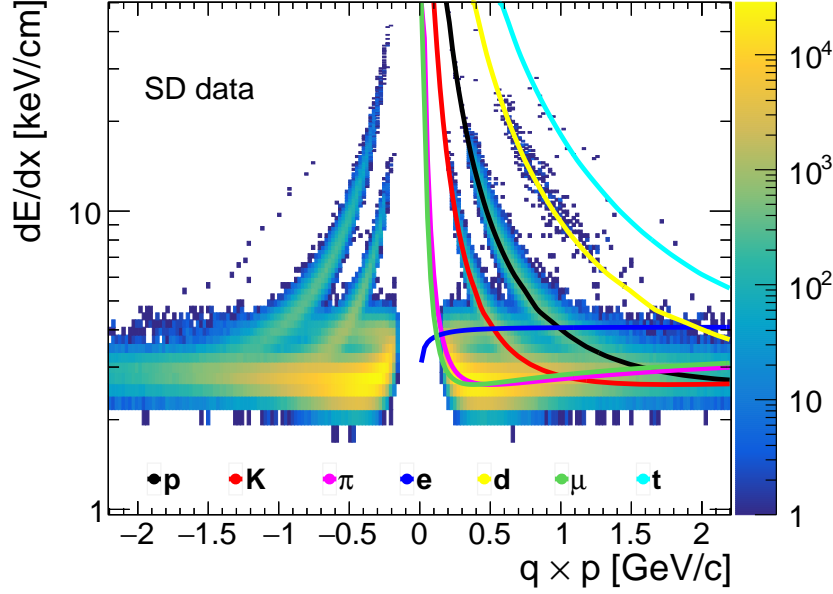


Figure 8.7: Specific ionization energy loss  $dE/dx$  as a function of rigidity  $q \times p$  for particles in  $|\eta| < 0.7$ . The Bichsel predictions for each particle species are also shown.

widths are kept the same for particle and antiparticle. In some  $p_T$  regions, the fit does not converge, because different particle species are not well separated there. Therefore, multiple steps of fitting are performed to reduce the number of free parameters in the final fit and ensure its stability. Almost all centroids and widths are constrained by a function with free parameters  $p_k$ , where  $k \in \mathbb{N}$ . The function is chosen to describe the data as best as possible. Since  $dE/dx$  is a function of the particle momentum and its shape should be independent of the process under study, the values of  $p_k$  are obtained only for events with  $0.02 < \xi < 0.05$  and kept the same for other  $\xi$  ranges. The electron contributions are fixed, but separately for each  $\xi$  range. The procedure slightly differs for different particle types. In each step, the multi-Gaussian fit is performed first, then the widths and centroids are fitted in  $p_T$  ranges in which the fit applied to  $n\sigma_{dE/dx}^i$  converges. Later, the widths and centroids are extrapolated to other  $p_T$  ranges, in which particle species are not well separated:

1.  $\pi^\pm$ :

- Step 1 (Fig. 8.10):

- Analyze data with  $0.2 < p_T < 0.65$  GeV/c
- Fit  $\mu_{\pi^-/\pi^+}$  and  $\sigma_{\pi^-/\pi^+}$  as a function of  $p_T$  with a polynomial  $p_0 p_T^3 + p_1 p_T^2 + p_2 p_T + p_3$
- Fit  $r_{e^-/e^+}$  as a function of  $p_T$  with a polynomial  $p_0 p_T^2 + p_1 p_T + p_2$
- Fit  $C_{e^-/e^+}$ ,  $\mu_{K^-/K^+}$  as a functions of  $p_T$  with  $p_0 \exp(p_1 p_T) + p_2$
- Fit  $\mu_{e^-/e^+}$  as a function of  $p_T$  with  $p_0 \exp[-(p_1 p_T)^{p_2}]$
- Fit  $\sigma_{K^-/K^+}$  as a function of  $p_T$ , for  $0.3 < p_T < 0.5$  GeV/c, with constant  $p_0$
- Fit  $\mu_{\bar{p}/p}$  and  $\sigma_{\bar{p}/p}$  as a function of  $p_T$  with  $p_0 \exp(p_1 p_T)$

- Step 2:

- $\sigma_{e^-/e^+}$  fixed to 1.2 and 0.8 for  $0.2 < p_T < 0.4$  and  $0.4 < p_T < 0.7$ , respectively
- Fit  $\sigma_{K^-/K^+}$  as a function of  $p_T$ , for  $0.3 < p_T < 0.7$  GeV/c, with constant  $p_0$  and fix it to the value of  $p_0$



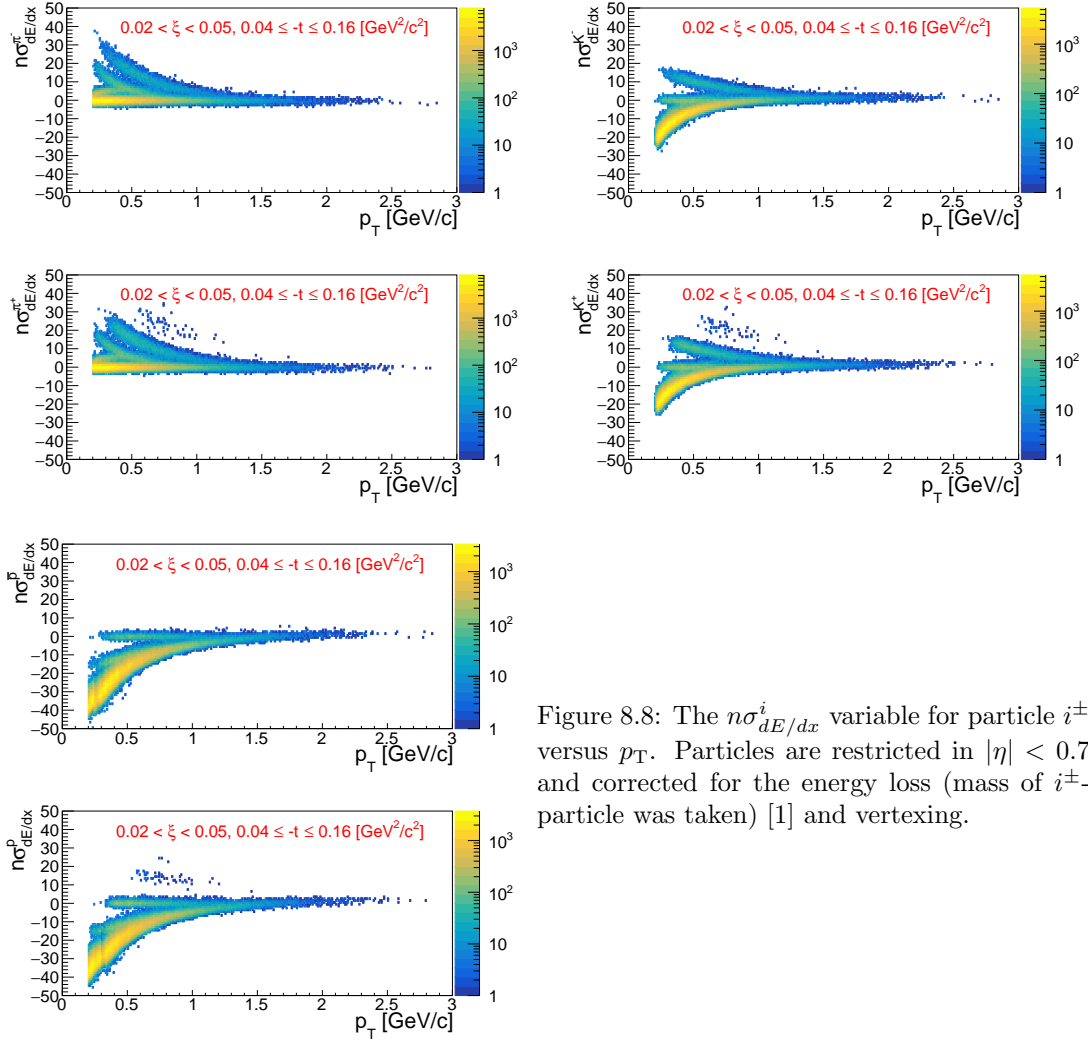


Figure 8.8: The  $n\sigma_{dE/dx}^i$  variable for particle  $i^\pm$  versus  $p_T$ . Particles are restricted in  $|\eta| < 0.7$  and corrected for the energy loss (mass of  $i^\pm$ -particle was taken) [1] and vertexing.

- The rest parameters from Step 1 are fixed to the values calculated from functions obtained in Step 1:  $\mu_{\pi^-/\pi^+}$ ,  $\sigma_{\pi^-/\pi^+}$ ,  $r_{e^-/e^+}$ ,  $C_{e^-/e^+}$ ,  $\mu_{e^-/e^+}$ ,  $\mu_{K^-/K^+}$ ,  $\mu_{\bar{p}/p}$ ,  $\sigma_{\bar{p}/p}$

## 2. $K^\pm$ :

- Step 1 (Fig. 8.11):
  - Analyze data with  $0.2 < p_T < 0.6$  GeV/c
  - Fit  $\mu_{\pi^-/\pi^+}$  as a function of  $p_T$  with  $-\exp(p_0 + p_1 p_T)$
  - Fit  $\sigma_{\pi^-/\pi^+}$ ,  $C_{e^-/e^+}$ ,  $\sigma_{e^-/e^+}$ ,  $\sigma_{K^-/K^+}$  as a function of  $p_T$  with  $\exp(p_0 + p_1 p_T)$
  - Fit  $r_{e^-/e^+}$  as a function of  $p_T$  with constant  $p_0$
  - Fit  $\mu_{e^-/e^+}$  as a function of  $p_T$  with a polynomial  $p_0 p_T^3 + p_1 p_T^2 + p_2 p_T + p_3$
  - Fit  $\mu_{K^-/K^+}$  as a function of  $p_T$  with a polynomial  $p_0 + p_1 p_T^2$
- Step 2:
  - All parameters from Step 1 except  $\sigma_{e^-/e^+}$  are fixed to the values calculated from functions obtained in Step 1
  - Fit  $\sigma_{e^-/e^+}$  as a function of  $p_T$ , for  $0.45 < p_T < 0.65$  GeV/c, with constant  $p_0$

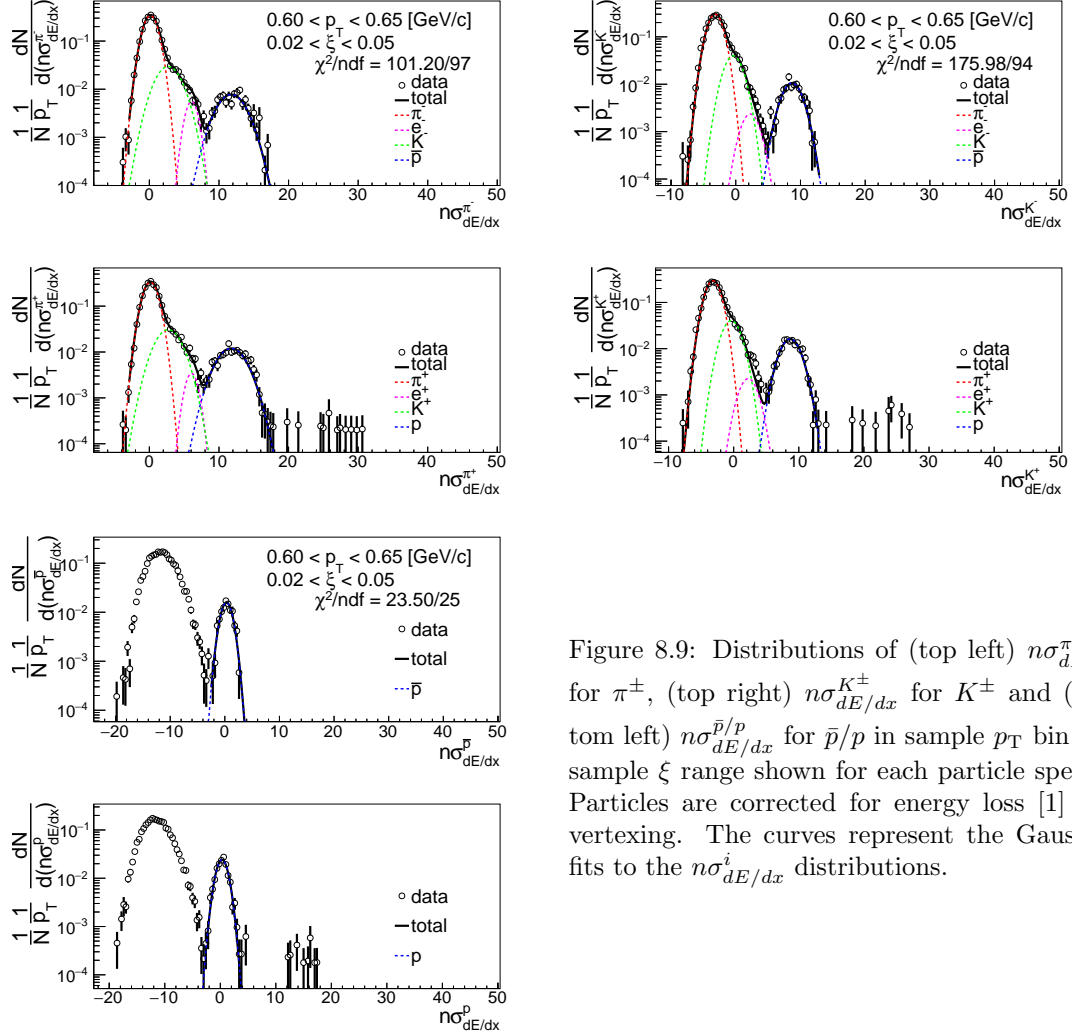


Figure 8.9: Distributions of (top left)  $n\sigma_{dE/dx}^{\pi^\pm}$  for  $\pi^\pm$ , (top right)  $n\sigma_{dE/dx}^{K^\pm}$  for  $K^\pm$  and (bottom left)  $n\sigma_{dE/dx}^{\bar{p}/p}$  for  $\bar{p}/p$  in sample  $p_T$  bin and sample  $\xi$  range shown for each particle species. Particles are corrected for energy loss [1] and vertexing. The curves represent the Gaussian fits to the  $n\sigma_{dE/dx}^i$  distributions.

• Step 3:

- $\sigma_{e^-/e^+}$  fixed to the values calculated from functions obtained in Steps 1 and 2 for  $0.3 < p_T < 0.45$  and  $0.45 < p_T < 0.65$ , respectively.
- The rest parameters from Step 1 are fixed to the values calculated from functions obtained in Step 1:  $\mu_{\pi^-/\pi^+}$ ,  $\sigma_{\pi^-/\pi^+}$ ,  $r_{e^-/e^+}$ ,  $C_{e^-/e^+}$ ,  $\mu_{e^-/e^+}$ ,  $\mu_{K^-/K^+}$ ,  $\sigma_{K^-/K^+}$

3.  $\bar{p}, p$ :

• Step 1 (Fig. 8.12):

- Analyze data with  $0.4 < p_T < 0.9$  GeV/c
- Fit  $\mu_{\pi^-/\pi^+}$ ,  $\mu_{K^-/K^+}$  as a function of  $p_T$  with a polynomial  $p_0 p_T + p_1$
- Fit  $\sigma_{\pi^-/\pi^+}$  as a function of  $p_T$  with a polynomial  $p_0 p_T^2 + p_1 p_T + p_2$
- Fit  $\sigma_{K^-/K^+}$  as a function of  $p_T$  with  $\exp(p_0 + p_1 p_T)$

• Step 2:

- $\mu_{K^-/K^+}$  fixed to the values calculated from a function obtained in Step 1
- All the rest parameters from Step 1 are limited to the values calculated from functions obtained in Step 1

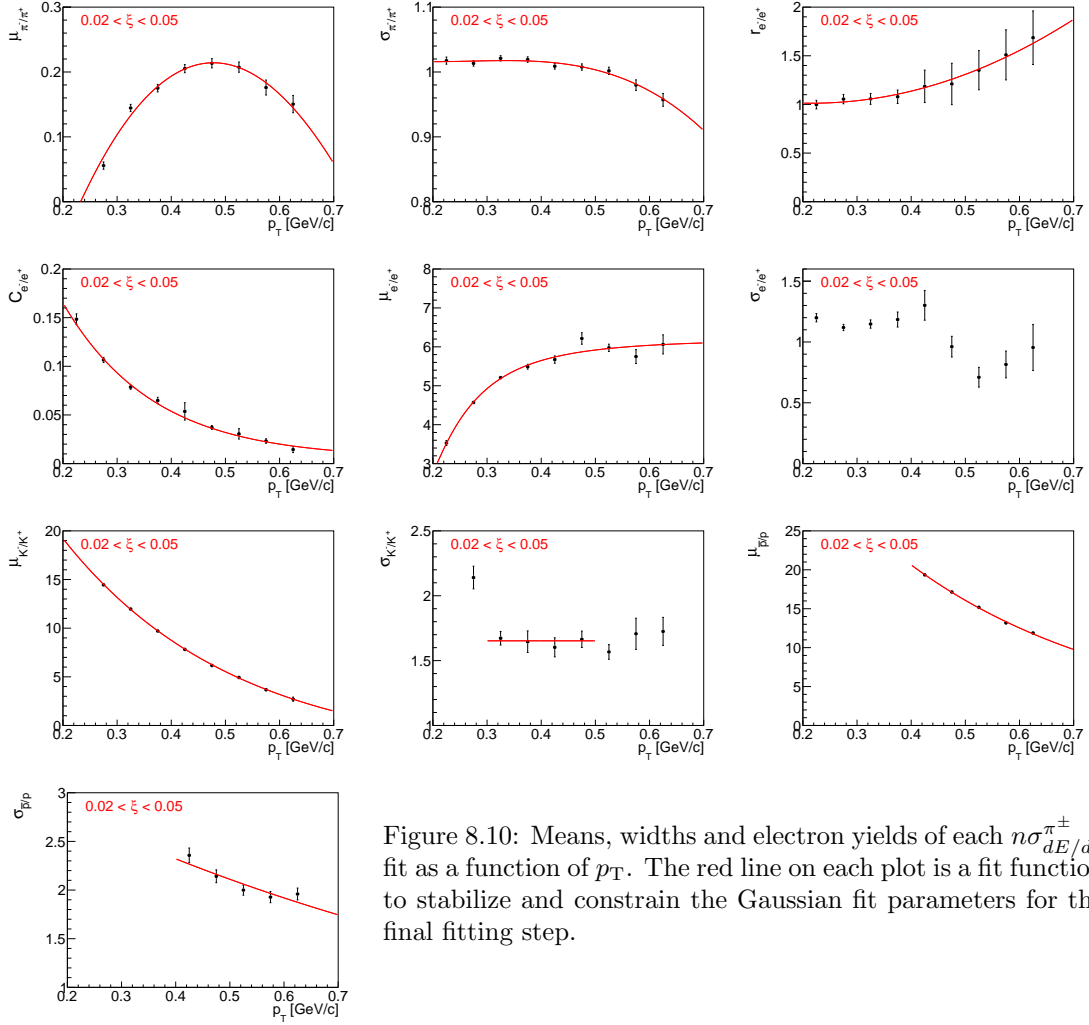


Figure 8.10: Means, widths and electron yields of each  $n\sigma_{dE/dx}^{\pi^{\pm}}$  fit as a function of  $p_T$ . The red line on each plot is a fit function to stabilize and constrain the Gaussian fit parameters for the final fitting step.

- 787 – Fit  $\mu_{\pi^-/\pi^+}$ ,  $\sigma_{\pi^-/\pi^+}$ ,  $\sigma_{K^-/K^+}$  as a function of  $p_T$  with a polynomial  $p_0 p_T^2 + p_1 p_T + p_2$
- 788 – Fit  $\mu_{\bar{p}/p}$  as a function of  $p_T$ , for  $0.7 < p_T < 1.0$  GeV/c, with constant  $p_0$
- 789 • Step 3:
- 790 –  $\mu_{K^-/K^+}$  fixed to the values calculated from a function obtained in Step 1
- 791 –  $\mu_{\bar{p}/p}$  fixed to the values calculated from a function obtained in Step 2 for  $0.7 < p_T < 1.0$
- 792 – The rest parameters from Step 2 are fixed to the values calculated from functions
- 793 obtained in Step 2:  $\mu_{\pi^-/\pi^+}$ ,  $\sigma_{\pi^-/\pi^+}$ ,  $\sigma_{K^-/K^+}$
- 794

795 The particle yield is extracted from the fit to the corresponding  $n\sigma_{dE/dx}^i$  distribution (corrected  
 796 only for the energy loss [1] and vertexing). As shown in Fig. 8.8, the  $dE/dx$  of each particle  
 797 type merge at large  $p_T$ . Hence, the particle identification is limited. Pions can be identified  
 798 in the momentum range of  $0.2 - 0.7$  GeV/c, kaons in  $0.3 - 0.65$  GeV/c and (anti)protons in  
 799  $0.4 - 1.0$  GeV/c.

## 800 8.6 Antiparticle-to-Particle Ratios

801 The following steps were taken to correct an identified antiparticle to particle (pion, kaon, proton  
 802 and their antiparticle) multiplicity ratios as a function of  $p_T$  in three ranges of  $\xi$ :

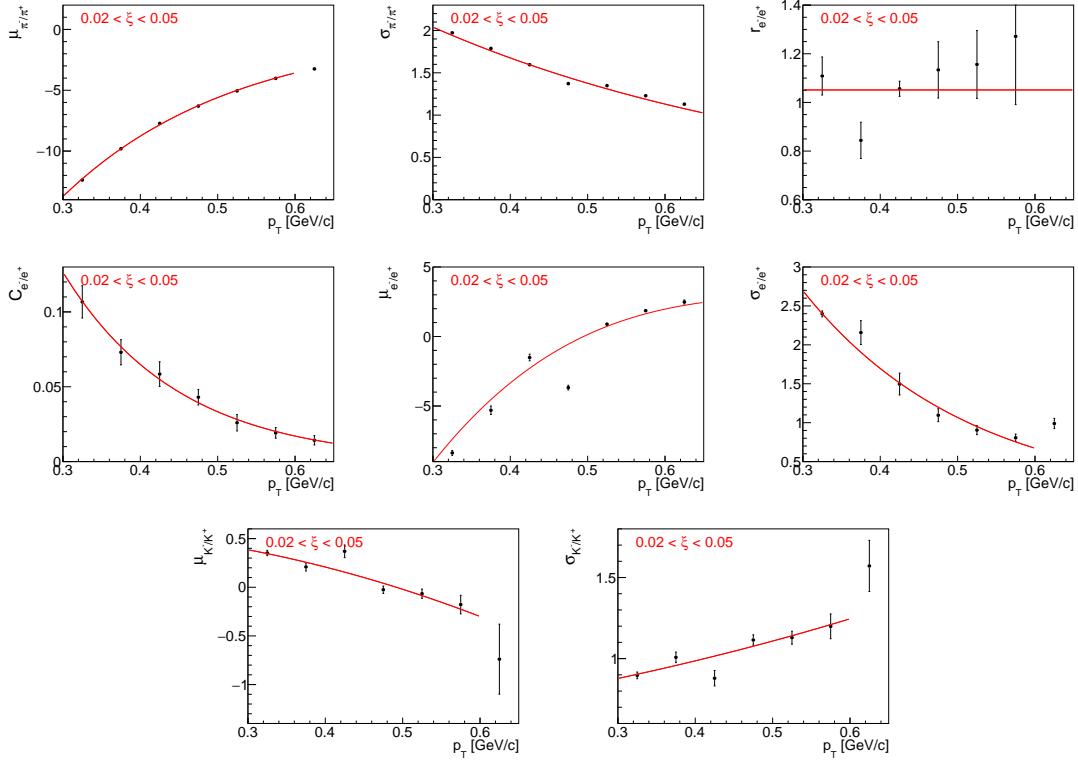


Figure 8.11: Means, widths and electron yields of each  $n\sigma_{dE/dx}^{K^\pm}$  fit as a function of  $p_T$ . The red line on each plot is a fit function to stabilize and constrain the Gaussian fit parameters for the final fitting step.

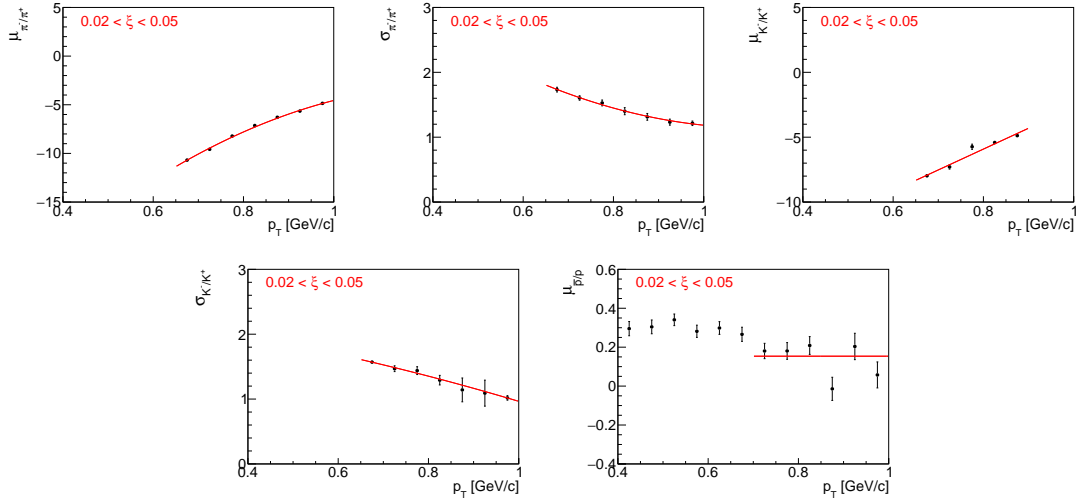


Figure 8.12: Means and widths of each  $n\sigma_{dE/dx}^{\bar{p}/p}$  fit as a function of  $p_T$ . The red line on each plot is a fit function to stabilize and constrain the Gaussian fit parameters for the final fitting step.

- The raw identified particle yields were obtained through multi-Gaussian fits to the  $n\sigma_{dE/dx}^i$  distributions (Sec. 8.5), where the vertex reconstruction and energy loss corrections [1] were applied. The latter depends on the particle type.

- The non-SD background was subtracted. It was assumed that the accidental background does not depend on the particle type and for this reason it was not subtracted.
- The particle yields were corrected for track reconstruction efficiencies [1], which depend on the particle type and charge. These corrections were averaged over  $\eta$  and  $V_z$ . The ratio of particle to antiparticle TPC-TOF efficiencies is shown in Fig. 8.13. It weakly depends on  $\xi$  range, therefore, only sample results for single range of  $0.02 < \xi < 0.05$  are presented.
- The background from non-primary tracks was subtracted (Sec. 4.2):
  - $\pi^\pm$ : weak decays pions, muon contribution and background from detector dead-material interactions,
  - $p$ : background from detector dead-material interactions,
  - $p, \bar{p}$ : reconstructed tracks which have the appropriate number of common hit points with true-level particle, but the distance between them is too large (this background is negligibly small for other particle types),
  - fake track contribution was assumed to be the same for each particle type, hence, it was not subtracted.
- Since track and  $\xi$  migrations, and BBC-small efficiency, do not depend on the particle type and charge, these corrections are not applied.
- Finally, each antiparticle  $p_T$  distribution was divided by the corresponding particle  $p_T$  distribution to obtain fully corrected identified antiparticle to particle multiplicity ratios.
- Additionally, the average antiparticle to particle ratios over fiducial region of  $p_T$  in each  $\xi$  region were calculated.

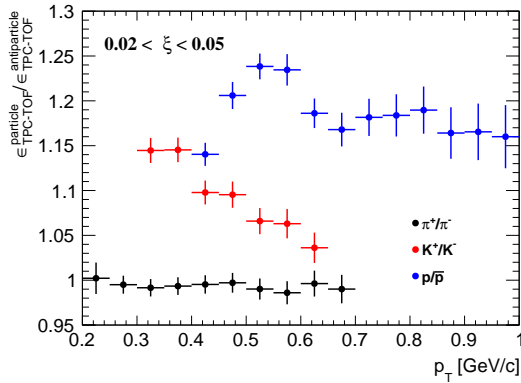


Figure 8.13: Ratio of particle to antiparticle TPC-TOF efficiencies for  $0.02 < \xi < 0.05$ .

## 9. Systematic Uncertainties

Apart from the statistical uncertainties there are also systematic uncertainties originating from inefficiencies and limitations of the measurement devices and techniques.

The following sources of systematic uncertainties were considered:

- the effect of off-time pile-up on TPC track reconstruction efficiency [1],
- the uncertainty of TPC track reconstruction efficiency related to the description of dead-material in simulation [1],
- representation of data sample in embedding MC [1],
- variation in the track quality cuts [1],
- non-primary track background contribution (Sec. 4.2),
- fake track background contribution (Sec. 4.2),
- TOF system simulation accuracy [1],
- accidental background contribution (Sec. 4.1),
- the effect of alternative model of hadronisation on BBC-small efficiency (Sec. 6.2),
- non-SD background contribution (Sec. 5),
- non-closure (Sec 8.3),
- the effect of alternative model on  $\epsilon_m$  correction (Sec. 8.1),
- non-closure of  $N_{\text{ev}}$ , applied only to  $p_T$  and  $\bar{\eta}$  distributions,
- difference in the distributions calculated separately for events in which forward proton is on one and the other side of the IP (east-west, Sec 8.4).

Some of the systematic uncertainties on  $1/N \, dN/dn_{\text{ch}}$  (related to TPC and TOF reconstruction efficiencies, fake track background contribution) are propagated by randomly removing and adding tracks in the  $n_{\text{sel}}$  distribution before unfolding procedure. For each track, a random number is generated. If this number is smaller than the absolute value of systematic uncertainty, then  $n_{\text{sel}}$  is increased or decreased, depending on the sign of systematic uncertainty.

Figures 9.1 to 9.3 show the components contributing to the total systematic uncertainty for charged particle distributions without the identification. The dominant systematic uncertainty for  $p_T$  and  $n_{\text{ch}}$  distributions is related to TOF system simulation accuracy. It affects mainly low- $p_T$  particles, where it is about 6%, and large charged particle multiplicities, where it varies up to 50% for  $n_{\text{ch}} = 8$  and  $0.02 < \xi < 0.05$ . In case of  $\bar{\eta}$  distribution, the systematic uncertainty on TOF mainly refers to charged particles produced at the edge of the fiducial region, for which it is about 4%. The largest (up to 35%) systematic uncertainty for  $\langle \bar{\eta} \rangle$ , is related to the observed difference in the distributions calculated separately with respect to the forward proton direction. The rest of the components have smaller contributions to the total systematic uncertainty. The systematic uncertainty on non-closure is at the level of 2% which proves the accuracy of the correction procedure.

Figures 9.4 to 9.7 show breakdown of all different systematics for the antiparticle-to-particle multiplicity ratio distributions. An additional systematic contribution for  $\bar{p}/p$  multiplicity ratio due to proton background estimation was introduced. Since most of the corrections are the same for particle and its antiparticle, nearly all systematic uncertainties cancel out in the antiparticle-to-particle ratios. The largest sources of systematics, which do not, are related to proton background estimation and dead-material effect on TPC track reconstruction efficiency. The former was found to be up to 5%, whereas the latter varies up to 2% for low- $p_T$   $\bar{p}/p$  multiplicity ratio.

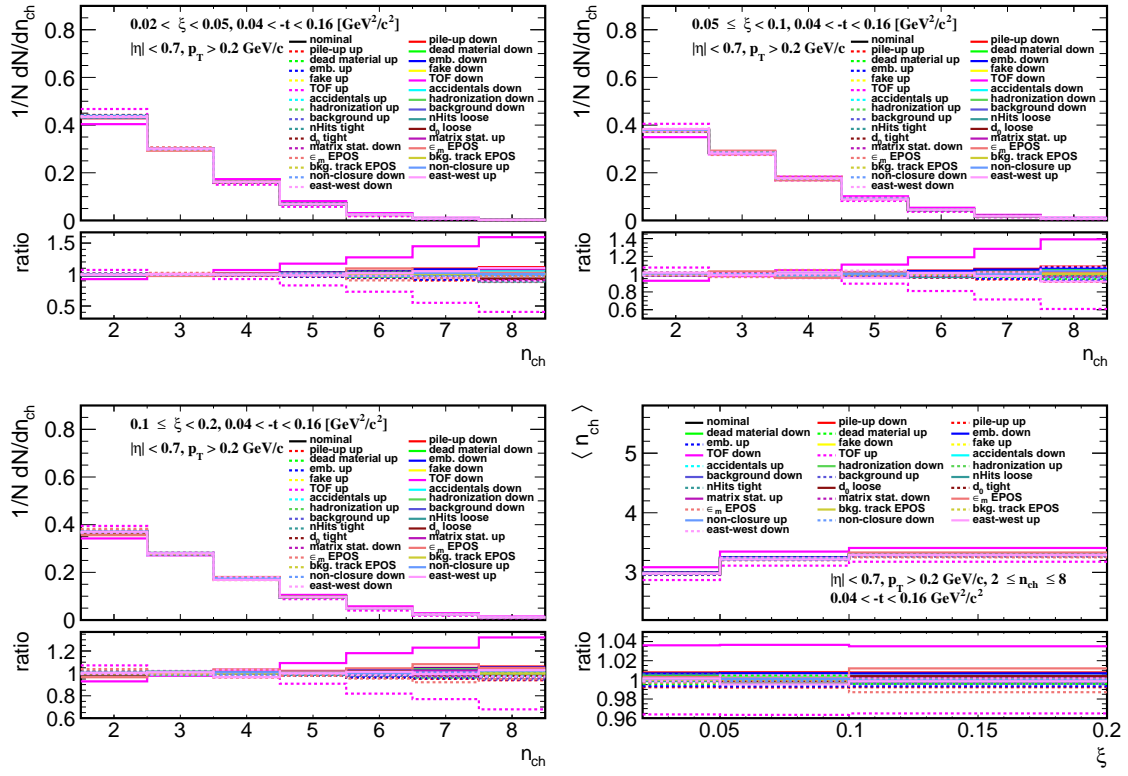


Figure 9.1: Components of the systematic uncertainties for the charged particle multiplicity in three  $\xi$  regions and for the average charged particle multiplicity.

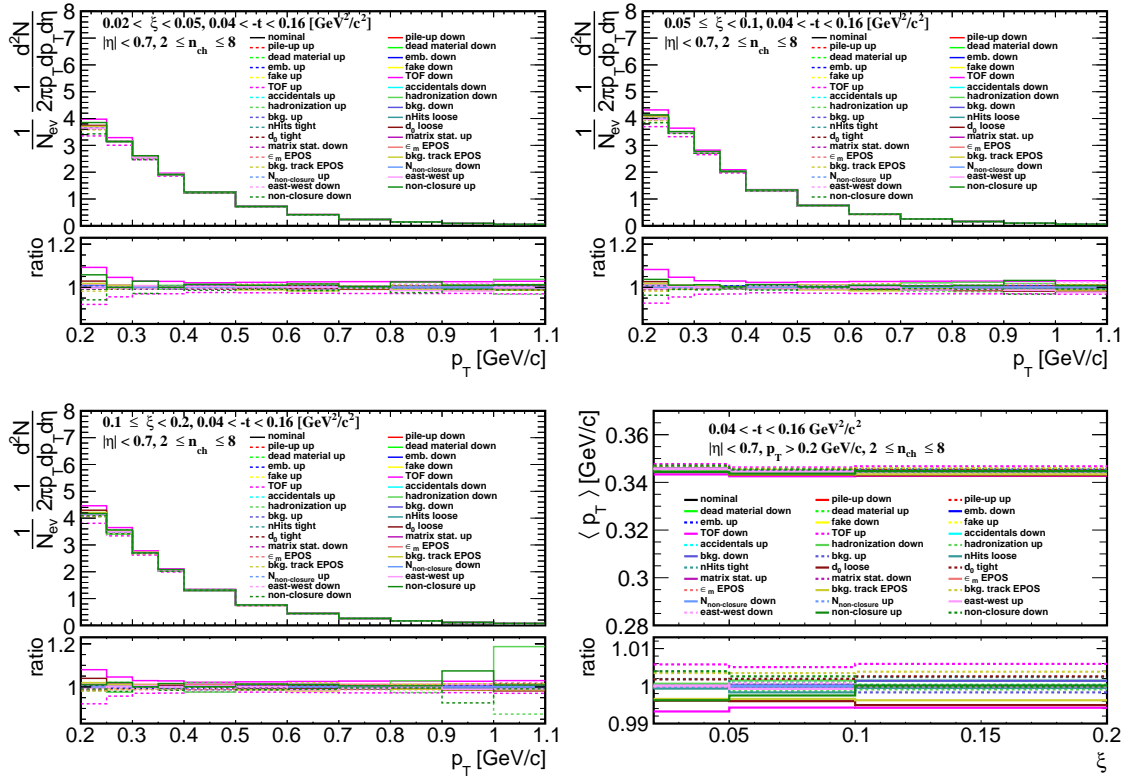


Figure 9.2: Components of the systematic uncertainties for  $p_T$  distributions in three  $\xi$  regions and for an average  $p_T$  distribution.

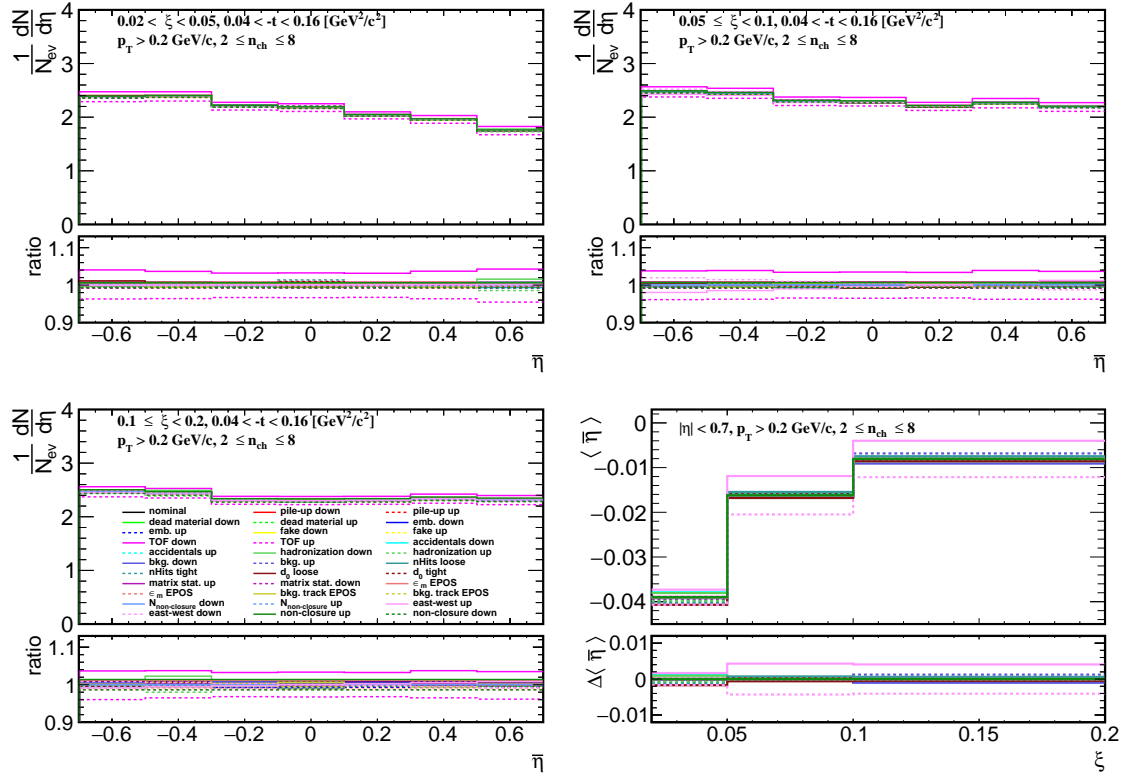


Figure 9.3: Components of the systematic uncertainties for  $\bar{\eta}$  distributions in three  $\xi$  regions and for an average  $\bar{\eta}$  distribution.

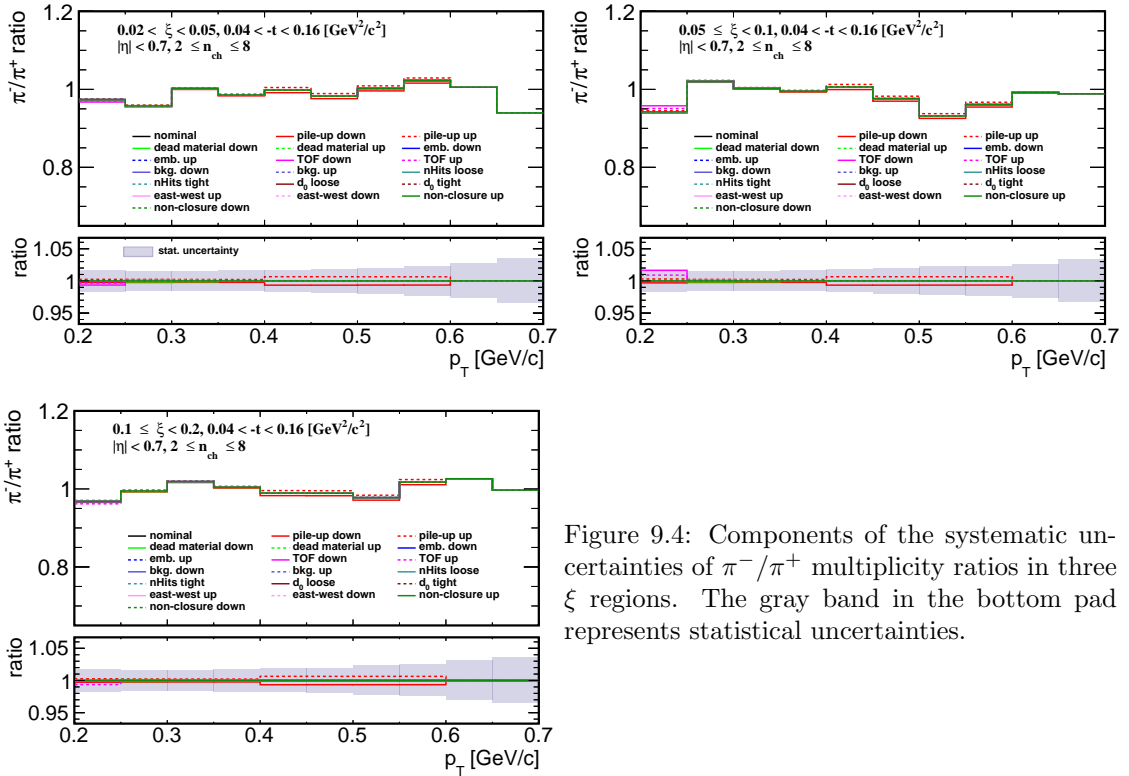


Figure 9.4: Components of the systematic uncertainties of  $\pi^-/\pi^+$  multiplicity ratios in three  $\xi$  regions. The gray band in the bottom pad represents statistical uncertainties.



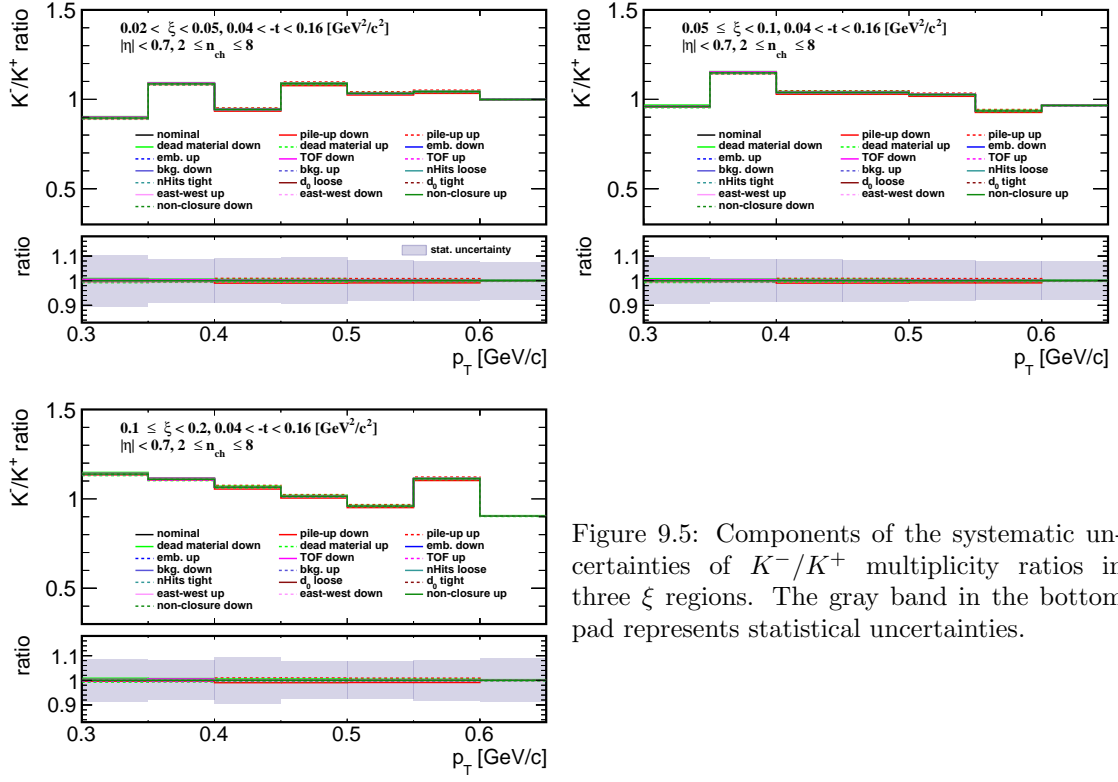


Figure 9.5: Components of the systematic uncertainties of  $K^-/K^+$  multiplicity ratios in three  $\xi$  regions. The gray band in the bottom pad represents statistical uncertainties.

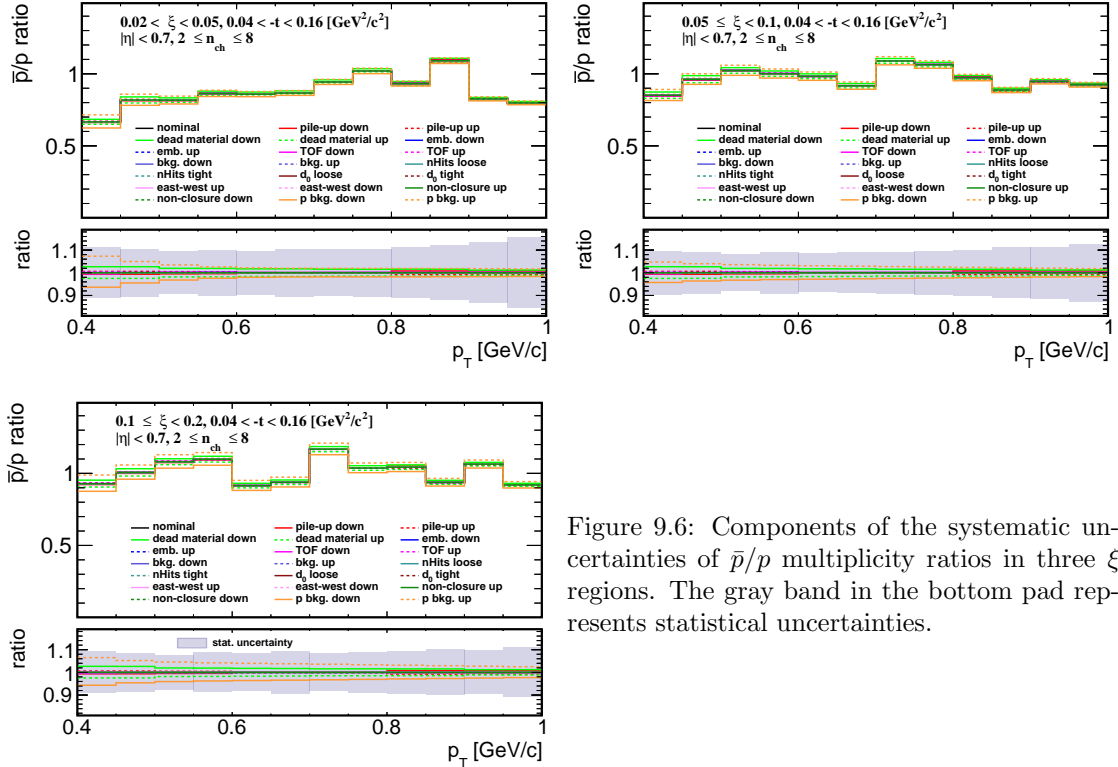


Figure 9.6: Components of the systematic uncertainties of  $\bar{p}/p$  multiplicity ratios in three  $\xi$  regions. The gray band in the bottom pad represents statistical uncertainties.

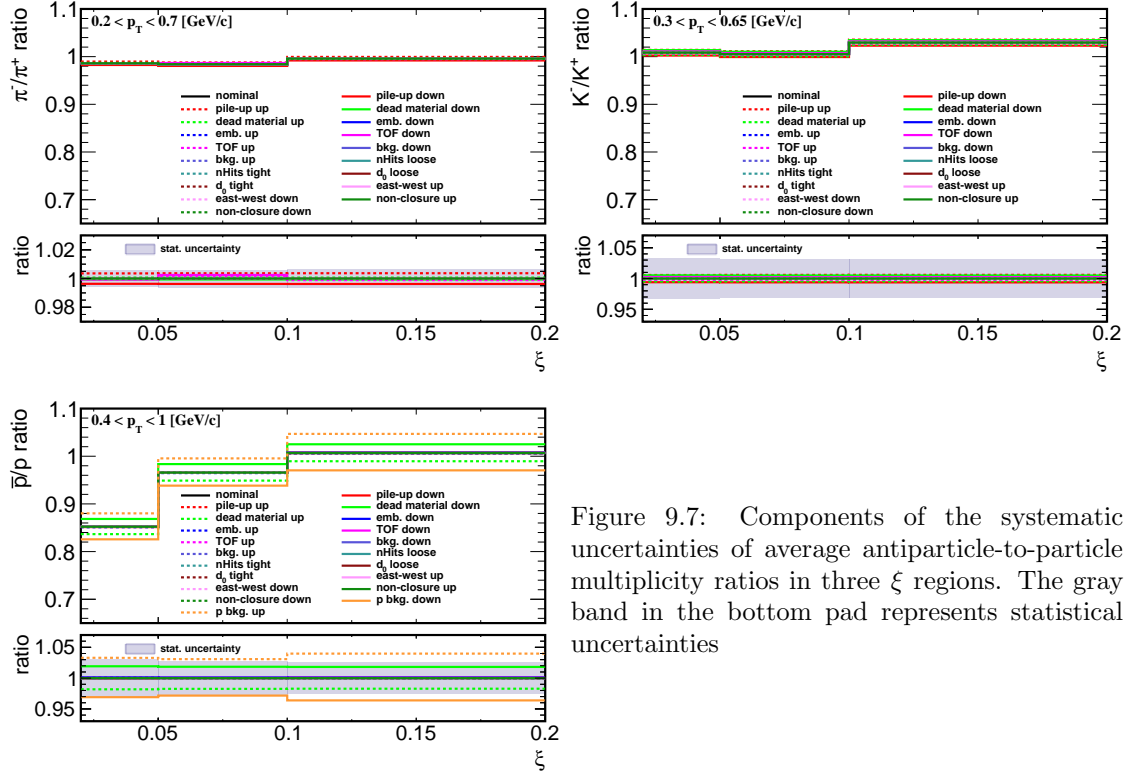


Figure 9.7: Components of the systematic uncertainties of average antiparticle-to-particle multiplicity ratios in three  $\xi$  regions. The gray band in the bottom pad represents statistical uncertainties

# 10. Results

In the following section, the final-state charged particle distributions are compared with various SD MC predictions, i.e.

- PYTHIA 8 4C (SaS),
- PYTHIA 8 A2 (MBR),
- PYTHIA 8 A2 (MBR-tuned),
- HERWIG 7,
- EPOS LHC with combined two classes of processes: diffractive (EPOS-SD) modelled by Pomeron exchange and non-diffractive modelled by low mass excitation of the proton remnant (EPOS-SD'),
- EPOS LHC SD'.

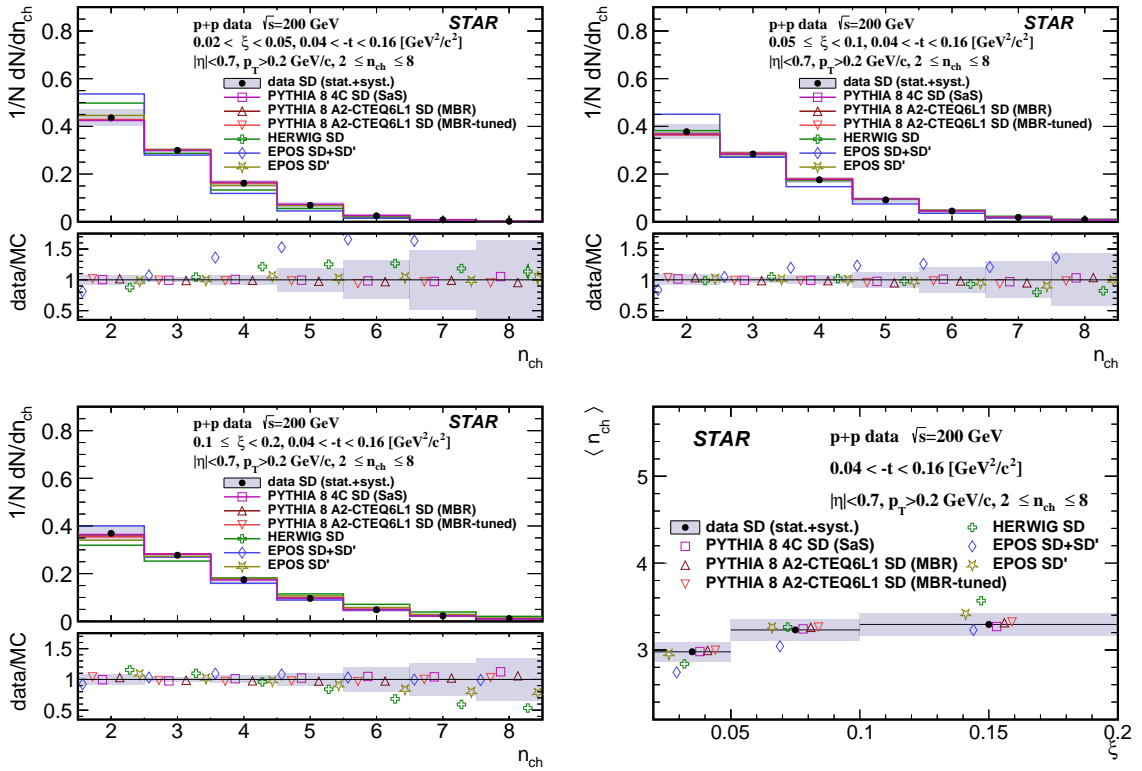


Figure 10.1: Primary charged-particle multiplicity shown separately for the three ranges of  $\xi$ : (top left)  $0.02 < \xi < 0.05$ , (top right)  $0.05 < \xi < 0.1$ , (bottom left)  $0.1 < \xi < 0.2$  and (bottom right) the mean multiplicity  $\langle n_{ch} \rangle$  as a function of  $\xi$ .

In all figures, data are shown as solid points with error bars representing the statistical uncertainties. Gray boxes represent statistical and systematic uncertainties added in quadrature. Predictions from MC models are shown as colour histograms and markers. The lower panel in each figure shows the ratio of data to the models' predictions. All results are presented separately for three ranges of  $\xi$ :  $0.02 < \xi < 0.05$ ,  $0.05 < \xi < 0.1$ ,  $0.1 < \xi < 0.2$ .

Figure 10.1 shows primary charged-particle multiplicity separately for the three ranges of  $\xi$  and the mean multiplicity  $\langle n_{\text{ch}} \rangle$  as a function of  $\xi$ . Data follow the expected increase of  $\langle n_{\text{ch}} \rangle$  with  $\xi$  due to the larger diffractive masses probed by increasing  $\xi$  in SD process. The shapes of the measured distributions are reproduced reasonably well by all models except EPOS SD+SD' and HERWIG-SD which predicts smaller  $\langle n_{\text{ch}} \rangle$  for  $0.02 < \xi < 0.1$  and  $0.02 < \xi < 0.05$ , respectively. HERWIG-SD predicts too large  $\langle n_{\text{ch}} \rangle$  for  $0.1 < \xi < 0.2$ .

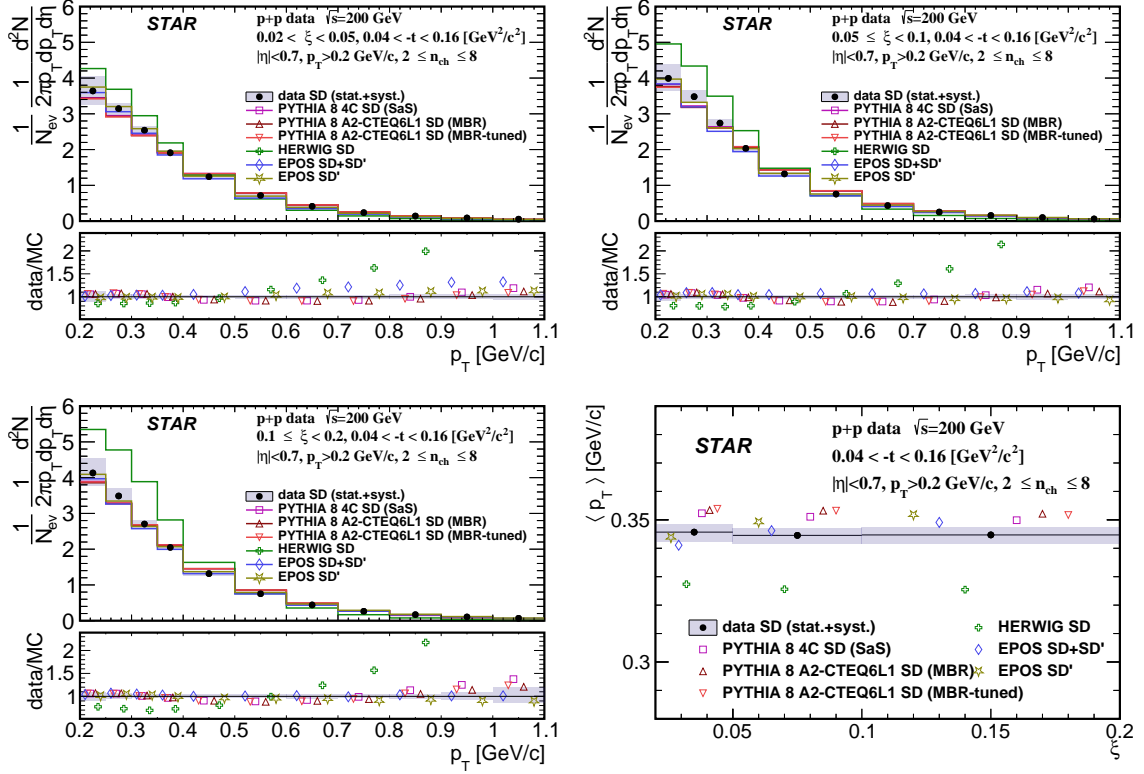


Figure 10.2: Primary charged-particle multiplicities as a function of  $p_T$  shown separately for the three ranges of  $\xi$ : (top left)  $0.02 < \xi < 0.05$ , (top right)  $0.05 < \xi < 0.1$ , (bottom left)  $0.1 < \xi < 0.2$  and (bottom right) the mean transverse momentum  $\langle p_T \rangle$  as a function of  $\xi$ .

Figure 10.2 shows primary charged-particle multiplicities as a function of  $p_T$  separately for the three ranges of  $\xi$  and the mean transverse momentum  $\langle p_T \rangle$  as a function of  $\xi$ . Data show that  $\langle p_T \rangle$  depends very weakly on  $\xi$ . Models describe data fairly well except HERWIG-SD which predicts much steeper dependence of particle density with  $p_T$  in all three  $\xi$  ranges.

Figure 10.3 shows primary charged-particle multiplicity as a function of  $\eta$  separately for the three ranges of  $\xi$  and the mean pseudorapidity  $\langle \eta \rangle$  as a function of  $\xi$ . Data show expected flattening of the  $\eta$  distribution with increasing  $\xi$  which reflects SD event-asymmetry and fact that the gap-edge at large  $\xi$  is outside  $|\eta| < 0.7$  region leading to more flat distribution of particle density as a function of  $\eta$ . Models describe data fairly well except EPOS SD+SD', which predicts less steep dependence of particle density with  $\eta$  for  $0.02 < \xi < 0.1$ , and HERWIG-SD, which predicts steeper distribution for all three  $\xi$  ranges.

Figure 10.4 shows the ratio of production yields of  $\pi^-/\pi^+$  as a function of  $p_T$  separately for the three ranges of  $\xi$ . Data in all three  $\xi$  ranges are consistent with equal amounts of  $\pi^+$  and  $\pi^-$  with no significant  $p_T$  dependence. Models agree with data (except HERWIG) predicting on average small deviation from unity by  $\sim 2\%$  what is smaller than data uncertainties. HERWIG in first two  $\xi$  ranges predicts too large asymmetry between  $\pi^+$  and  $\pi^-$ .

Figure 10.5 shows the ratio of production yields of  $K^-/K^+$  as a function of  $p_T$  separately for

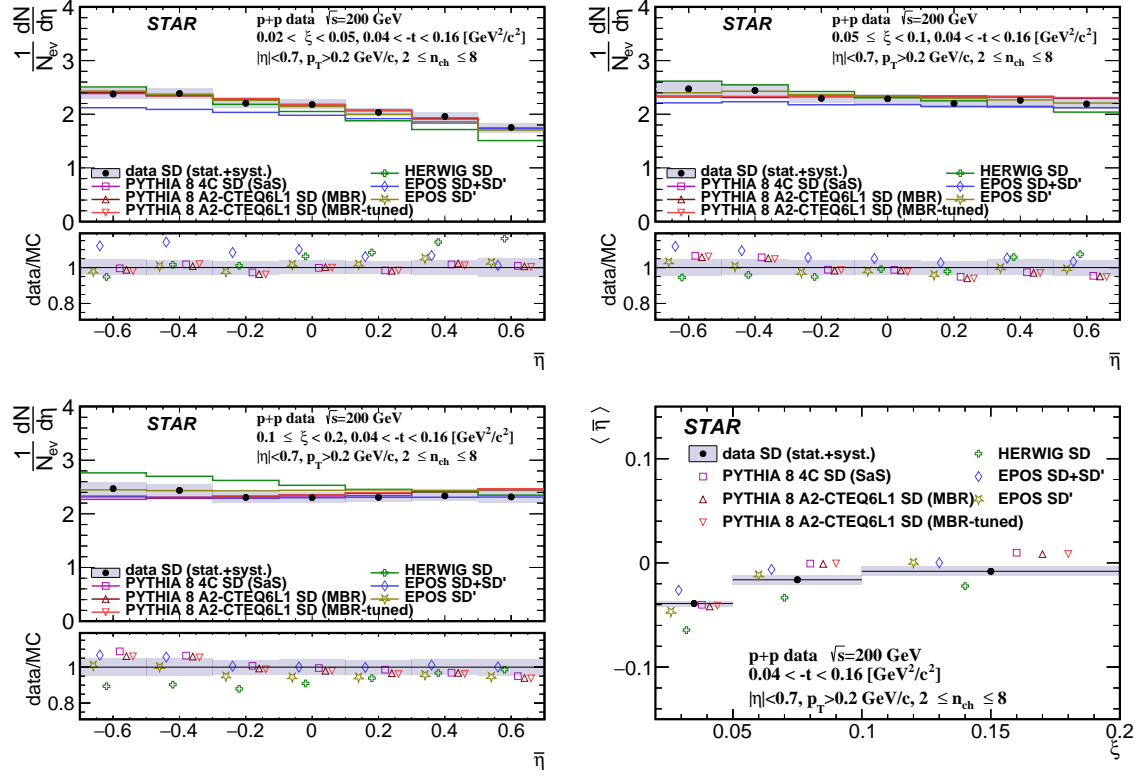


Figure 10.3: Primary charged-particle multiplicity as a function of  $\bar{\eta}$  shown separately for the three ranges of  $\xi$ : (top left)  $0.02 < \xi < 0.05$ , (top right)  $0.05 < \xi < 0.1$ , (bottom left)  $0.1 < \xi < 0.2$  and (bottom right) the mean pseudorapidity  $\langle \bar{\eta} \rangle$  as a function of  $\xi$ .

the three ranges of  $\xi$ . Data in all three  $\xi$  ranges are consistent with equal amounts of  $K^+$  and  $K^-$  with no  $p_T$  dependence. Models agree with data except HERWIG in the first  $\xi$  range predicting too large ratio of  $K^-$  to  $K^+$ .

Figure 10.6 shows the ratio of production yields of  $\bar{p}/p$  as a function of  $p_T$  separately for the three ranges of  $\xi$ . Data in the last two  $\xi$  ranges are consistent with equal amounts of  $p$  and  $\bar{p}$  with no  $p_T$  dependence. However, in the first  $\xi$  range at  $p_T < 0.7$  GeV/c data shows significant deviation from unity indicating a significant transfer of the baryon number from the forward to the central region. PYTHIA8, EPOS SD' and EPOS SD+SD' agree with data in the last two  $\xi$  ranges. In first  $\xi$  range PYTHIA8 and EPOS SD' predict small deviation from unity by  $\sim 5\%$  which is smaller than observed in data, whereas EPOS SD+SD' predicts an asymmetry between  $\bar{p}$  and  $p$  of  $\sim 30\%$  which is larger than observed in data except  $p_T < 0.5$  GeV/c. HERWIG predicts much larger baryon number transfer compared to data in first two  $\xi$  ranges and shows consistency with data in last  $\xi$  range.

Figure 10.7 shows mean ratio of production yields of  $\pi^-/\pi^+$ ,  $K^-/K^+$  and  $\bar{p}/p$  as a function of  $\xi$ .

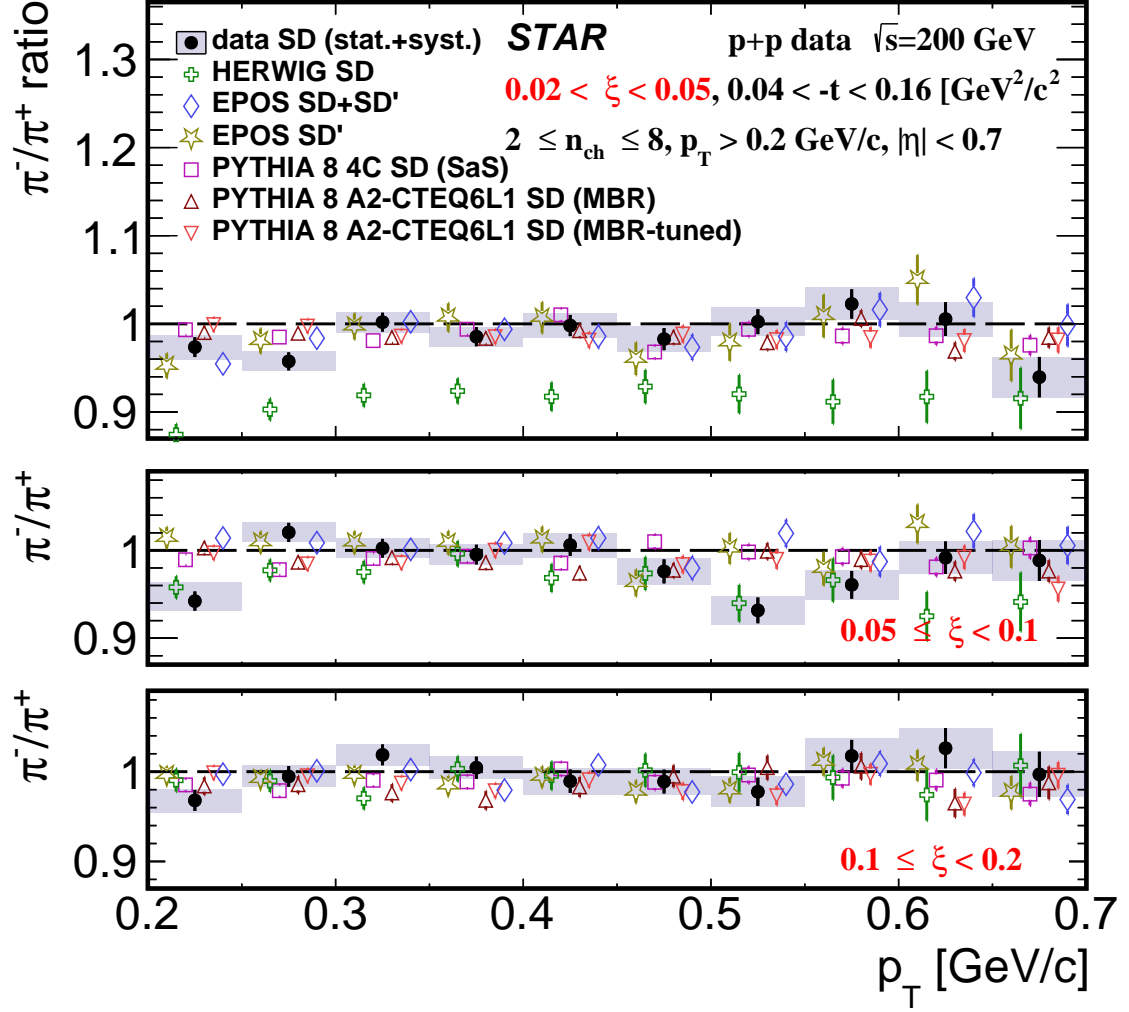


Figure 10.4: Ratio of production yields of  $\pi^-/\pi^+$  as a function of  $p_T$  shown separately for the three ranges of  $\xi$ : (top)  $0.02 < \xi < 0.05$ , (middle)  $0.05 < \xi < 0.1$ , (bottom)  $0.1 < \xi < 0.2$ .

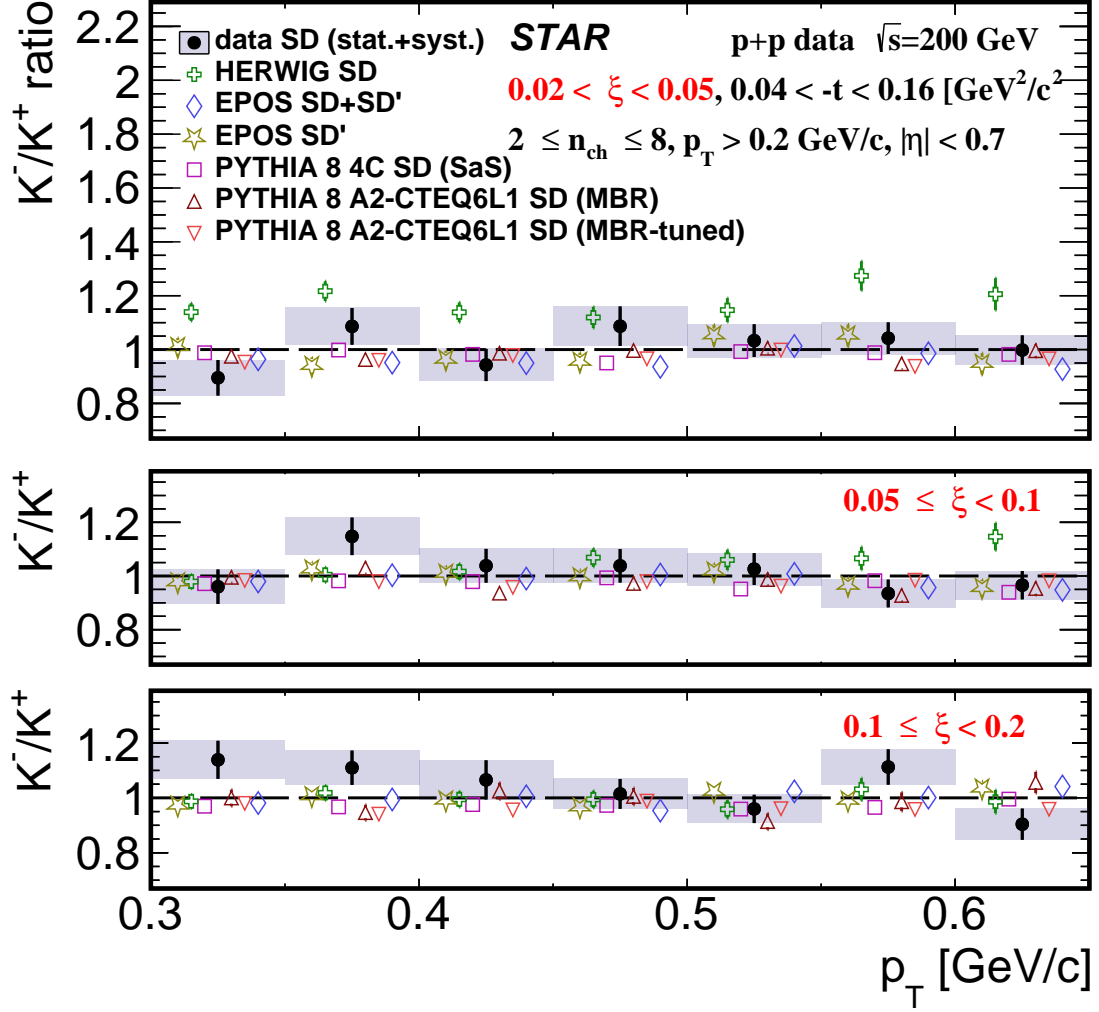


Figure 10.5: Ratio of production yields of  $K^-/K^+$  as a function of  $p_T$  shown separately for the three ranges of  $\xi$ : (top)  $0.02 < \xi < 0.05$ , (middle)  $0.05 < \xi < 0.1$ , (bottom)  $0.1 < \xi < 0.2$ .

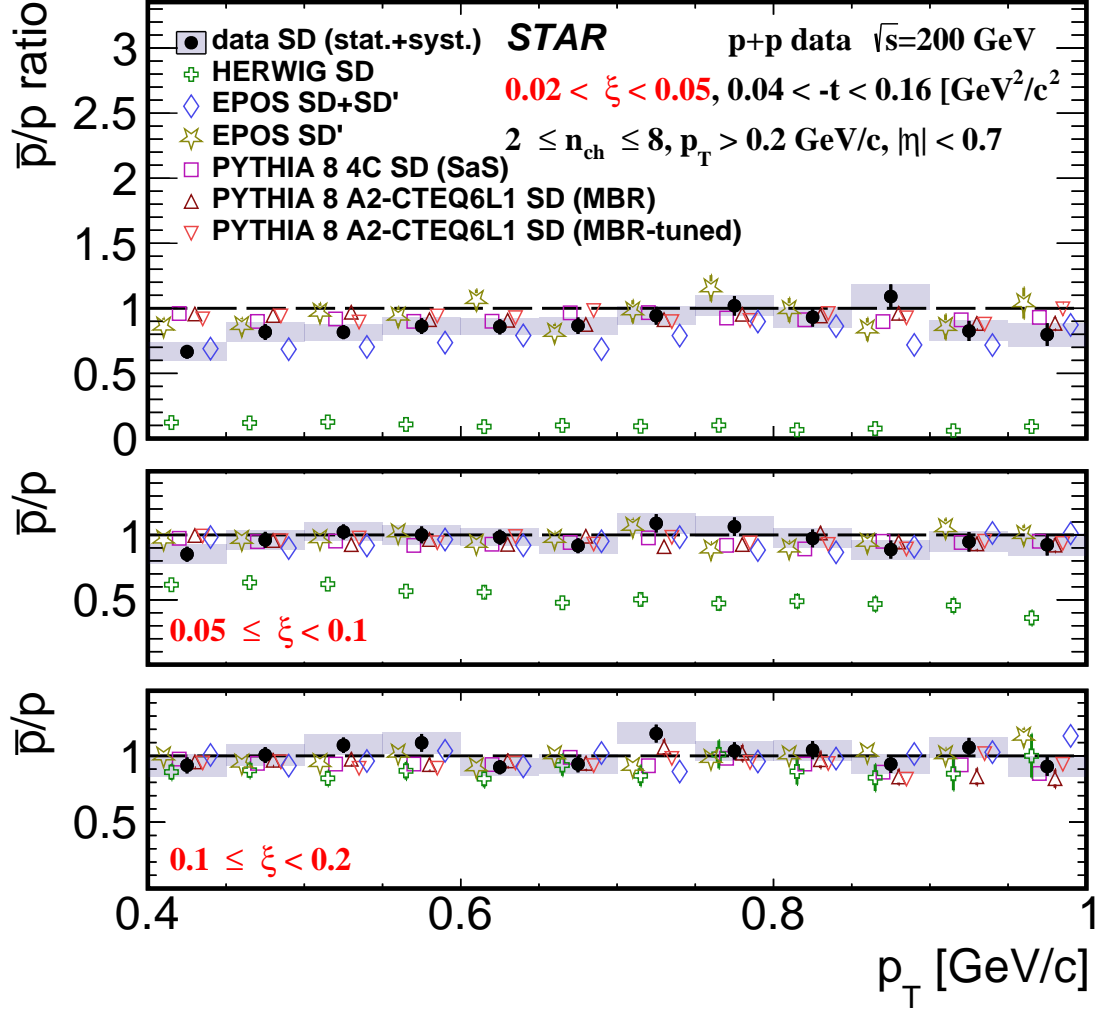


Figure 10.6: Ratio of production yields of  $\bar{p}/p$  as a function of  $p_T$  shown separately for the three ranges of  $\xi$ : (top)  $0.02 < \xi < 0.05$ , (middle)  $0.05 < \xi < 0.1$ , (bottom)  $0.1 < \xi < 0.2$ .



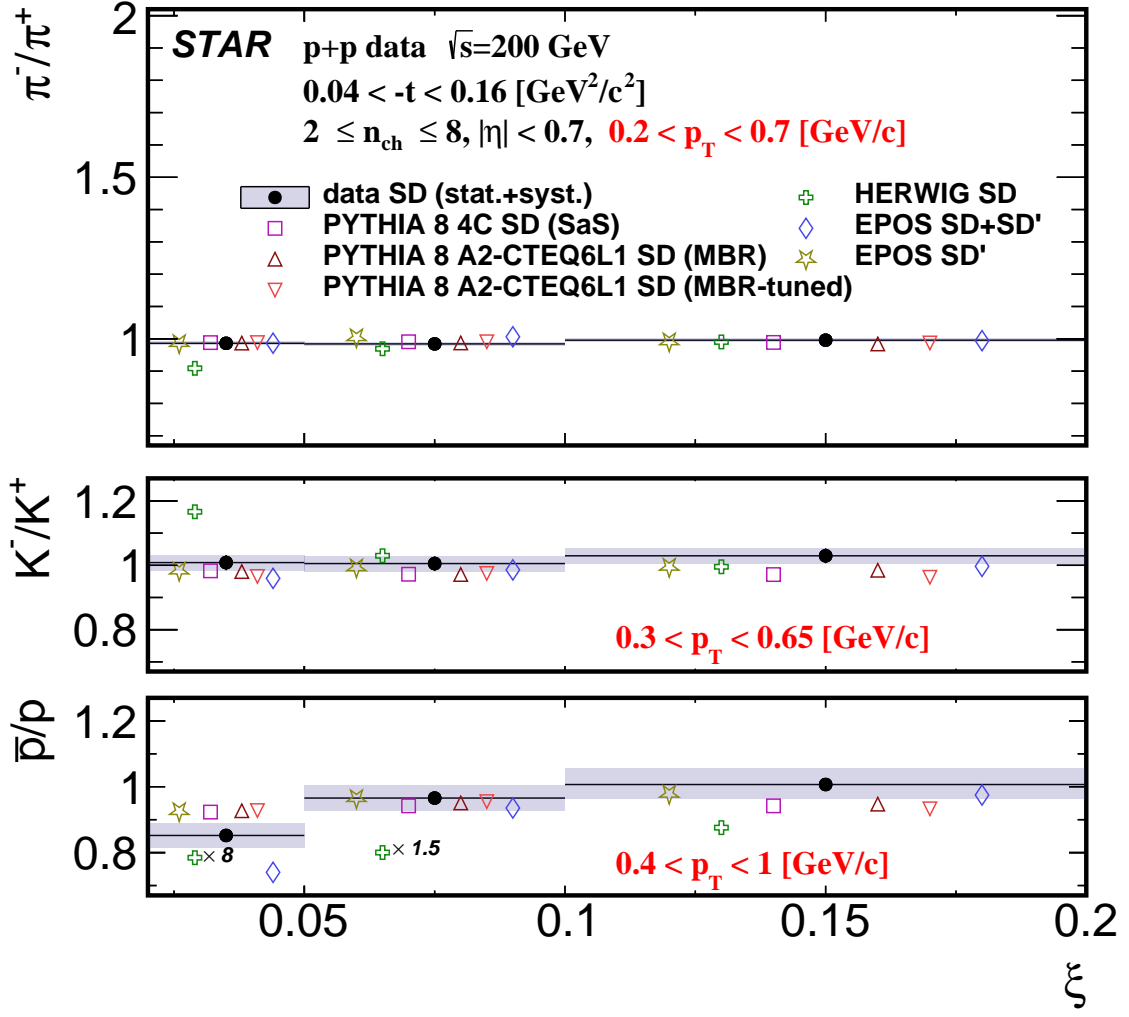


Figure 10.7: Ratio of production yields of  $\pi^-/\pi^+$ ,  $K^-/K^+$  and  $\bar{p}/p$  as a function of  $\xi$ .

## 11. Summary and Conclusions

Inclusive and identified (pion, kaon, proton and their antiparticles) charged particle production in Single Diffractive Dissociation process has been measured in proton-proton collisions at  $\sqrt{s} = 200$  GeV with the STAR detector at RHIC using data corresponding to an integrated luminosity of  $15 \text{ nb}^{-1}$ .

Significant differences are observed between the measured distributions of  $\xi$  and Monte Carlo model predictions. Amongst the models considered EPOS and PYTHIA8 (MBR) without suppression of diffractive cross sections at large  $\xi$  provide the best description of the data.

Primary-charged-particle multiplicity and its density as a function of pseudorapidity and transverse momentum are well described by PYTHIA8 and EPOS-SD' models. EPOS-SD and HERWIG do not describe the data.

$\pi^-/\pi^+$  and  $K^-/K^+$  production ratios are close to unity and consistent with most of model predictions except for EPOS-SD and HERWIG.

$\bar{p}/p$  production ratio shows a significant deviation from unity in the  $0.02 < \xi < 0.05$  range indicating a non-negligible transfer of the baryon number from the forward to the central region. Equal amount of protons and antiprotons are observed in the  $\xi > 0.05$  range. PYTHIA8 and EPOS-SD' agree with data for  $\xi > 0.05$ . For  $0.02 < \xi < 0.05$  they predict small deviations from unity (0.93) which is however higher than observed in data ( $0.85 \pm 0.04$ ). HERWIG and EPOS-SD predict much larger baryon number transfers compared to data for  $\xi < 0.1$  and show consistency with data for  $\xi > 0.1$ .

# Bibliography

- [1] L. Adamczyk, L. Fulek, and R. Sikora, *Supplementary note on diffractive analyses of 2015 proton-proton data*, <https://drupal.star.bnl.gov/STAR/starnotes/private/psn0732>, July, 2019.
- [2] B. Z. Kopeliovich and B. G. Zakharov, *Novel Mechanisms of Baryon Number Flow Over Large Rapidity Gap*, Z. Phys. **C43** (1989) 241.
- [3] F. W. Bopp, *Baryon transport in dual models and the possibility of a backward peak in diffraction*, in *New trends in high-energy physics: Experiment, phenomenology, theory. Proceedings, International School-Conference, Crimea 2000, Yalta, Ukraine, May 27-June 4, 2000*. arXiv:hep-ph/0007229 [hep-ph].
- [4] M. Anderson et al., *The STAR Time Projection Chamber: A Unique tool for studying high multiplicity events at RHIC*, Nucl. Instrum. Meth. **A499** (2003) 659–678, arXiv:nucl-ex/0301015 [nucl-ex].
- [5] R. Brun, F. Bruyant, M. Maire, A. C. McPherson, and P. Zancarini, *GEANT3*, CERN-DD-EE-84-1 (1987).
- [6] GEANT4 Collaboration, S. Agostinelli et al., *GEANT4: A Simulation toolkit*, Nucl. Instrum. Meth. **A506** (2003) 250–303.
- [7] T. Sjöstrand, S. Mrenna, and P. Z. Skands, *PYTHIA 6.4 Physics and Manual*, JHEP **05** (2006) 026.
- [8] R. Ciesielski and K. Goulios, *MBR Monte Carlo Simulation in PYTHIA8*, PoS **ICHEP2012** (2013) 301, arXiv:1205.1446 [hep-ph].
- [9] *Roman Pot Phase II\* - online DAQ monitoring*, <https://online.star.bnl.gov/rp/pp200/>.
- [10] *STAR RunLog Browser*, <https://online.star.bnl.gov/RunLogRun15/>.
- [11] W. Fischer, *Run Overview of the Relativistic Heavy Ion Collider*, <http://www.agrhhichome.bnl.gov/RHIC/Runs/>.
- [12] STAR Collaboration, J. Adam et al., *Results on Total and Elastic Cross Sections in Proton-Proton Collisions at  $\sqrt{s} = 200$  GeV*, arXiv:2003.12136 [hep-ex].
- [13] STAR Collaboration, B. I. Abelev et al., *Systematic Measurements of Identified Particle Spectra in  $pp$ ,  $d^+$  Au and Au+Au Collisions from STAR*, Phys. Rev. **C79** (2009) 034909, arXiv:0808.2041 [nucl-ex].
- [14] ATLAS Collaboration, G. Aad et al., *Charged-particle distributions in  $\sqrt{s} = 13$  TeV  $pp$  interactions measured with the ATLAS detector at the LHC*, Phys. Lett. **B758** (2016) 67–88, arXiv:1602.01633 [hep-ex].

- 978 [15] G. D'Agostini, *A Multidimensional unfolding method based on Bayes' theorem*, Nucl.  
979 Instrum. Meth. **A362** (1995) 487–498.
- 980 [16] H. Bichsel, *A method to improve tracking and particle identification in TPCs and silicon*  
981 *detectors*, Nucl. Instrum. Meth. **A562** (2006) 154–197.

# Appendices

## 983 A. Proton and Antiproton DCA 984 Distributions

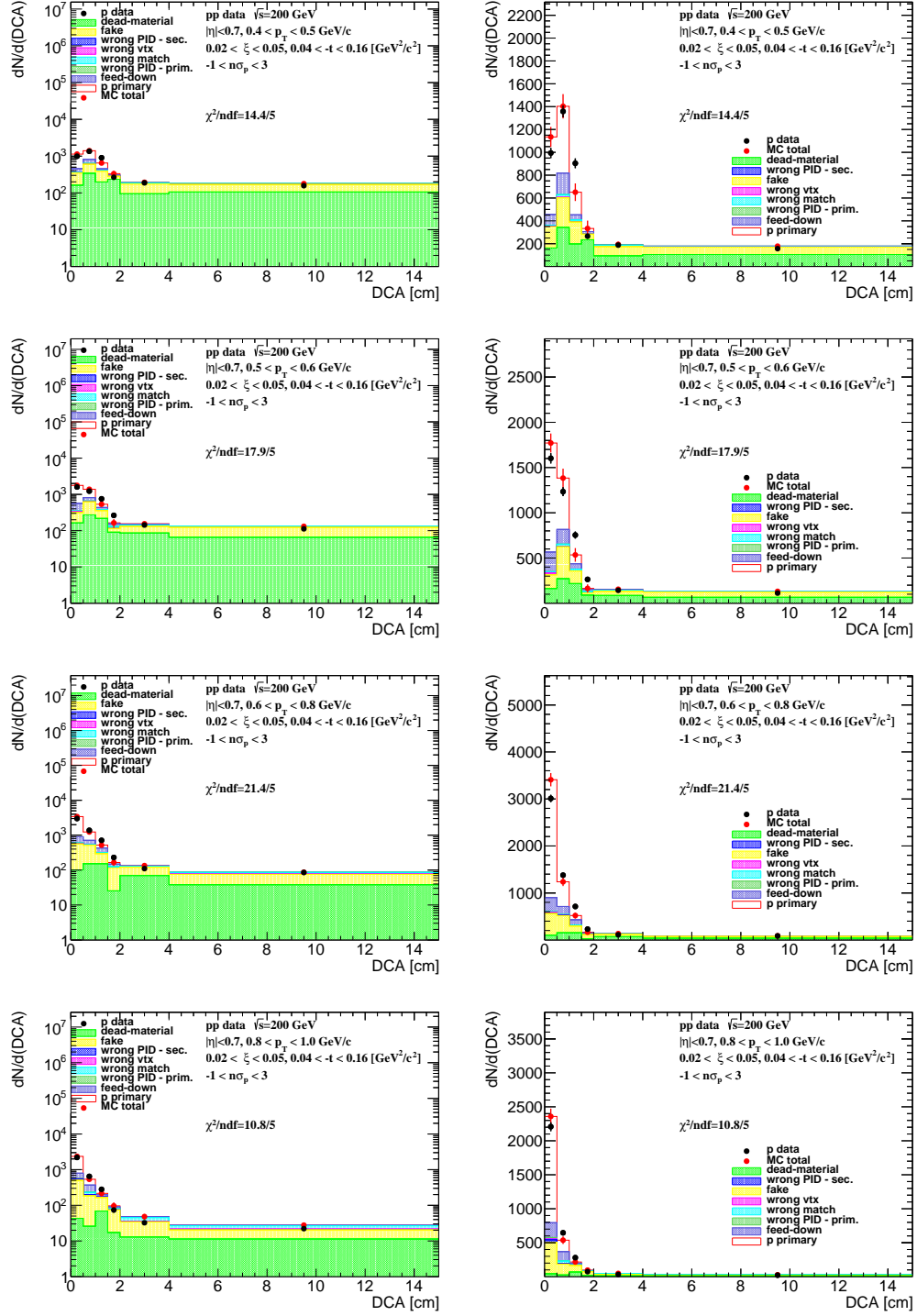


Figure A.1: Distributions of DCA for protons in SD interactions with  $0.02 < \xi < 0.05$  and loose selection.

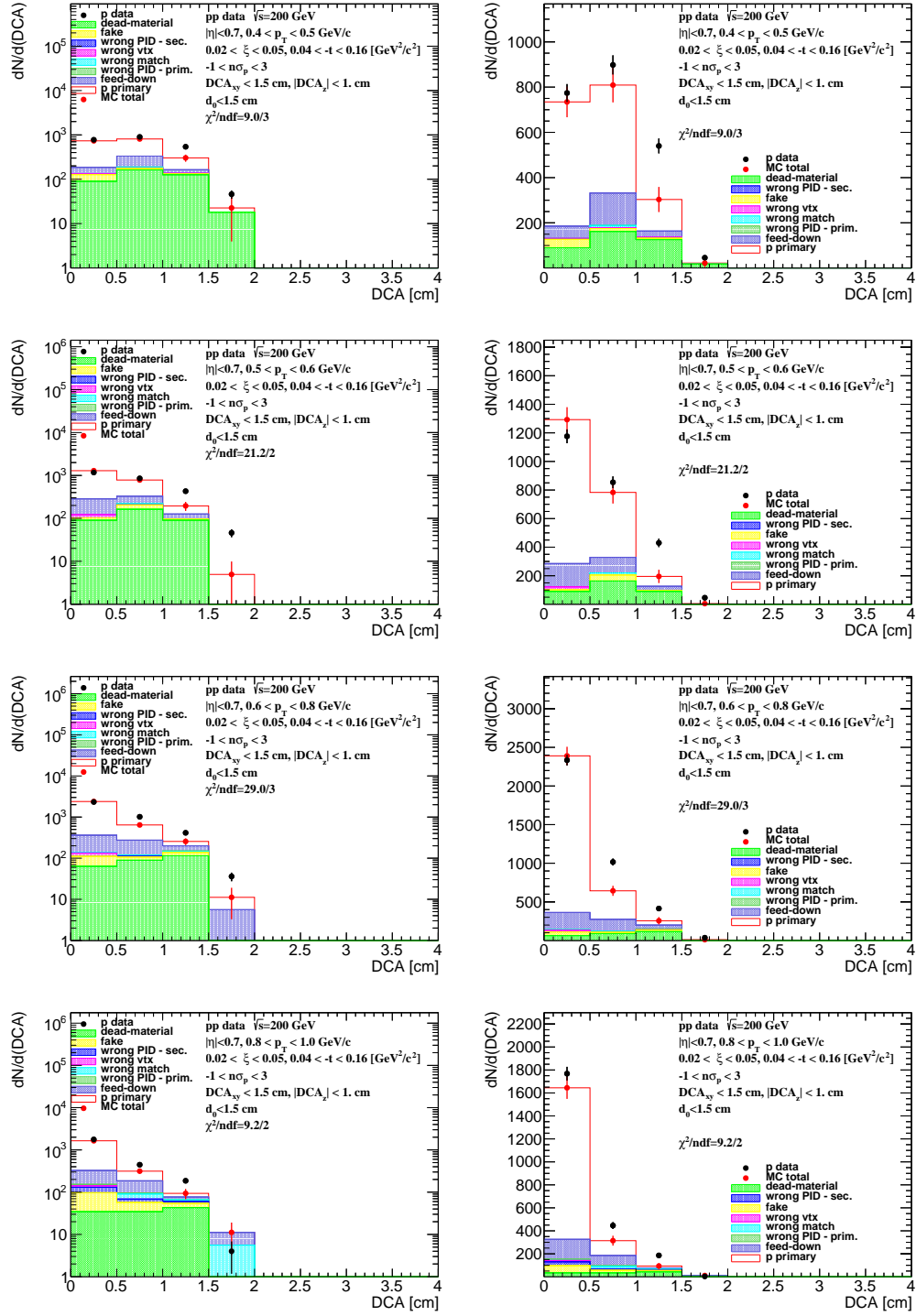


Figure A.2: Distributions of DCA for protons in SD interactions with  $0.02 < \xi < 0.05$  and normal selection.



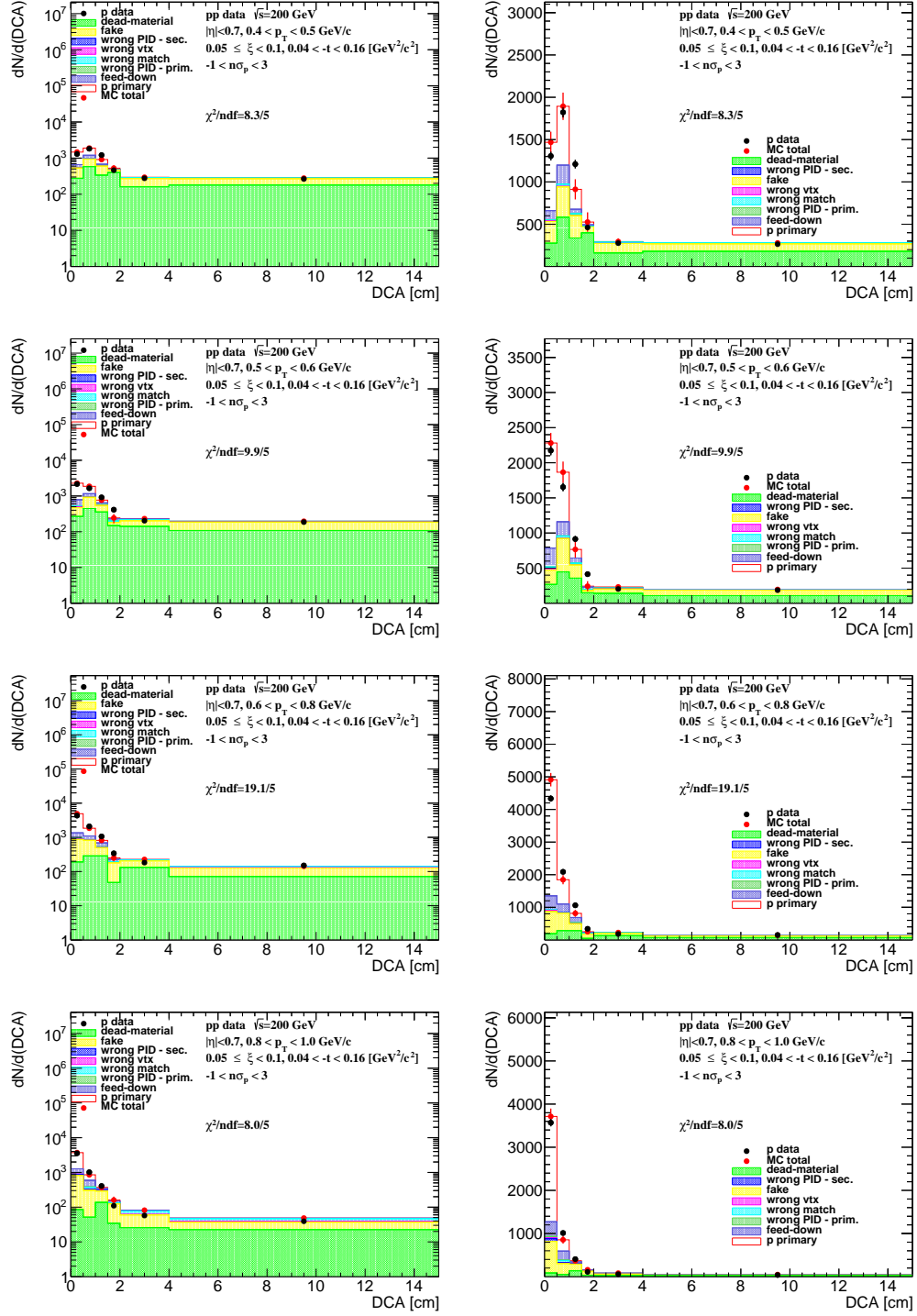


Figure A.3: Distributions of DCA for protons in SD interactions with  $0.05 < \xi < 0.1$  and loose selection.

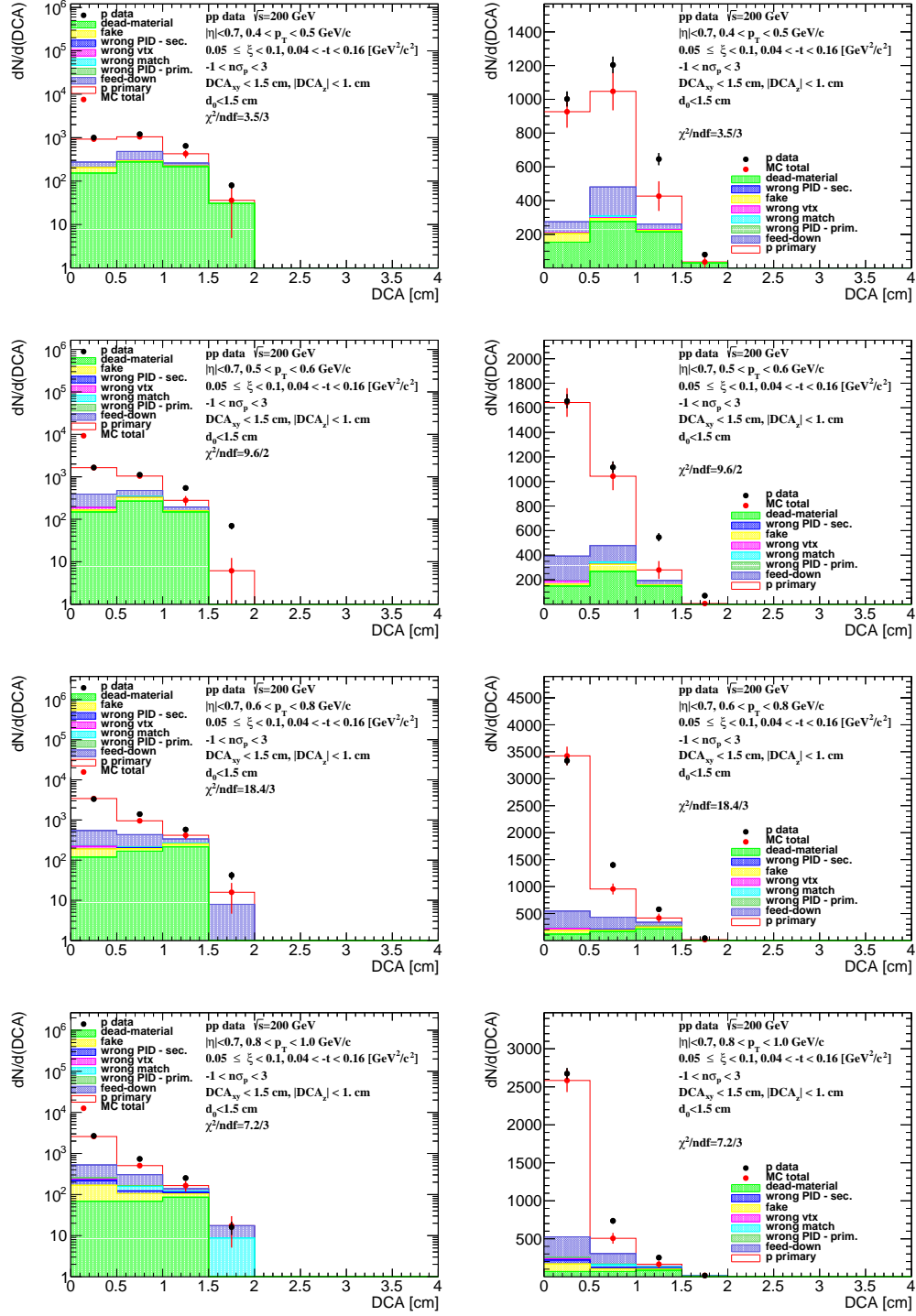


Figure A.4: Distributions of DCA for protons in SD interactions with  $0.05 < \xi < 0.1$  and normal selection.

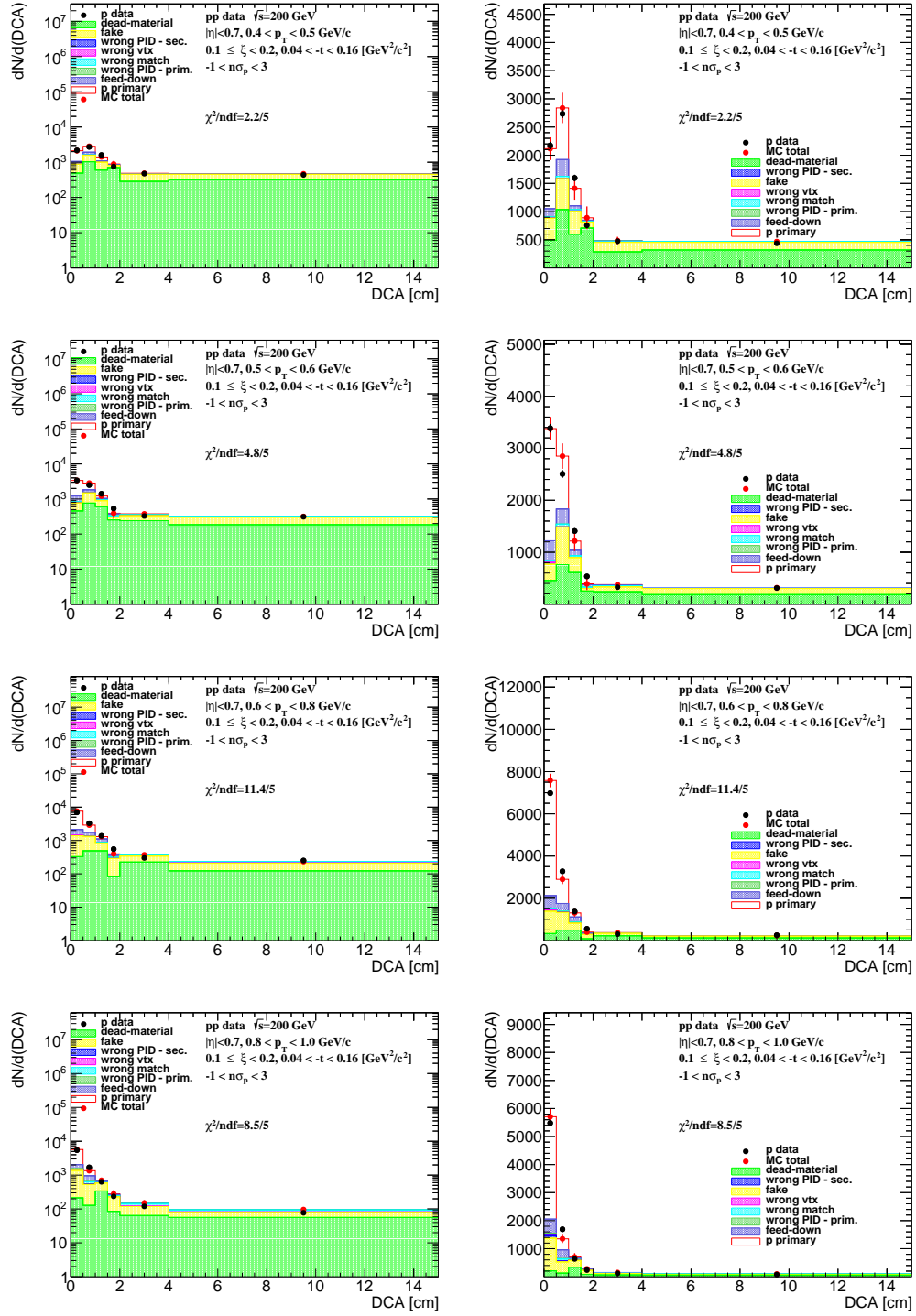


Figure A.5: Distributions of DCA for protons in SD interactions with  $0.1 < \xi < 0.2$  and loose selection.

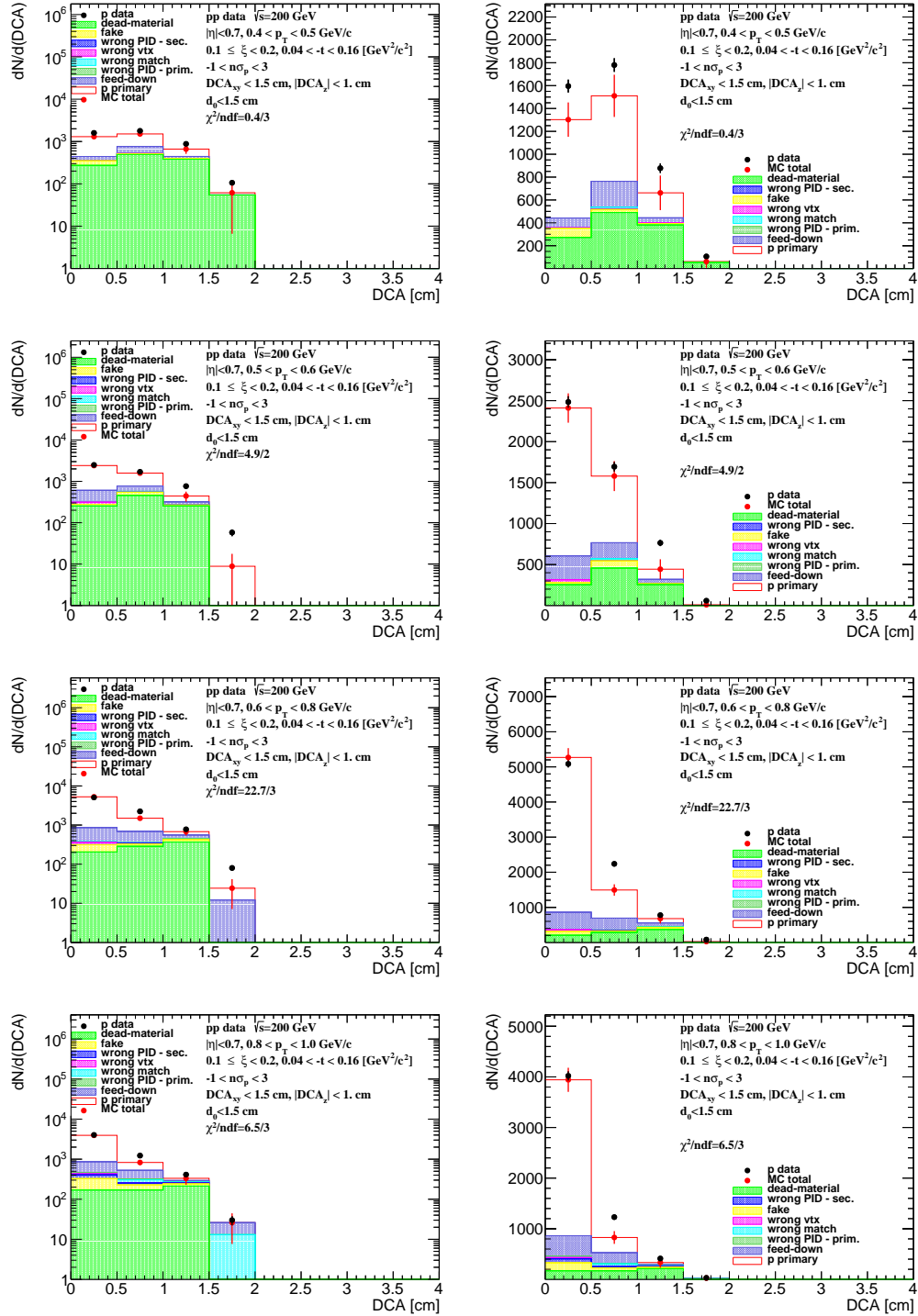


Figure A.6: Distributions of DCA for protons in SD interactions with  $0.1 < \xi < 0.2$  and normal selection.

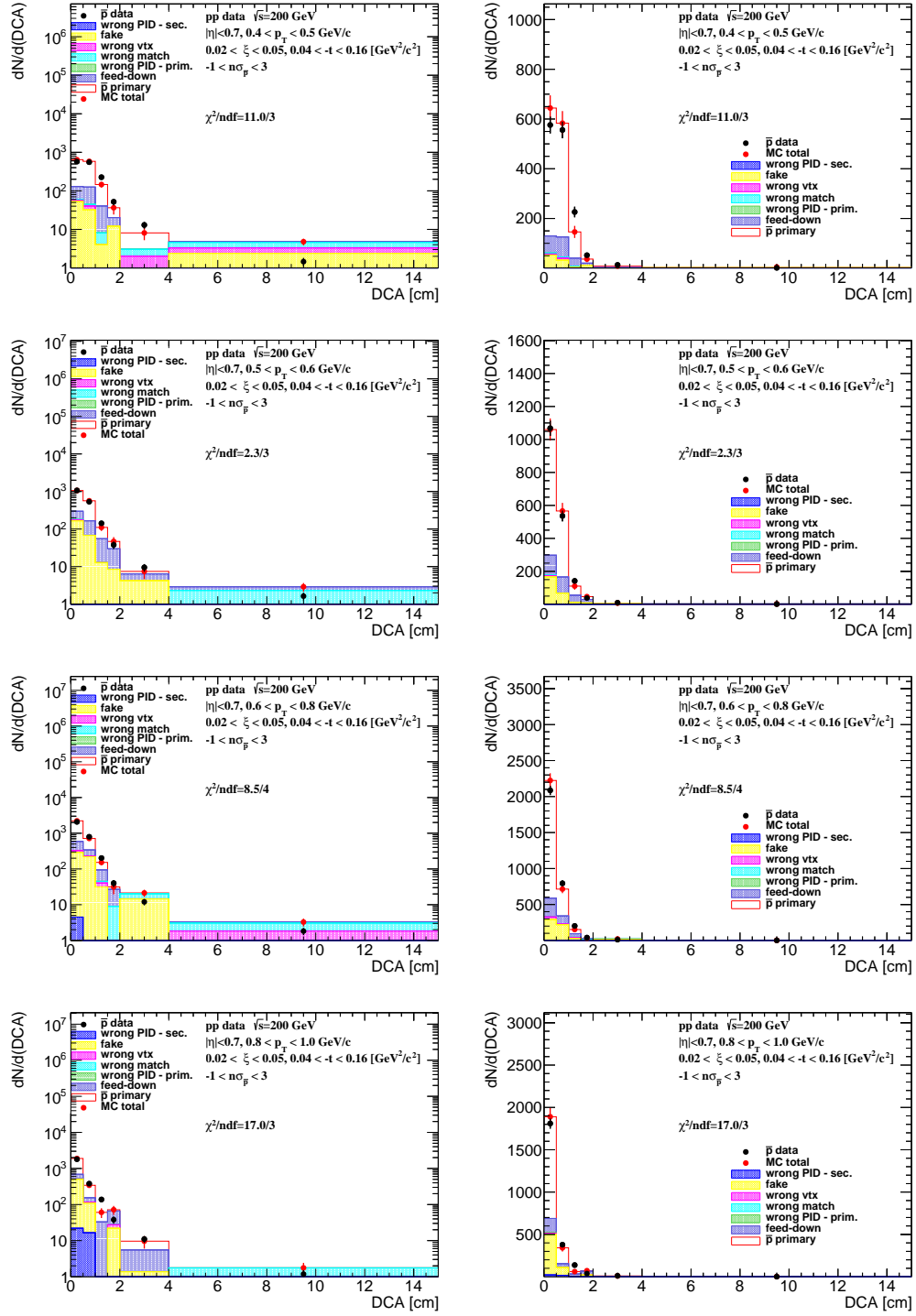


Figure A.7: Distributions of DCA for antiprotons in SD interactions with  $0.02 < \xi < 0.05$  and loose selection.

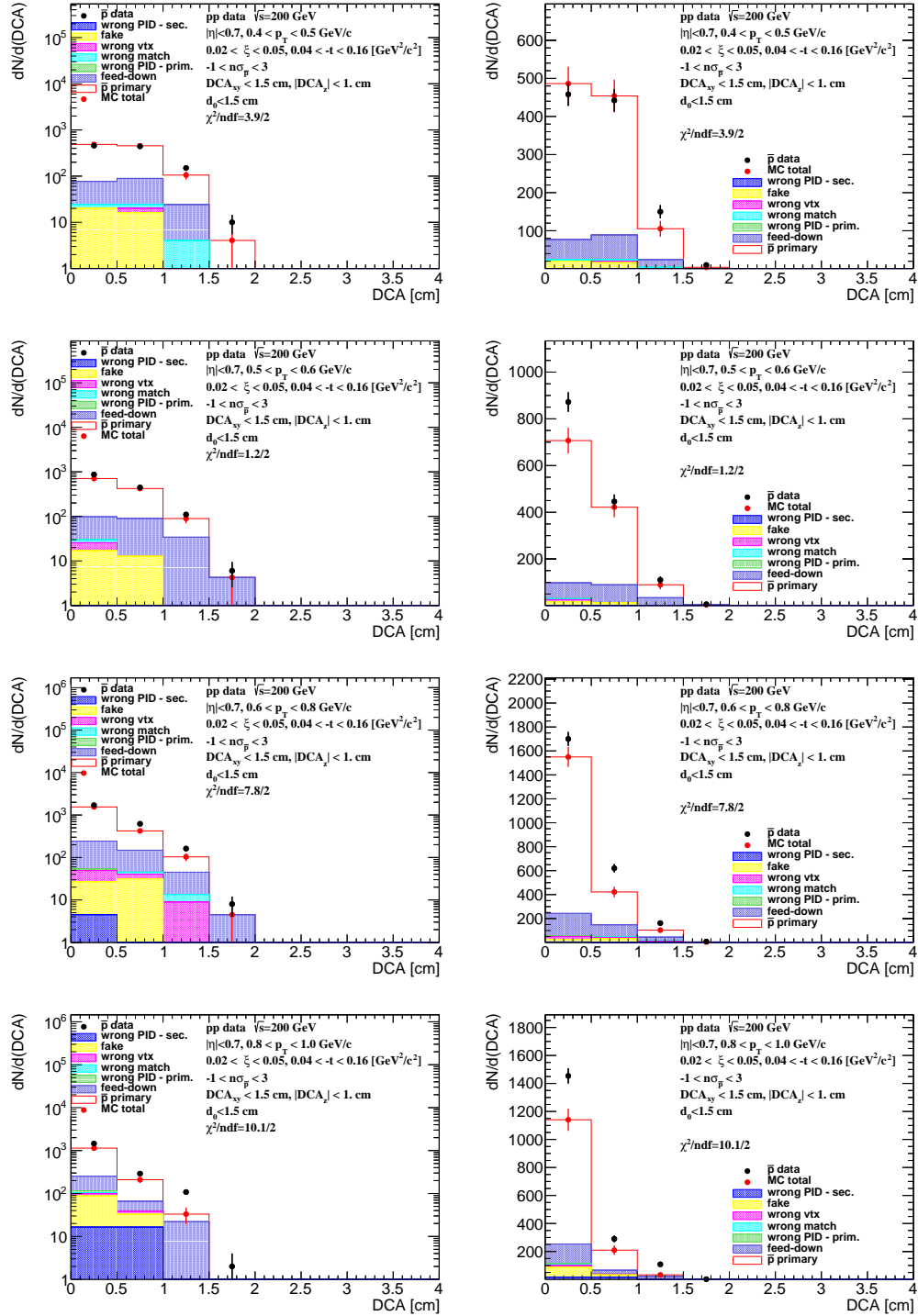


Figure A.8: Distributions of DCA for antiprotons in SD interactions with  $0.02 < \xi < 0.05$  and normal selection.

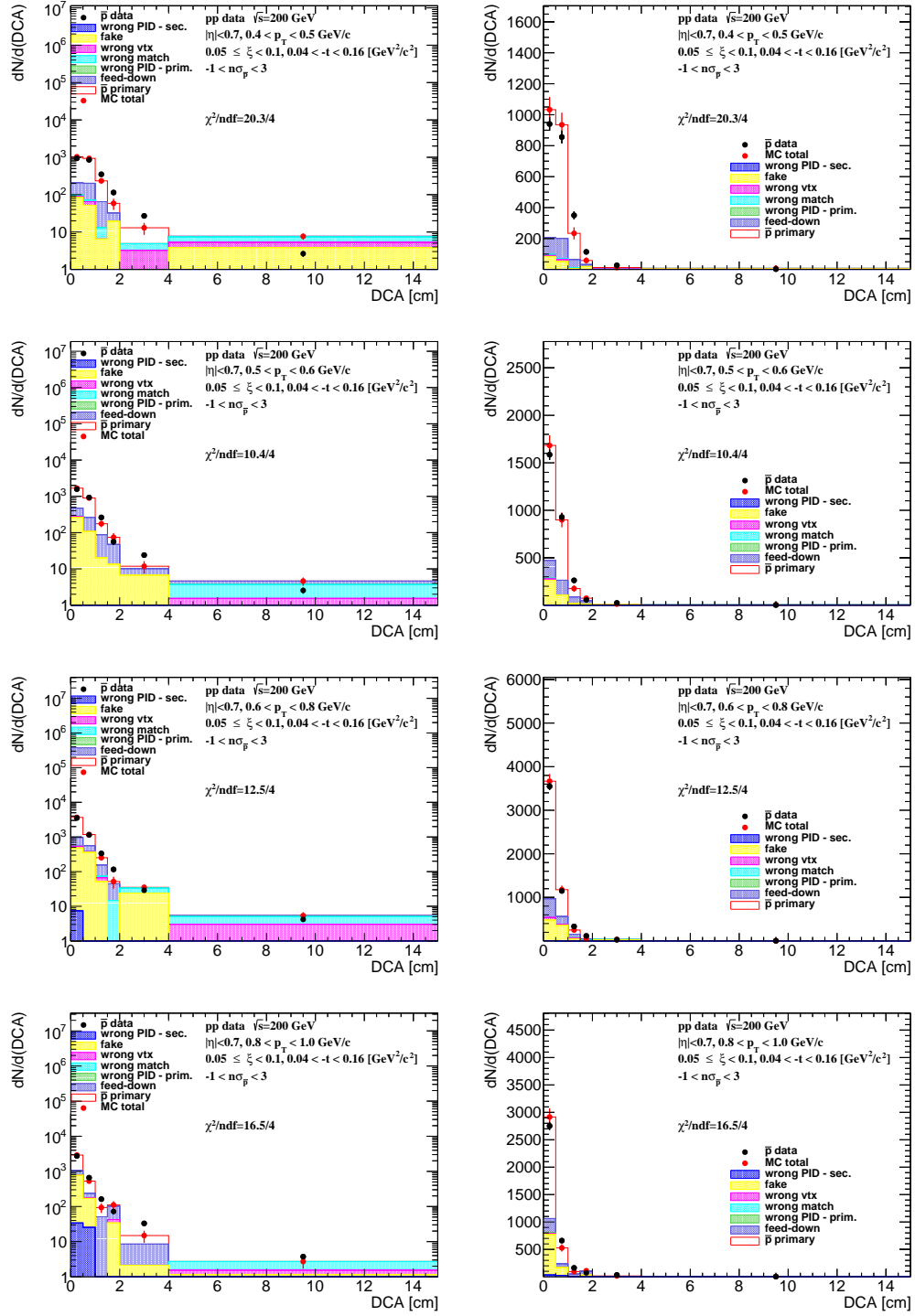


Figure A.9: Distributions of DCA for antiprotons in SD interactions with  $0.05 < \xi < 0.1$  and loose selection.

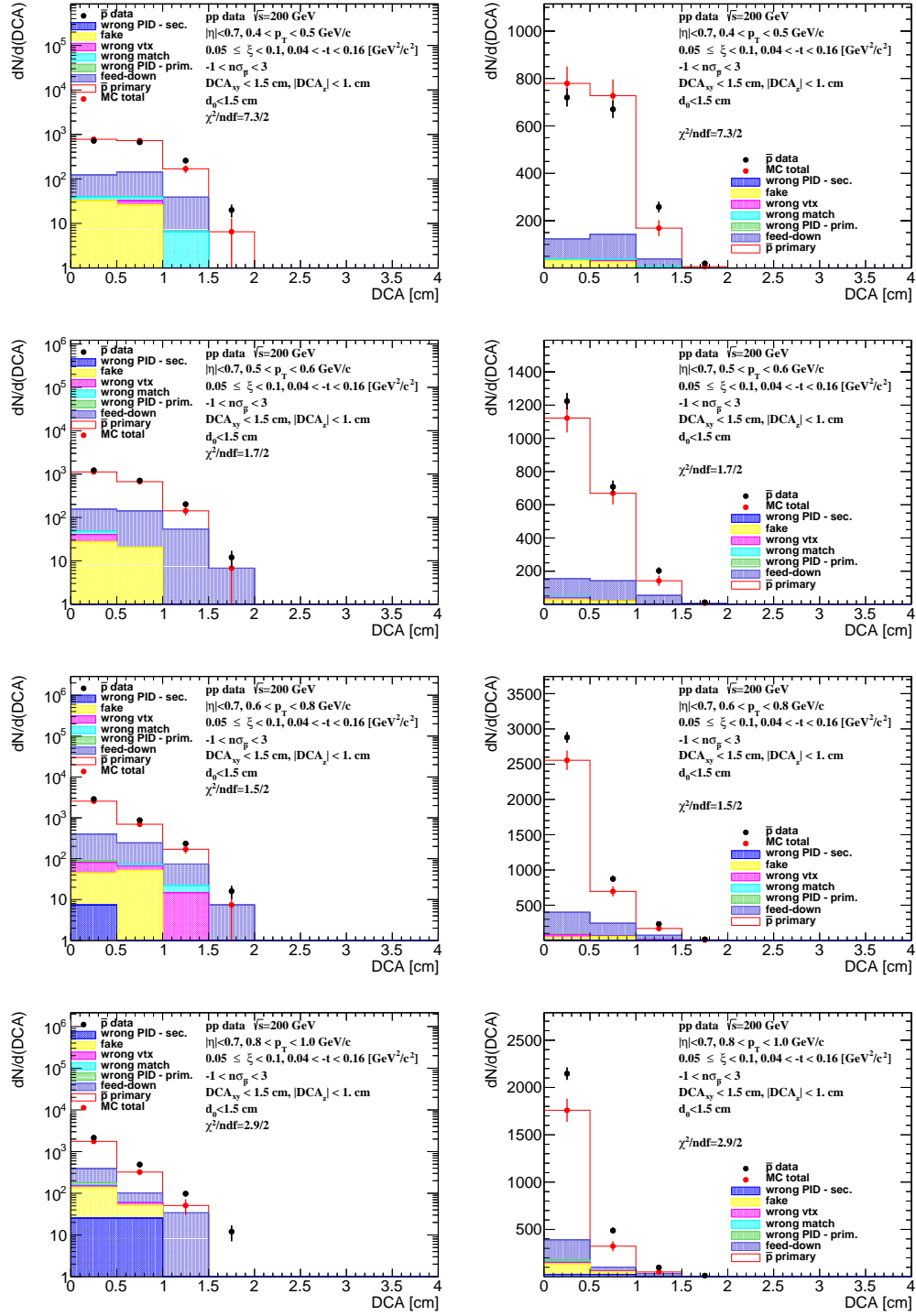


Figure A.10: Distributions of DCA for antiprotons in SD interactions with  $0.05 < \xi < 0.1$  and normal selection.



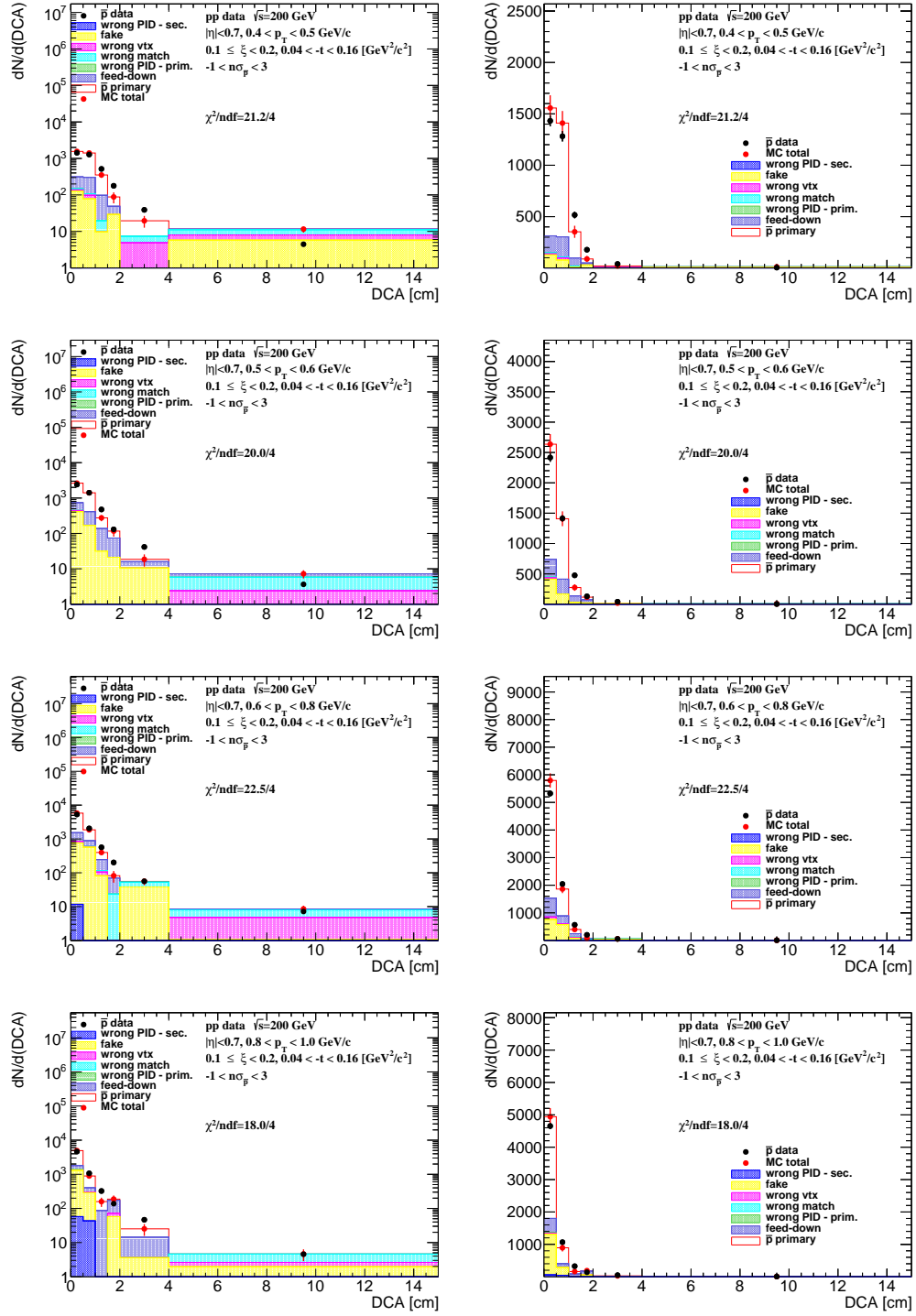


Figure A.11: Distributions of DCA for antiprotons in SD interactions with  $0.1 < \xi < 0.2$  and loose selection.

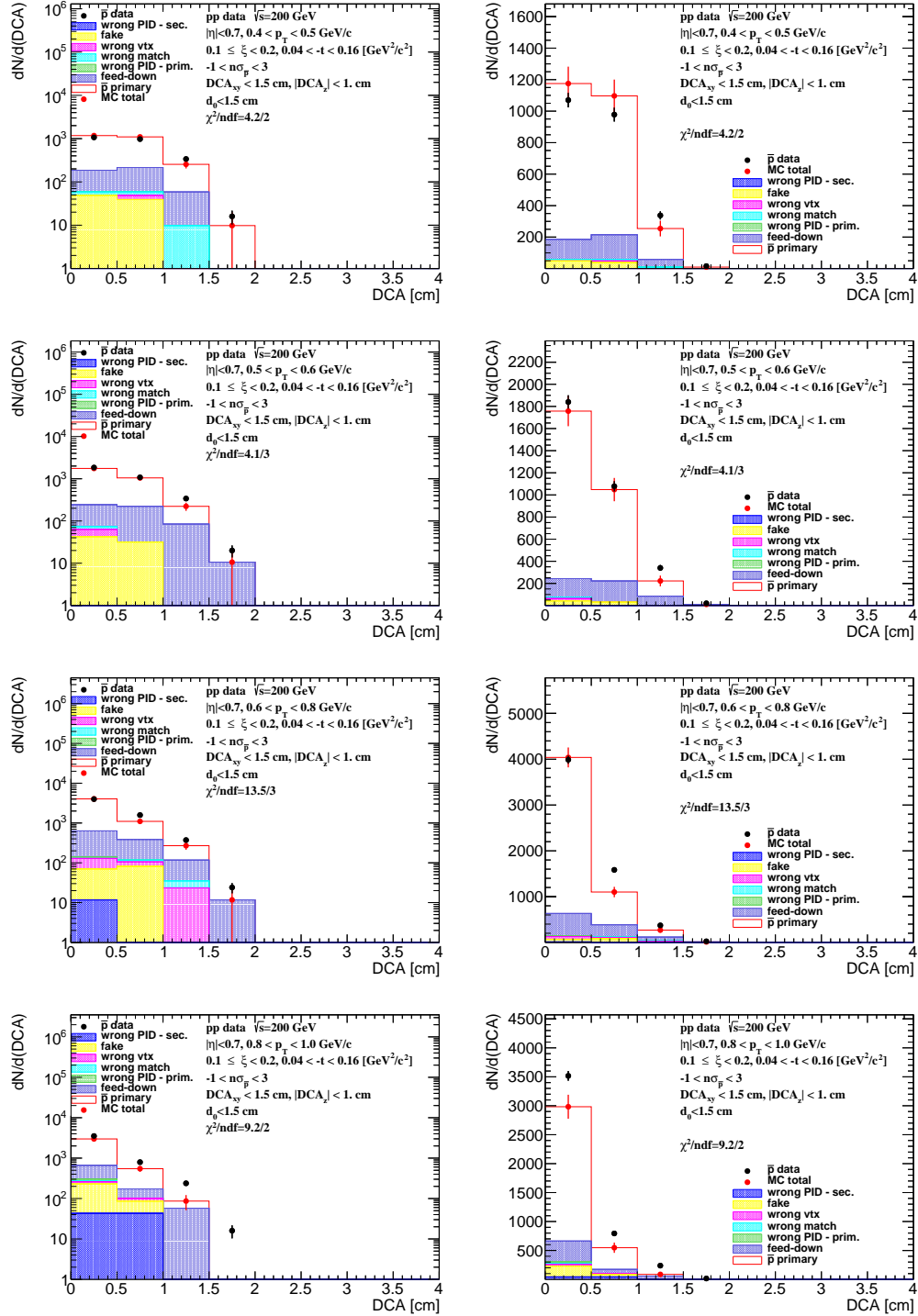


Figure A.12: Distributions of DCA for antiprotons in SD interactions with  $0.1 < \xi < 0.2$  and normal selection.

# B. Distributions of $n\sigma_{dE/dx}^i$ in SD

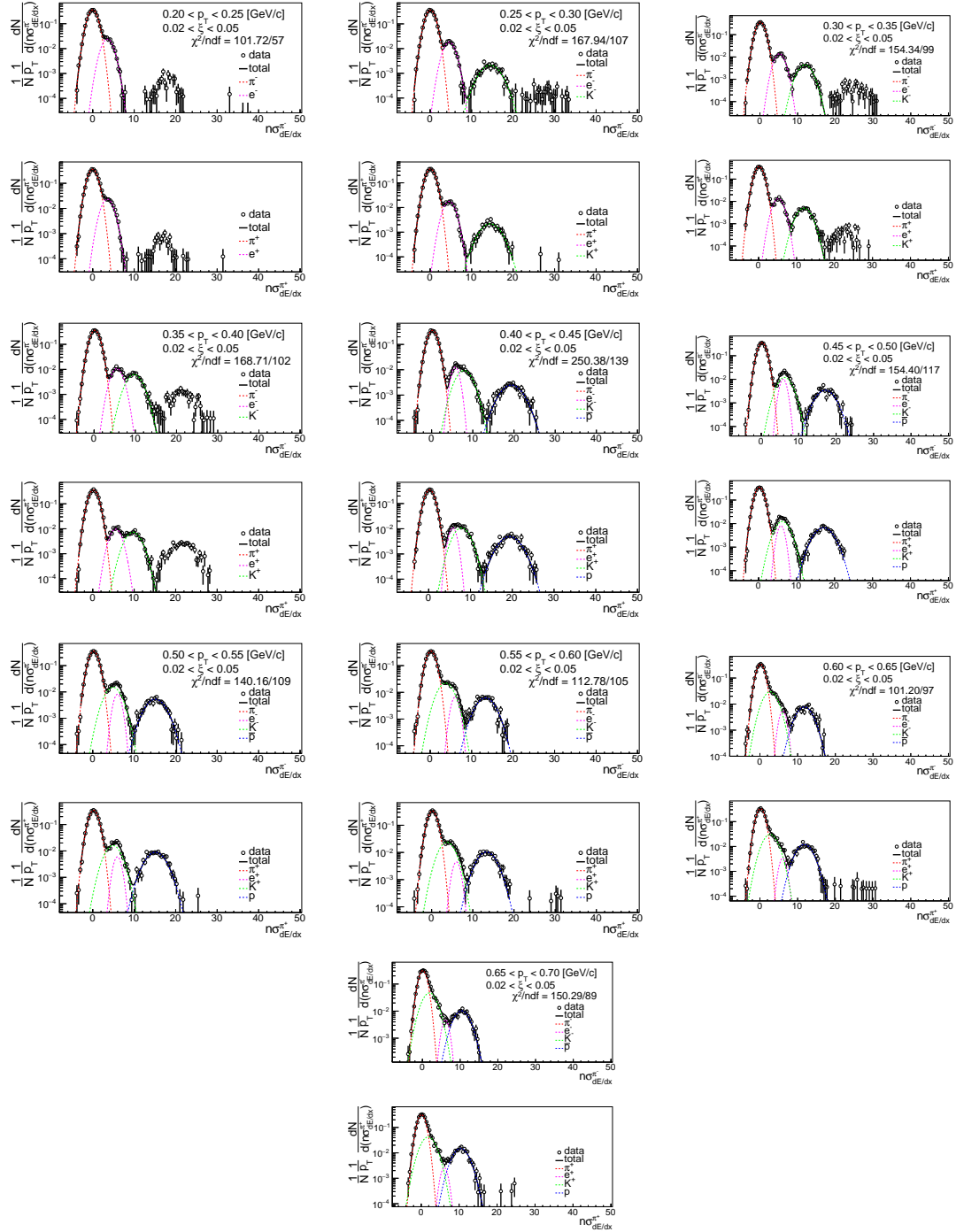


Figure B.1: Distributions of  $n\sigma_{dE/dx}^{\pi^\pm}$  for  $\pi^\pm$  in SD interactions with  $0.02 < \xi < 0.05$ .

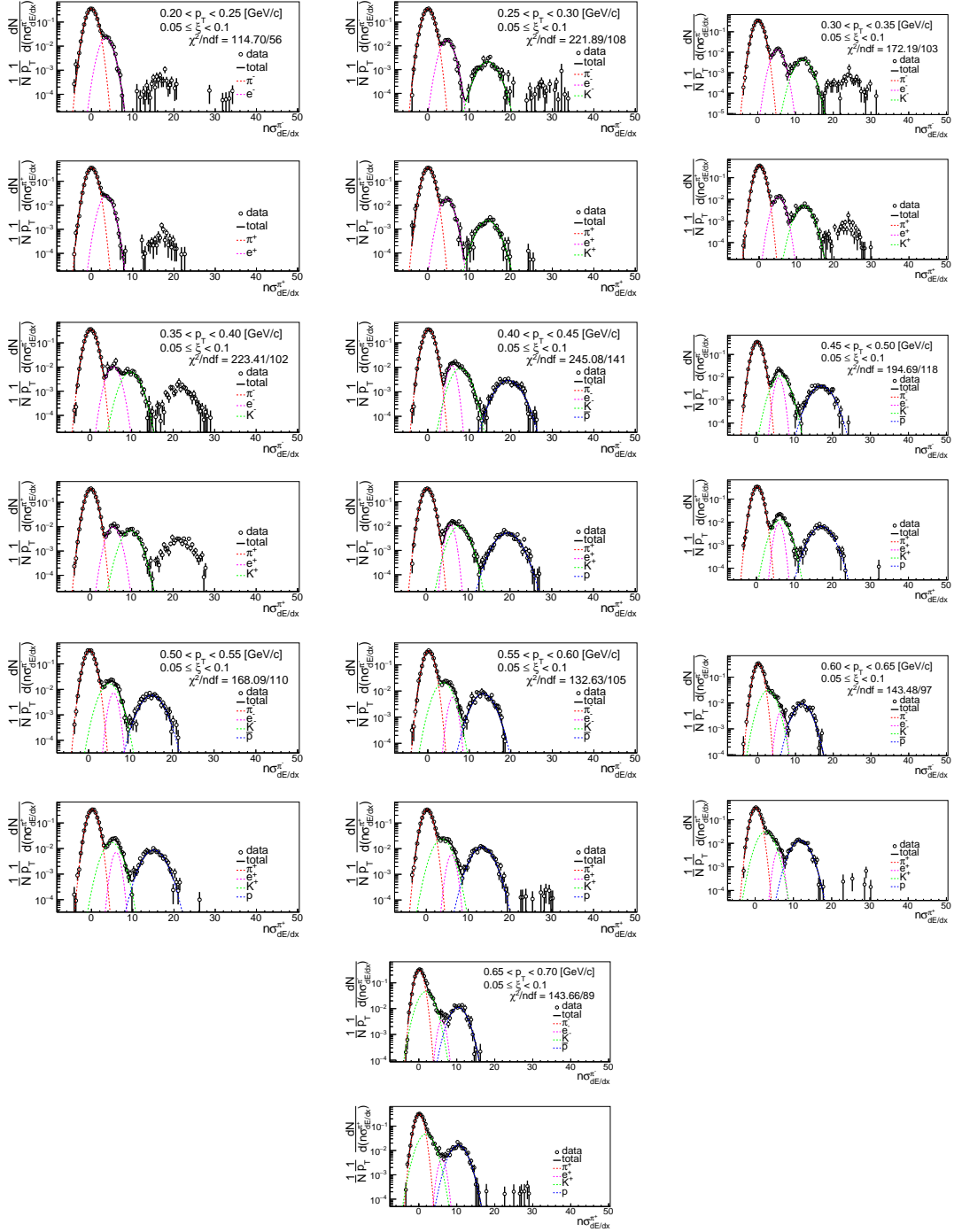


Figure B.2: Distributions of  $n\sigma\pi^\pm/dE/dx$  for  $\pi^\pm$  in SD interactions with  $0.05 < \xi < 0.1$ .

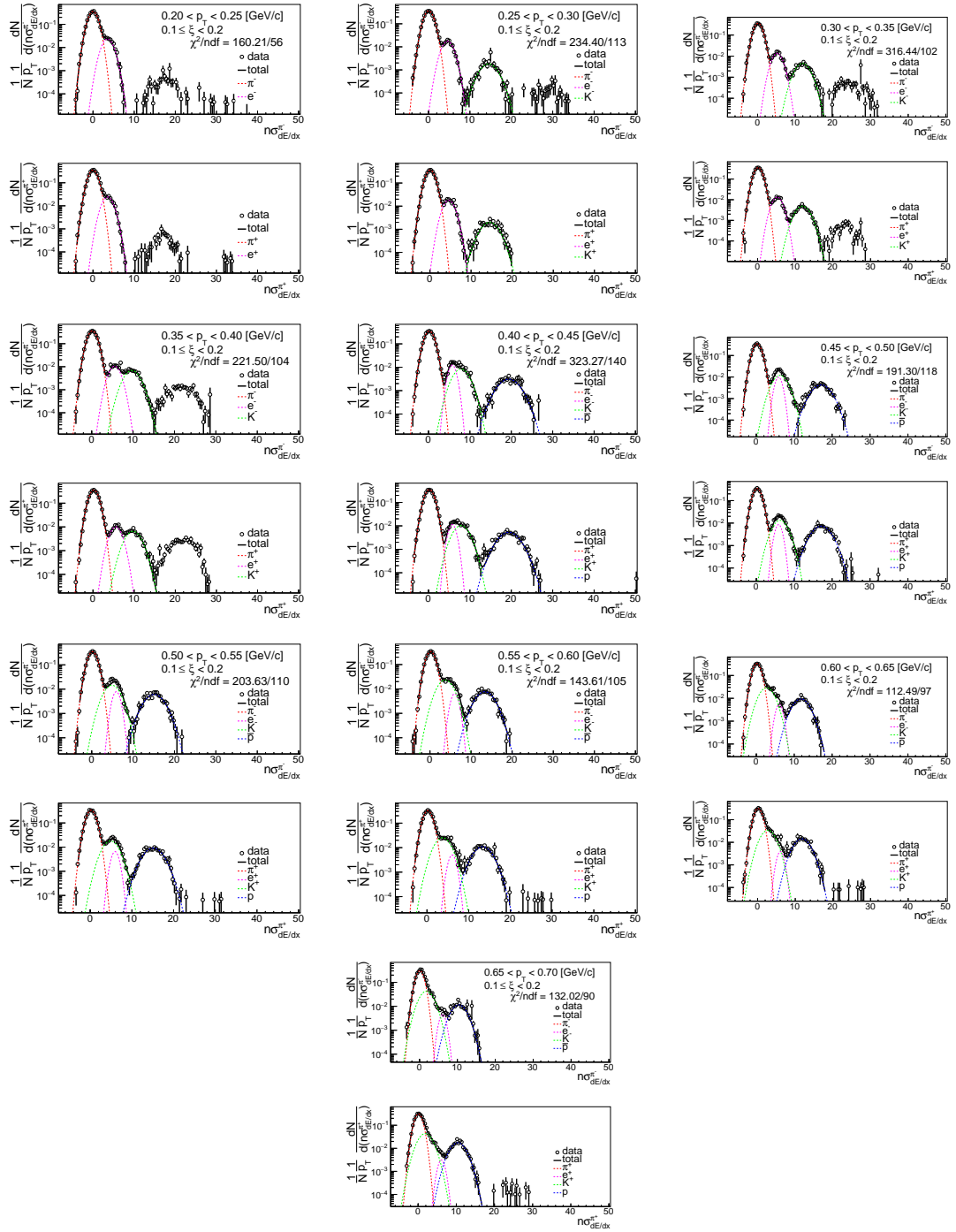


Figure B.3: Distributions of  $n\sigma_{dE/dx}^{\pi^\pm}$  for  $\pi^\pm$  in SD interactions with  $0.1 < \xi < 0.2$ .

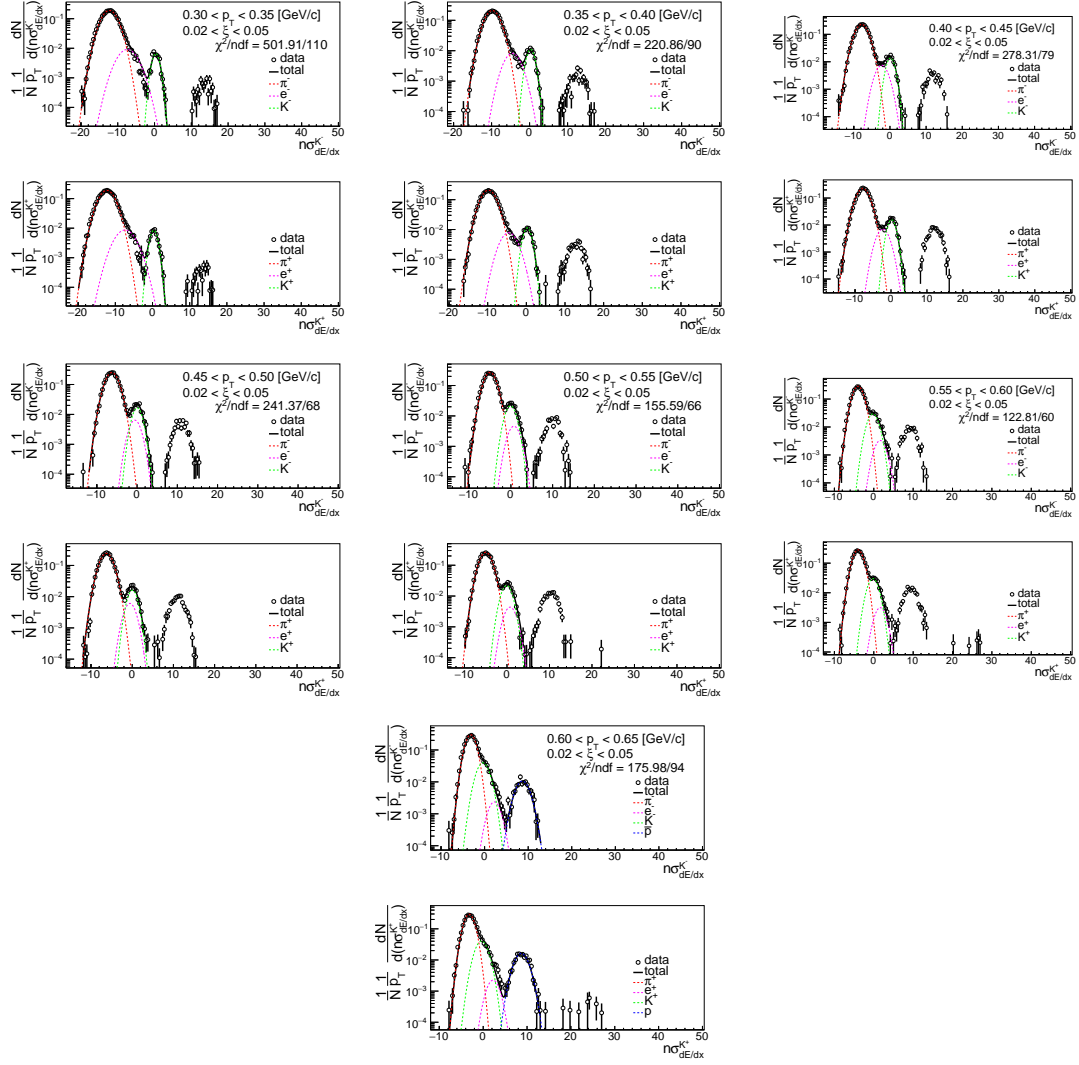


Figure B.4: Distributions of  $n\sigma_{dE/dx}^{K^\pm}$  for  $K^\pm$  in SD interactions with  $0.02 < \xi < 0.05$ .

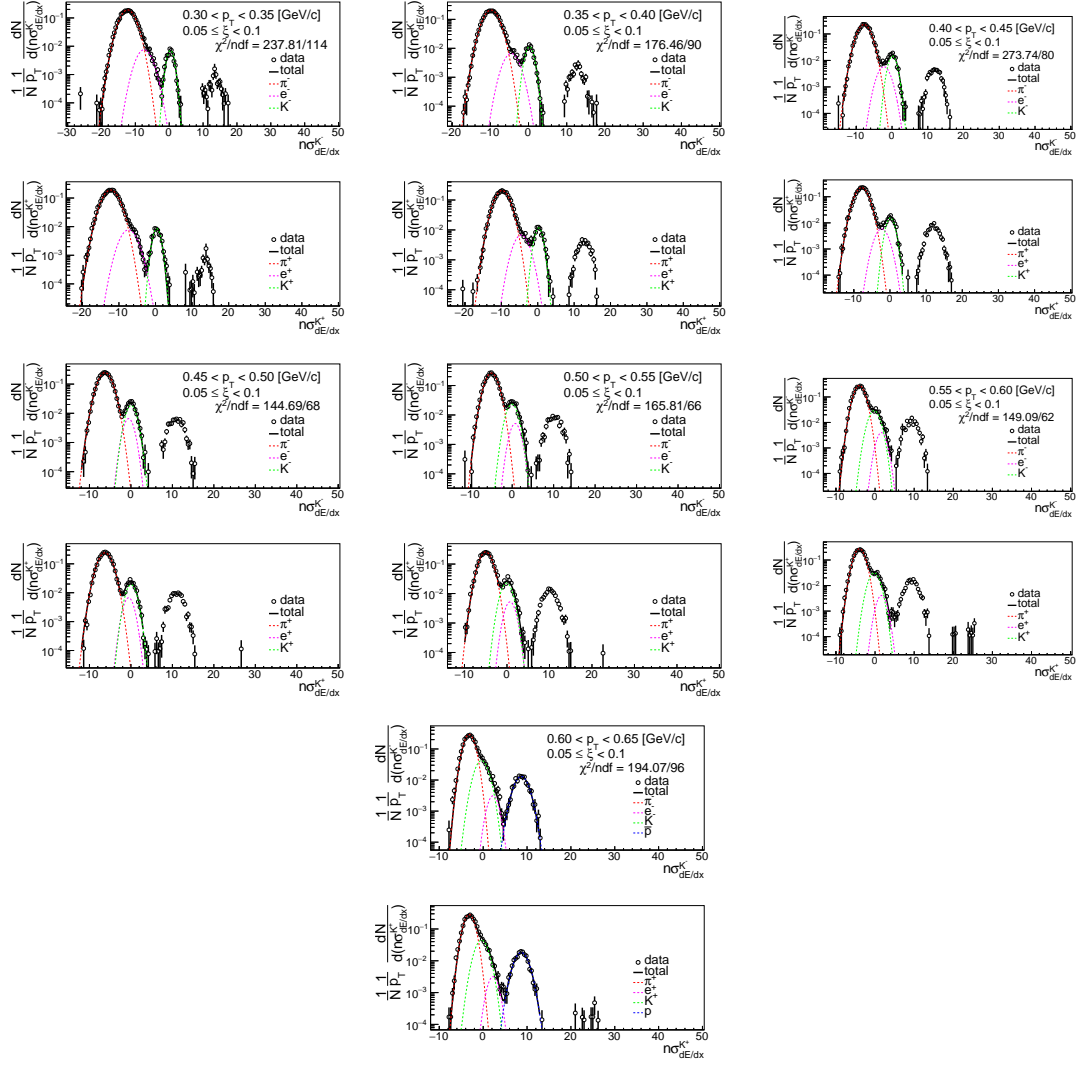


Figure B.5: Distributions of  $n\sigma_{dE/dx}^{K^\pm}$  for  $K^\pm$  in SD interactions with  $0.05 < \xi < 0.1$ .

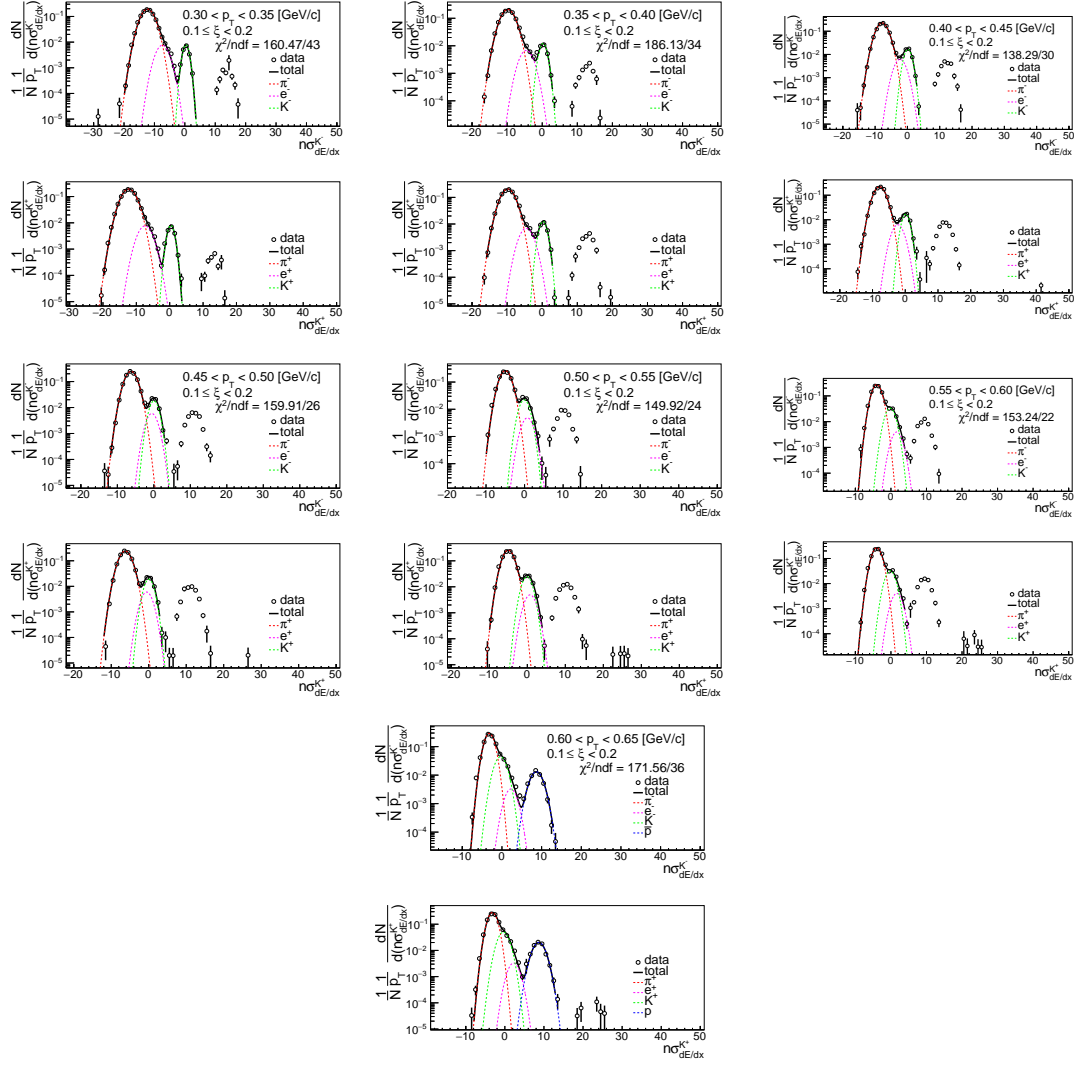


Figure B.6: Distributions of  $n\sigma_{dE/dx}^{K^\pm}$  for  $K^\pm$  in SD interactions with  $0.1 < \xi < 0.2$ .



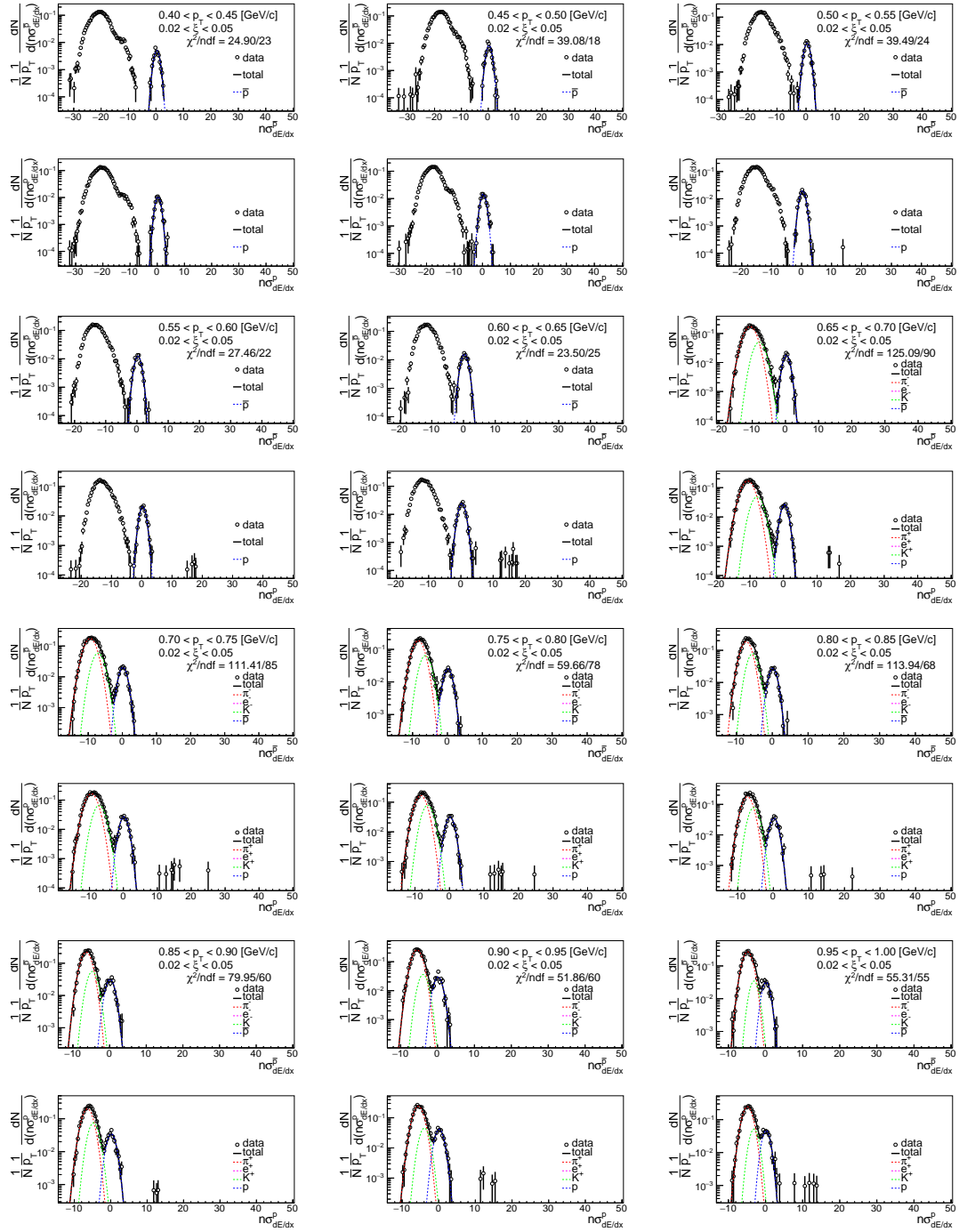


Figure B.7: Distributions of  $n\sigma_{dE/dx}^{\bar{p},p}$  for  $\bar{p}, p$  in SD interactions with  $0.02 < \xi < 0.05$ .

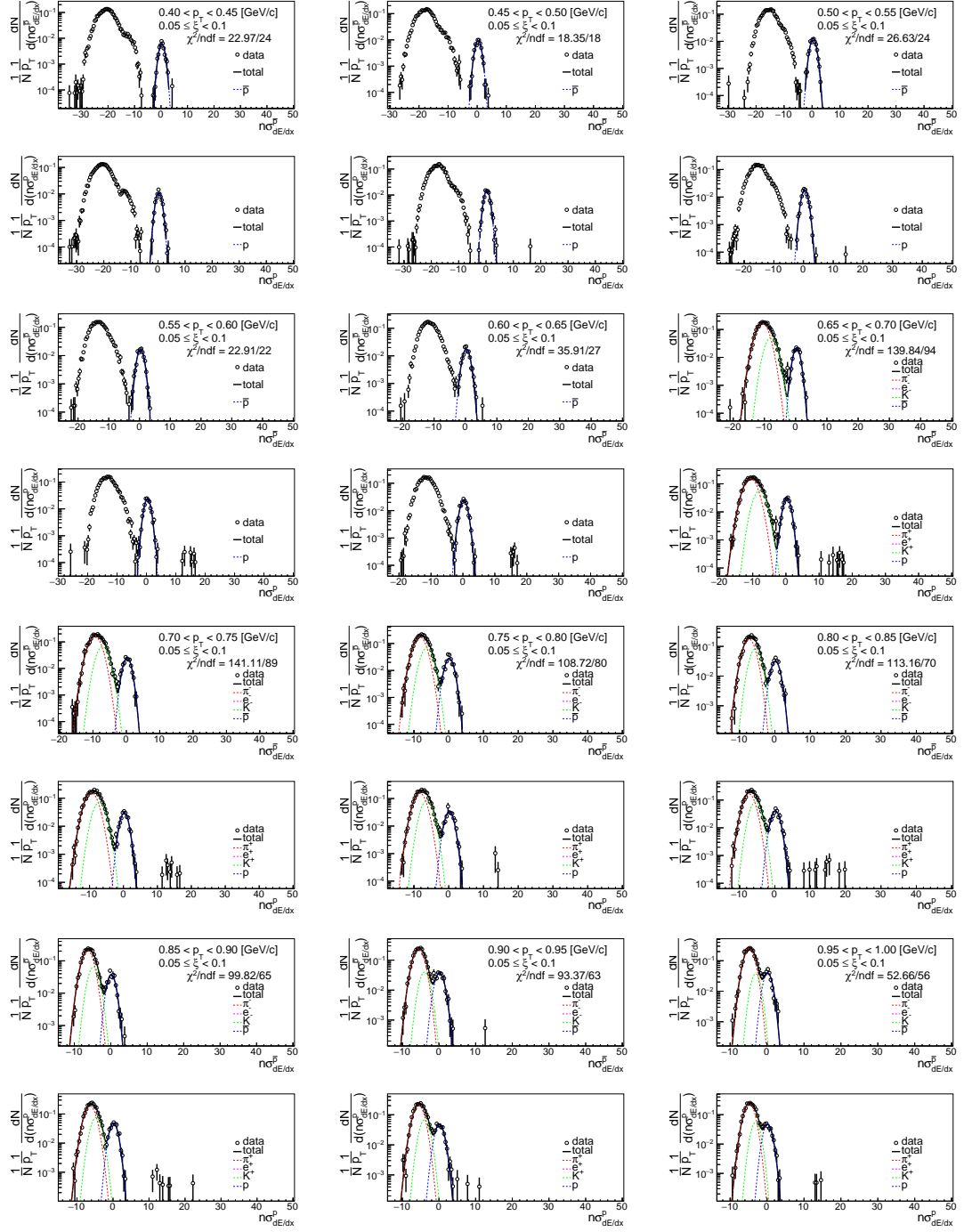


Figure B.8: Distributions of  $n\sigma_{dE/dx}^{\bar{p},p}$  for  $\bar{p}, p$  in SD interactions with  $0.05 < \xi < 0.1$ .

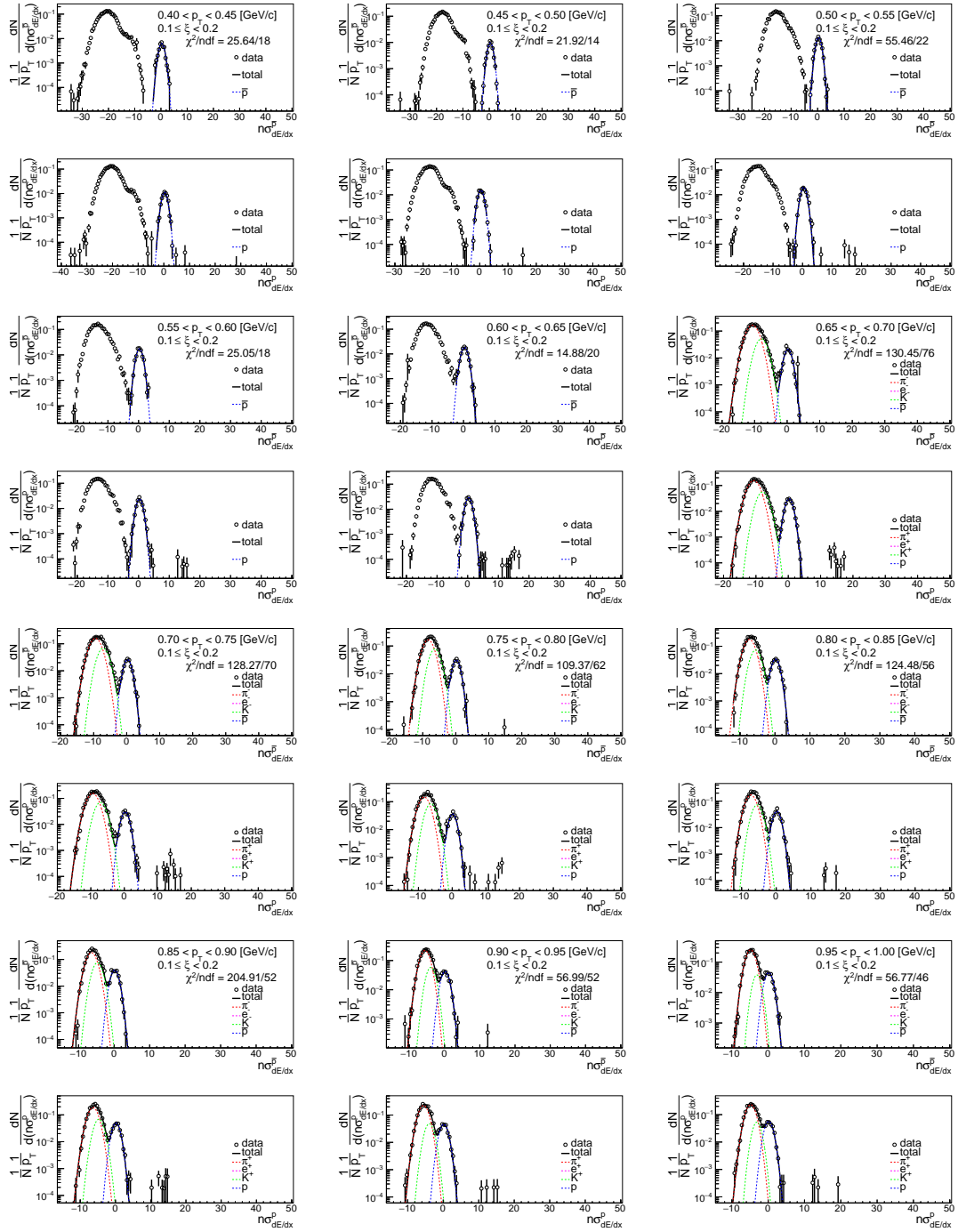


Figure B.9: Distributions of  $n\sigma_{dE/dx}^{\bar{p},p}$  for  $\bar{p}, p$  in SD interactions with  $0.1 < \xi < 0.2$ .